Technische Universität Braunschweig

NFL
am Campus Forschungsflughafen

On the Impact of High-Speed Drops on Dry and Wetted Surfaces

David Burzynski
TU Braunschweig, Institut für Strömungsmechanik

Niedersächsisches Forschungszentrum für Luftfahrt - Forschungsbericht 2021-03

TU Braunschweig – Niedersächsisches Forschungszentrum für Luftfahrt

Berichte aus der Luft- und Raumfahrttechnik

Forschungsbericht 2021-03

On the Impact of High-Speed Drops on Dry and Wetted Surfaces

David Burzynski

TU Braunschweig
Institut für Strömungsmechanik

Diese Arbeit erscheint gleichzeitig als von der Fakultät für Maschinenbau der Technischen Universität Carolo-Wilhelmina zu Braunschweig zur Erlangung des akademischen Grades eines Doktor-Ingenieurs genehmigte Dissertation.

Die Deutsche Bibliothek - Einheitsaufnahme
Die Deutsche Nationalbibliothek verzeichnet diese Publikation in der Deutschen Nationalbibliografie.

David Burzynski
On the Impact of High-Speed Drops on Dry and Wetted Surfaces

Diese Arbeit erscheint gleichzeitig als von der Fakultät für Maschinenbau der Technischen Universität Carolo-Wilhelmina zu Braunschweig zur Erlangung des akademischen Grades eines Doktor-Ingenieurs genehmigte Dissertation.

Herausgeber der NFL Forschungsberichte:
TU Braunschweig – Niedersächsisches Forschungszentrum für Luftfahrt
Hermann-Blenk-Straße 42 • 38108 Braunschweig
Mail: nfl@tu-braunschweig.de
Internet: www.tu-braunschweig.de/nfl

On the Impact of High-Speed Drops on Dry and Wetted Surfaces

Von der Fakultät für Maschinenbau
der Technischen Universität Carolo-Wilhelmina zu
Braunschweig

zur Erlangung der Würde
eines Doktor-Ingenieurs (Dr.-Ing.)
genehmigte Dissertation

von:	**David A. Burzynski, M.Sc.**
aus:	Caracas

eingereicht am:	28.07.2020
mündliche Prüfung am:	26.11.2020
Gutachter:	Prof. Dr.-Ing. Rolf Radespiel Apl. Prof. Dr. Ilia V. Roisman Dr.-Ing. habil. Stephan E. Bansmer

2021

Abstract

This thesis focuses on the high-speed impact of liquid drops on dry smooth surfaces and thin liquid films in the presence of a strong gas flow using experimental and numerical methods. In many applications, the phenomena of high-speed drop impact under these extreme conditions are important, but, at the same time, this common problem is not well understood. A novel and robust experimental set-up was designed to study such challenging conditions in a reliable manner. In this thesis, the high-speed impact of drops was achieved using the newly developed flywheel, three different liquids, and ten surrounding gas mixtures. This allowed to investigate the impact in a wide range of Weber and Reynolds numbers, which varied from 2,000 to 30,000 and from 8,000 to 100,000, respectively. A sophisticated algorithm was also developed for image analysis and to handle a large number of experimental data. Selected experimental cases were complemented with high-resolution numerical simulations performed in OpenFOAM, which provided insights on the flow around and inside the impacting drop.

The outcome of high-speed impact onto a dry wall was studied in detail. The following parameters were measured: the entrapped ring of microbubbles, the ejected secondary droplets size, their velocity, the total ejected volume, the time evolution of the spreading diameter, and the maximal spreading diameter. The results indicate that the possible splashing outcomes of high-speed drops on dry surfaces are corona detachment, corona splash, prompt/jet splash, and prompt splash. It is also demonstrated that the splashing outcome depends mainly on the physical properties of the drop liquid and not on the drop size, velocity, or the surrounding gas. The mechanism of gas entrapment at the early stage of the impact is not responsible for the splashing of drops; however, the physical properties of the surrounding gas influenced the spreading lamella and the ejection of secondary droplets. After analyzing multiple images and the secondary droplets ejected, it can be stated that the Reynolds number of the drop may play a more important role than the Weber number. A theoretical model was developed based on the Rayleigh-Taylor instability of the rapidly advancing liquid lamella and the work of Riboux and Gordillo (2014), which at-

tributes the splashing to the aerodynamic lift force to the spreading lamella. The results demonstrated that the prompt splash is indeed well described by the Rayleigh–Taylor instability and that this instability can be used to determine the boundaries defining the prompt splash; therefore, it can be used to distinguish between the corona and prompt splash regimes. The methods developed in this thesis allow to estimate the entire outcome of splashing, including the size, velocity, and ejected volume, and also predict with high accuracy whether a drop would splash or not.

The outcome of high-speed impact onto a wetted wall was also studied in this thesis. This is a completely different phenomenon from the impact on dry surfaces. In this case, the following parameters were measured: the film thickness, the crown diameter and height, the crown thickness, the ejected secondary droplets size, their corresponding velocity, and the total ejected volume. The results indicate that the high-speed impact of drops on wetted surfaces always generates a chaotic and thin corona, which bends and deforms itself during the entire splashing process. Contrary to the splashing on dry surfaces, the break-up of the corona can be attributed to at least three different instabilities: rim-bending, Rayleigh-Taylor, and Rayleigh-Plateau instabilities. Those instabilities generate a host of small secondary droplets in a wide range of sizes and velocities. It was found that the thin ejected corona leads to hole formation and the eventual detachment from its base at the last stage of impact. This phenomenon was examined in more detail, which allowed to estimate the thickness of the lamella at several impact conditions. The evolution of crown geometry was modelled using the theory of Yarin and Weiss (1995) and the adaptation proposed by Roisman and Tropea (2002). This approach makes a good prediction of the crown dimension for high-speed impacts on thin films.

Kurzfassung

In dieser Studie wurde der Aufprall von Flüssigkeitstropfen bei hohen Geschwindigkeiten auf glatte trockene und benetzte Oberflächen mit experimentellen und numerischen Methoden untersucht. Dafür ist ein neues Schwungrad-Experiment entwickelt worden, mit dem der Tropfenaufprall mit einer großen Anzahl von Aufprallgeschwindigkeiten, verschiedenen Flüssigkeiten und Gasgemischen analysiert werden konnte. Das Schwungrad-Experiment ermöglichte die Untersuchung in einem weiten Bereich von Weber- und Reynoldszahlen, die von 2.000 bis 30.000 bzw. von 8.000 bis 100.000 variierten. Ausgewählte experimentelle Fälle wurden durch hochaufgelöste numerische Simulationen in OpenFOAM ergänzt, welche einen tieferen Einblick in die Strömung um und innerhalb des aufprallenden Tropfens ermöglichten.

Die experimentellen Ergebnisse des Tropfenaufpralls auf trockenen Oberflächen deuten darauf hin, dass lediglich vier Zerspritzen-Szenarien bei hohen Aufprallgeschwindigkeiten möglich sind, nämlich: die Korona-Ablösung, das Korona-Zerspritzen, das Prompt-Strahl-Spritzen und Prompt-Spritzen. Das Zerspritzen-Szenario hängt stark von den physikalischen Eigenschaften der Flüssigkeiten und nicht von dem umgebenden Gas oder den kinematischen Aufprallbedingungen, wie Durchmesser und Geschwindigkeit, ab. Außerdem konnte in dieser Studie nachgewiesen werden, dass der Mechanismus des Gaseinschlusses in der frühen Phase des Aufpralls nicht für das Zerspritzen der Tropfen verantwortlich ist. Jedoch haben die physikalischen Eigenschaften des umgebenden Gases einen Einfluss auf die Entstehung von Sekundärtropfen während der Ausbreitung der Flüssigkeitslamelle. Bei der Entstehung von Sekundärtropfen spielt die Reynoldszahl eine noch wichtigere Rolle als die Weberzahl. Mit Hilfe einer fundierten theoretischen Analyse konnte in dieser Arbeit bewiesen werden, dass das Prompt-Zerspritzen durch die Rayleigh-Taylor-Instabilität der schnell vorrückenden Flüssigkeitslamelle beschrieben wird. Die Rayleigh-Taylor-Instabilität bestimmt die Grenzen, die das Prompt-Spritzen definieren, und damit kann diese Instabilität zur Unterscheidung zwischen dem Korona- und dem Prompt-Spritzen verwendet werden.

Der Tropfenaufprall bei hohen Geschwindigkeiten auf benetzte Oberflächen erzeugt immer eine chaotische und dünne Korona, die sich während des gesamten Spritzenvorgangs verbiegt und verformt. Im Gegensatz zum Spritzen auf trockene Oberflächen kann der Zerfall der Korona auf mindestens drei verschiedene Instabilitäten zurückgeführt werden: Biege-, Rayleigh-Taylor- und Rayleigh-Plateau-Instabilitäten. Diese Instabilitäten erzeugen eine Vielzahl kleiner Sekundärtropfen in einem weiten Bereich von Größen und Geschwindigkeiten. In dieser Studie konnte auch festgestellt werden, dass die dünne sich ausbreitende Korona in der letzten Phase des Aufpralls zur Lochbildung und Ablösung vom Film führt. Anhang zweier theoretischer Methoden konnte die Dicke der Lamelle bei verschiedenen Aufprallbedingungen abgeschätzt werden. Die Ergebnisse deuten darauf hin, dass die Lochbildung immer bei einer konstanten Lamellendicke stattfindet.

Im Rahmen dieser Arbeit wurden die entstehenden Sekundärtropfen beim Tropfenaufprall auf trockene und benetzte Oberflächen mit hochauflösenden Shadowgraphie-Aufnahmen quantifiziert. Die Ergebnisse aus den theoretischen, experimentellen und numerischen Analysen konnten vereint werden, um die Entstehung der kleinen Sekundärtropfen und darüber hinaus den gesamten Spritzenprozess vollständig zu beschreiben. Die vorgestellten Methoden ermöglichen dementsprechend die Vorhersage des Spritzen-Phänomens für einen Tropfen, der mit niedriger oder hoher Geschwindigkeit auf trockene oder benetzte Oberflächen aufprallt. Damit kann mit großer Genauigkeit prognostiziert werden, ob das Spritzen auftritt oder nicht sowie die Größe, Geschwindigkeit und das Gesamtvolumen der kleinen Sekundärtropfen.

Acknowledgments

This thesis is based on a part of my research conducted at the Institute of Fluid Mechanics (ISM) of the TU Braunschweig. First of all, I would like to acknowledge the German Research Foundation (Deutsche Forschungsgemeinschaft, DFG) for financing this research project (No. BA 4953/3) over the last four years.

My heartfelt gratitude goes to my supervisor Prof. Dr.-Ing. Rolf Radespiel for the advice and support during my time at the ISM and the invaluable discussions about this fascinating research project. I thank you for giving me the opportunity to work for multiple scientific and engineering projects. I would also like to thank you for your consistent candor and transparency in all our meetings.

My deep gratitude goes to Prof. Dr. Ilia Roisman for inspiring me to provide a detailed and in-depth explanation of the physical mechanisms of splashing and for guiding me when analyzing the results. Thank you very much for the intense and fruitful collaboration over the years.

My sincere thanks go to Dr.-Ing. habil. Stephan Bansmer for the helpful ideas, suggestions, and constructive criticism in many discussions. I also appretiate the funny moments every Wendsday morning and the support you gave me when conducting my research project in the direction I wanted to.

I would like to extend my gratitude to all the members of the ISM for the interesting discussions and enjoyable moments. I would especially like to thank Inken Knop, Oliver Esselmann, Juan Velandia, Denis Sotomayor, Stephan Sattler, Arne Baumert, Yasir Malik, and Venkateshwar Bora. Many discussions on my research projects also took place during lunch breaks together with Denis and Juan. I thank you deeply for being more than colleagues during my years at the institute.

Special thanks go to Juan Londoño, Jacob Kötter, Daniel ter Haar, Niklas Bildt, Elia Lichtenstein, Patrick Loster, Christian Breitenstein, and Rory Fegan for working with me in developing and running the experiments and numerical simulations. This dissertation would not have been even possible without your brilliant ideas and constant hard work. I'm very happy to have met you all. I would also like to thank Tobias Hurlbeck and his entire workshop team for producing almost

all the parts used my experiments, and to Jennifer Kupke and Ursula Schamp for helping me with the paperwork related to the research projects.

Additionally, I would like to thank Prof. Dr. Rinie Akkermans for the helpful discussions on fluid dynamics and the great time during the APS conference. I also thank Dr. Richard Semaan for supporting and guiding me in the exploration of different machine learning techniques. My gratitude also goes to Maximilian Pierzyna for the very interesting and fruitful collaboration together with Richard. I would also like to thank Dipl.-Ing. Gabriel Rothe for guiding me to develop a more generalistic perspective over the last years.

Finally, I'm deeply grateful to my wife Lena and my son Sebastian for their unconditional love, support, and patience that allow me to invest much of my free time in this project. You have inspired me to give my best day after day, and have given me the strength to stay in focus. I love you!

Declaration of Authorship

I, David Alexander Burzynski, declare that this thesis and the work presented in it is my own unaided work. All direct or indirect sources used are acknowledged as references. The contents of this thesis have already been published as journal or conference articles. These publications are referenced at the beginning of every chapter and unless it is clearly indicated, the published text has been written by myself. The thesis was proofread by Ms. Martina Baltkalne.

Braunschweig, 26.11.2020

Contents

1 Introduction

The impact of liquid drops on dry and wetted solid surfaces are two common phenomena in nature, and the understanding of the physics underlying them is of fundamental importance in a wide variety of technical applications. On a global scale, the drop impact plays an important role in processes occurring in the natural world. For example, extreme rainfalls are expected to increase in the next years as a result of the ongoing climate change (Allen and Ingram, 2002). The impact of fast wind-driven water drops during extreme weather leads to strong erosion and damage of airplanes, buildings, vehicles, structures, etc. (Erkal et al., 2012). The raindrops also interact with plants by absorbing chemical contamination and diseases of the leaves and transporting them to other plants; this drop impact on plants is considered one of the mechanism of the transmission of foliar diseases (Gilet and Bourouiba, 2014). The transmission of diseases results in harvest failure and promotes the use of pesticides, which consequently affects the crops and the entire ecosystem. The outcome produced by the impact of drops also provides useful information in several scientific disciplines. For example, the analysis of blood patterns in forensic science helps criminalists to determine the origin of blood and thus reconstruct crime scenes (Comiskey et al., 2016).

From a more technical point of view, the impact of drops has an enormous significance in the development of additive manufacturing technologies, which is also known as 3D printing. In such manufacture process, molten drops are released from the printer's heads colliding with a dry surface, afterwards the drops solidify generating a very small structure. This process occurs multiple times until the desired shape is obtained (Gibson et al., 2014). In aviation, the impact of supercooled water drops with the airframe leads to in-flight ice accretion, reducing the aerodynamic performance of the aircraft and in extreme cases causing the loss of control (Gent et al., 2000). Understanding how drops interact with fast-moving surfaces is also essential for the design of new technologies based on inkjet printers (Hoath, 2016). With total global revenue of more than $820Bn in 2019, the inkjet printing industry is a clear example of the importance of technologies that utilize the

drop impact phenomena in the world's economy (IBIS-World, 2019). Another example can be found in the automobile industry, where engineers have to predict and avoid the soiling caused by the impact of raindrops on vehicles in order to improve passenger safety and comfort (Hagemeier et al., 2011). These are only few examples that illustrate the importance of studying and understanding the phenomena related to the drop impacts.

Since the drop impact is fundamental for many applications, it have been studied systematically for more than a century. One of the first investigations of this kind was presented by Worthington (1908), who provided detailed images of this complex phenomena by capturing the impact of water drops onto milk pools. Many other theoretical, experimental, and numerical investigations have been carried out since then to understand the underlying physics of this event. In recent years, the research activities have been intensified due to the advances made in camera and computer technology (Scardovelli and Zaleski, 1999, Thoroddsen et al., 2008). These improvements have provided a much deeper understanding of the involved fluid dynamics than in the previous decades together and will continue to do so in the near future (Josserand and Thoroddsen, 2016). From all those years of investigations, it can be stated that the drop impact is an extremely diverse phenomenon, which depends on a large number of parameters associated not only to fluid dynamics but also chemical reactions and thermodynamics (Rein, 1993, Yarin et al., 2017). What makes this phenomenon very interesting to many scientists most likely is the fact that even small changes in the impact conditions can lead to different outcomes; this makes a general description, modelling, and simulations of the impact problem very challenging.

The outcomes observed during the drop impact are manifold; however, the majority of them can be categorized as coalescence, deposition, fingering, jetting, rebound, receding, splashing, and spreading. Comprehensive reviews of these different outcomes and the recent scientific advances associated with them can be found in Breitenbach et al. (2018), Josserand and Thoroddsen (2016), Liang and Mudawar (2017), Marengo et al. (2011), Moreira et al. (2010), Yarin et al. (2017). From the plethora of events related to drop impacts, this thesis concentrates on the physical phenomenon of splashing. This particular outcome is related to the impact at relatively high velocity and can be observed when drops impact on dry and wetted surfaces. Splashing describes a fast event, in which a part of the liquid drop fragments during the impact, ejecting many small secondary droplets. An example of a drop splash-

ing is shown in figure 1.1. Identifying the conditions at which this phenomenon occurs remains crucial to understand, control, and improve many of the technical applications mentioned above (Josserand and Thoroddsen, 2016, Yarin, 2006). The splashing on dry surfaces does not produce the same outcome as splashing on wetted ones, and these two events are determined by different physical phenomena; therefore, they have to be introduced and described separately.

1.1 Splashing on dry surfaces

When a drop splashes on a dry surface, part of its mass spreads over the surface, while the other part atomizes into small drops, as shown in figure 1.1. Stow and Stainer (1977) presented one of the first studies on the drop impact on dry surfaces. The authors postulated in this study that the surface tension, the properties of the impacting surface, and the kinetic energy of the drop before its impact affect the ejected amount and the size of secondary droplets. Two decades later, Mundo et al. (1995) provided detailed measurements of the impact outcome, including the size and velocity of the ejected small droplets. They proposed to use a composited dimensionless parameter to determine the splashing threshold. The composited parameter K depends exclusively on the liquid properties of the drop and can be expressed as $K = OhRe^{5/4}$, where $Re = \rho_l U D/\mu_l$ the Reynolds number based on the liquid properties of the drop and $Oh = \mu_l/\sqrt{\rho_l D\sigma}$ is the Ohnesorge number. As the K parameter also depends on the surface tension, it can be expressed as a function of $\sqrt{We}/Re$, where $We = \rho_l U^2 D/\sigma$ represents the Weber number also based on the liquid properties of the drop. However, more recent studies suggest that the splashing of

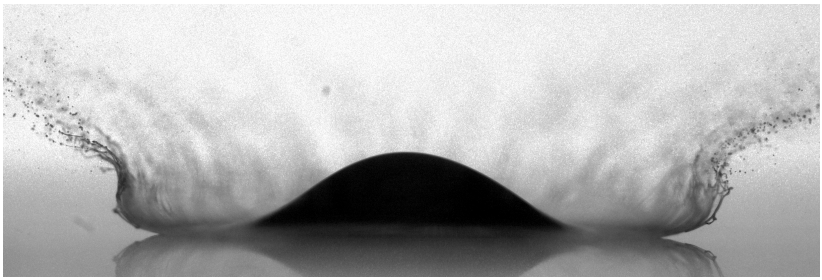

Figure 1.1: Splash of an ethanol drop on a dry surface.

drops is a more complex phenomenon also depending on many surface properties, such as porosity (Sahu et al., 2012), roughness (Roisman et al., 2015), stiffness (Howland et al., 2016), temperature (Liang and Mudawar, 2017), and wettability (Quetzeri-Santiago et al., 2019). The simplicity of the K expression to define the splashing boundary has led to many optimizations of this model over the years (Moreira et al., 2010, Yarin et al., 2017), although a general prediction of splashing on dry surfaces using only the K-Parameter is not accurate (Pierzyna et al., 2021, Roisman et al., 2015).

Xu et al. (2005) demonstrated for the first time that the surrounding gas plays a very important role during the impact of drops on dry smooth surfaces. In the early stages of the impact, the drop deforms just before the contact with the surface and entraps a small amount of gas (Thoroddsen et al., 2003). Afterwards, the drop liquid spreads over the surface, and the gas continues to determine the dynamics of the thin lamella (Stevens, 2014). The experiments of Xu et al. (2005) demonstrated that splashing can even be suppressed by reducing air pressure. They attributed the corona formation during splashing to a weak shock in the surrounding gas that is caused by the fast acceleration of the lamella. Riboux and Gordillo (2014) proposed a more physical alternative by attributing the phenomenon of splashing to an aerodynamic lift force F_L acting on the spreading liquid. The splashing criterion within the theory of Riboux and Gordillo (2014) is defined as $\beta = (F_L/(2\sigma))^{1/2}$. This expression is achieved by balancing the lamella ejection velocity with the retraction velocity caused by capillarity. Several studies have been performed to modify this theory for impacts on heated, moving, inclined, or hydrophobic surfaces (Gordillo and Riboux, 2019, Hao and Green, 2017, Quintero et al., 2019, Staat et al., 2015). These studies have shown an excellent agreement between the RG theory and the experiments.

The outcome of splashing on dry surfaces can be subdivided into three distinct regimes: receding break-up, corona splash, and prompt splash (Rioboo et al., 2001). In the receding break-up regime, the liquid spreading on the surfaces reaches its maximum and then recedes, leaving some drops on the surfaces. This kind of break-up is caused primarily by the wetting properties of the surface (Yarin et al., 2017). The corona splash regime is characterized by the spreading liquid, which separates from the surface during the impact time U/D, generating a free liquid sheet in form of a crown. This liquid sheet is unstable and breaks up into secondary droplets after forming long liquid ligaments. The instability of the rim formed at the edge of the uprising liquid

sheet has been the focus of investigations since the remarkable work of (Taylor, 1959). To clarify the mechanisms leading to the loss of stability of the rim, some studies proposed to use a theoretical approach, including a linear wave analysis of the transverse rim stability (Krechetnikov, 2010, Krechetnikov and Homsy, 2009, Roisman, 2010, Roisman et al., 2006), other authors relies on numerical studies to investigate the instability mechanism of the phenomenon (Agbaglah et al., 2013, Liu and Bothe, 2016). Yarin and Weiss (1995) proposed that the bending disturbances on the rim at later stages of the impact are non-linear, forming several cusps in the azimuthal direction. These cusps are the origin of multiple jets ejected directly from the rim. More recently, Roisman et al. (2007) showed that the diameters of the small ejected droplets correlate with the diameter of the rim; they concluded that the splash in the corona regime is indeed triggered by the instability of the moving rim. Many experiments studying spray impacts demonstrate that the size of the secondary droplets at high Reynolds numbers can be scaled by the thickness of the viscous boundary layer as $DRe^{-1/2}$ (Roisman et al., 2006, Yarin et al., 2017).

The prompt splash regime differs from the corona splash regime since the secondary droplets are ejected directly from small jets located at the surface. These finger-like jets are formed at the early stage of the impact from the azimuthal undulations in the free surface cusp, as shown by Thoroddsen et al. (2012a). It is also demonstrated that such undulations do not vary during the spreading of the liquid, but it is possible that they can merge or split (Thoroddsen and Sakakibara, 1998). Rioboo et al. (2001) attributed the prompt splash to the roughness of the surfaces, indicating the importance of the surface morphology on the impact process. The effect of the surface morphology on splashing was studied by Tsai et al. (2010), who demonstrated that the microscopic pillars on the surface affect the splashing outcome. Latka et al. (2012) studied the drop impact on surfaces with random roughness and concluded that in low viscosity liquids the roughness of the surface causes splashing, while the roughness can suppress the drop splashing in the case of high viscosity liquids. As a consequence, the considerable differences between the corona and the prompt splash have been attributed to the surface roughness (Latka et al., 2012, Xu et al., 2007). Palacios et al. (2013) performed an extensive experimental study, varying the physical properties and kinematic impact conditions of the drops, and found out an empirical boundary that separates both splashing regimes for low impact velocities. Several other analytical, numerical, and experimental studies have been performed to analyse the mecha-

nism leading to the generation of vast amounts of secondary droplets during the impact on dry surfaces (Boelens and de Pablo, 2018, Jian et al., 2018, Mandre and Brenner, 2012, Moore et al., 2018).

1.2 Splashing on wetted surfaces

Splashing on a wetted surface is also a multifaceted phenomenon, where the presence of a liquid layer may increase the level of complexity; thus, the outcome is different from what is observed in impacts on dry surfaces (Rein, 1993). This can be clearly observed by comparing the images of figures 1.1 and 1.2. Kittel et al. (2018) demonstrated that when a drop impacts on a liquid layer, the typical outcomes can be deposition, corona splash, corona formation without the generation of secondary droplets, corona splash after detachment from the surface, and central jet break-up after the formation and collapse of a crater into the liquid layer. In general, splashing on a surface wetted with another liquid also leads to the formation of a large free liquid sheet similar to the one observed when a drop impacts a dry smooth surface. However, the splashing on a wetted surface results from the interaction between the liquid of the spreading drop and the liquid film, and not by an aerodynamic lift force acting on the free lamella (Guo et al., 2016).

The use of different liquids for the drop and film leads to different outcomes in the corona splash regime, as demonstrated by Thoroddsen et al. (2006). The existence of a large surface tension gradient gives rise to the Marangoni effect, thinning the lamella locally and producing several holes. This hole formation promotes the lamella break-up, which in turn produces a large number of secondary droplets. But even when the drop and film liquid are the same, the generation of secondary droplets is a complex process that depends on many other effects. (Cossali et al., 1997) demonstrated that the outcome of splashing can be greatly influenced by the thickness of the film, also when the drop and film are of the same fluid. The time evolution of splashing can be divided into four different phases almost regardless of the film thickness: 1) the crown formation with the eventual ejection of small droplets, 2) the rim instability and finger-like jet formation, 3) the break-up of jets into secondary droplets, and 4) the period of crown detachment or collapse. Detailed experiments at the early stage of impact demonstrated that an axisymmetric ejecta sheet develops before the crown can be formed (Thoroddsen, 2002). A von Kármán-like vortex between the drop and liquid layer interface has been identified as the mechanism

Figure 1.2: Splash of a water drop on a thin film.

responsible for the break-up of this thin ejecta sheet (Castrejón-Pita et al., 2012, Thoraval et al., 2012).

As the spreading lamella during the splashing of liquids of the same fluid on wetted surfaces is not greatly affected by the aerodynamic lift force, the splashing can be roughly predicted using the dimensionless K-parameter $K(We, Re)$. By incorporating the film thickness and velocity in this parameter, the boundary between the deposition and splashing seems to provide good agreement with the experiments (Gao and Li, 2015). Further variants of the K-parameter have been proposed depending on the conditions of the impact, as reviewed in Moreira et al. (2010). A more physical explanation of splashing has been given by Yarin and Weiss (1995), who have attributed the splashing on liquids to the propagation of a kinematic discontinuity in a liquid film. This discontinuity leads to the ejection of an uprising and expanding rim-bound corona, which is also called a crown. The instabilities of this rim lead to the generation of cusps with finger-like ligaments, which then rupture into secondary droplets (Roisman, 2010, Roisman et al., 2006).

Different instability mechanism has been proposed to describe the emergence of the ligaments, and, up to date, there is no consensus on the underlying mechanism of splashing (Yarin et al., 2017). The periodic disturbances in the crown are usually attributed to the Rayleigh-Plateau instability, Rayleigh-Taylor instability, bending instability, or to a combination of the longitudinal and azimuthal instabilities (Ag-

baglah and Deegan, 2014, Krechetnikov, 2010, Roisman, 2010, Villermaux, 2007, Yarin, 2006). More recently, Li et al. (2018) demonstrated that azimuthal instabilities are formed in the free surface cusp between the droplet and liquid at the early stages of impact. One of the conclusions made by the authors is that these unsteady azimuthal perturbations can be promoted by Rayleigh-Taylor instability. Thus, the final word on the dominant mechanism of splashing has not been said yet.

Characterization of secondary droplets from sheet fragmentation after the drop impact on dry or wetted surfaces has been investigated in a wide range of experiments, as reviewed in Villermaux (2007) and Liang and Mudawar (2017). Many studies have been performed in order to quantify the position, diameter, and velocity of the ejected secondary droplets (Villermaux, 2020). However, such characterization can be very challenging due to the small size of the secondary droplets, which can be of the order of a few micrometers and therefore are rarely detected by standard measurement equipment (Yarin and Weiss, 1995). In the case of drop impact on dry surfaces, several interesting approaches have been developed to overcome these difficulties. For example, Xu et al. (2007) measured large secondary droplets ($d > 100$ μm) by surrounding the impacting drop with a paper sheet and analyzing the footprint of the droplets. The experiments conducted by Thoroddsen et al. (2012a) using a high-speed camera have shown that the ejected droplet size is in a range from $d \sim 5$ to ~ 60 μm for impacts on dry smooth surfaces. As these droplets can be smaller than the spatial resolution of the cameras used in typical experimental set-ups, it is probable that many authors may have erroneously claimed deposition instead of the prompt splash. Using shadowgraph techniques, Faßmann et al. (2013) measured droplets with a diameter of around 30 μm for the corona splash, indicating that very small droplets can be expected also in this splashing regime.

In the case of a drop impact on wetted surfaces, Yarin and Weiss (1995) have produced an extensive analysis of the secondary droplets ejected from a train of drops by providing the size and velocities of the smallest droplets. They demonstrated that the size of the droplets covers a wide range of values. Samenfink et al. (1999) conducted a large number of experiments of the drop impact on shear driving films and analyzed the secondary droplets using a Phase-Doppler-Anemometer. They observed considerable differences from the experimental results of Mundo et al. (1995), indicating that the physics of splashing on wetted surfaces may be different from the physics observed during impacts on dry surfaces. In a more recent study, Okawa et al. (2006)

demonstrated that the number of droplets ejected increases with the K parameter with a slight dependency on the film thickness. The authors provided an empirical correlation between the K parameter and the ejected secondary droplet mass. In agreement with Okawa et al. (2006), Faßmann (2015) reported that the ejected volume is weakly dependent on the film thickness but strongly dependent on the impact velocity. Recently, Li et al. (2019) also highlighted that the size and velocity distributions are less affected by the film thickness.

Numerical and experimental studies have shown an increase in the lamella thickness over time; at the beginning of splashing, it seems to be much smaller than the thickness of the crown formed later. However, a detailed quantification of the secondary droplets provided by Zhang et al. (2012a) demonstrated that the size of the secondary droplets generated at the beginning and at the later stages is not necessarily different from each other. The authors also concluded that no correlation exists between the droplet origin and their sizes. Wang and Chen (2000) observed another break-up process, which occurs when droplets impact very thin films. In such a scenario, the crown can separate from the base leading to the generation of many secondary droplets. In accordance with this conclusion, Roisman et al. (2006) performed a linear stability analysis and showed that the main source of secondary droplets is indeed the crown break-up. It is tentative to make connections from the observations based on spray impact studies to the single drop impact studies. However, both phenomena cannot be compared since during the spray impact a diverse number of drops of different sizes impact on a fluctuating film (Breitenbach et al., 2018, Moreira et al., 2010, Roisman et al., 2006). Hence, the outcome from a single drop impact compared to the spray outcome is completely different.

Another break-up mechanism observed during splashing is the hole formation around the crown when the lamella becomes thin(Marston et al., 2016). This kind of rupture can be directly associated to the rupture of thin free sheets, even when the liquid sheet during the drop impact is moving and expanding. Thoroddsen et al. (2006) reported the hole formation and its subsequent break-up, when concentration gradients are present on the liquid drop. This break-up phenomenon is attributed to the Marangoni effect. The rupture of pure thin free sheets after puncturing (without concentration gradients) has been investigated by many authors, and the governing dynamics of this process are well understood(Culick, 1960, Taylor, 1959). This phenomenon has also been observed during the aerodynamic breakup of drops, as demonstrated in Opfer et al. (2014). However, the hole formation and

break-up of an emerging crown during the splashing on wetted surfaces has not been reported when the physical properties of the drop and film are the same. Finally, the strong differences observed between the different splashing regimes suggest that the governing physics are completely different in each case and cannot be unified into one general theory.

1.3 Motivation

This study was motivated by a large number of problems associated with high-speed drop impacts in technical applications. In the energy industry, for example, water is injected into stationary gas turbine to cool it down, reduce the NO_x emissions, and increase the performance of the turbine (Walsh and Fletcher, 2004). The water drops injected in the turbine first impact on the compressor blades. In such an area, the air pressure and temperature are high, and the drops splash, generating multiple secondary drops that are then transported to the combustion chamber. Predicting the conditions inside this chamber, including the water splashed and the mass of water stuck on the blade, is important for the engineers to optimize the performance of the turbine (Günther et al., 2017).

The soiling of ground vehicles during wet road conditions is another example where water drops can impact a very high velocity and drastically affect the safety of the passengers (Gaylard et al., 2017, Hagemeier et al., 2011). Driving through the rain leads to the accumulation of water on the glasses, disturbing the visibility of the driver. In modern vehicles, a large number of sensors and cameras are used by driver assistant systems, and their functionality has to be guaranteed in rain conditions (Schilling et al., 2020). In such cases, the impact velocities ($U > 30$ m/s) are high and drop diameters ($D \sim 3$ mm) large, resulting in very large Weber and Reynolds numbers. The model of high-speed drops impacting on dry and wetted surfaces, including the splash limit, and the characterization of the secondary droplets is for the prediction of vehicle soiling the weakest point up to date due to the lack of fundamental and experimental studies (Tropea et al., 2019). This is not only true for vehicle soiling problems but for all applications where the drops impact at high Weber and Reynolds numbers.

Another specific problem that motivated this study is the in-flight aircraft icing; this phenomenon has been investigated at the TU Braunschweig for the last decade using an icing wind tunnel (Bansmer et al.,

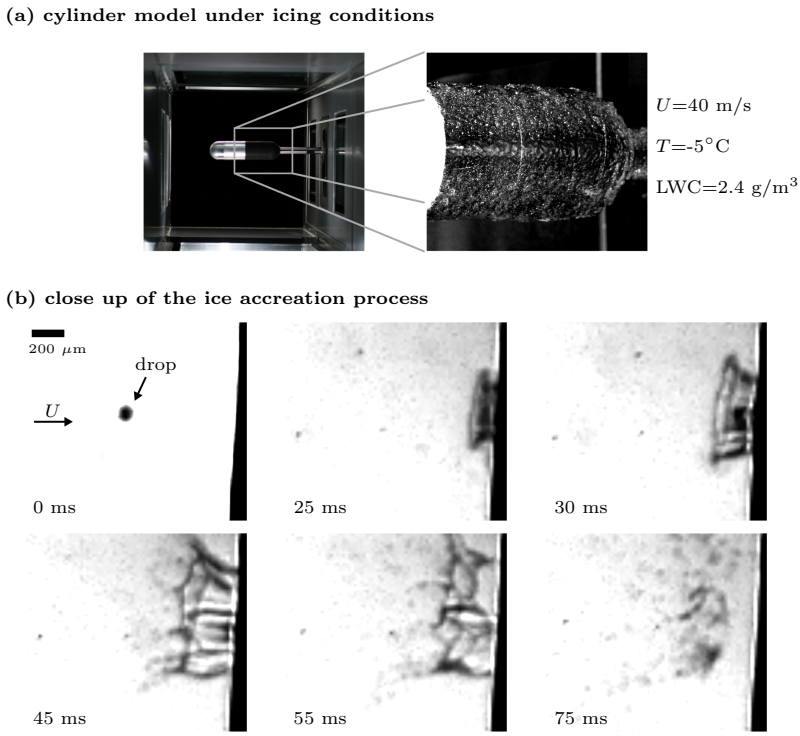

Figure 1.3: Ice accretion caused by the impact of super-cooled drops in the Braunschweig Icing Wind Tunnel. (a) shows the model before and after 1 min of testing. (b) shows the splashing of super-cooled drops during the test. Images courtesy of Arne Baumert, TU Braunschweig.

2018, Baumert et al., 2018). In general, when an aircraft flies through a cloud of super-cooled droplets, drops impact first on a dry surface at high velocity. A part of the drop mass remains on the surface, forming a very thin liquid film, while the other part atomizes into small secondary droplets. After a thin film is formed over the surface, the subsequent drops coming from the cloud impact on it; as a result, the splashing on a dry surface is no longer relevant at this stage. Subsequently, the residual liquid on the surface starts to move due to the strong shear stress caused by the moving airflow (Seiler et al., 2019). Therefore, a correct description of the splashing dynamics on dry surfaces and moving films are essential to understand the ice accretion on

aircrafts (Baumert et al., 2018, Beaugendre et al., 2003, Caminade and Frazza, 2019, Politovich, 1989, Trontin and Villedieu, 2017). Wright and Potapczuk (2004) demonstrated that from all the different phenomena present during the ice accretion, splashing is the most important one. The authors concluded that numerical simulation of the ice accretion process without considering the amount of mass ejected during the splashing leads to a wrong estimation of the ice growth rate. It is important to mention that even when the solidification of supercooled drops plays an important role during the ice accretion process (Schremb et al., 2018), the time scales of splashing $\sim \mu$s are much smaller than those of the solidification $\sim$ s. The existing experimental data suggest that the splashing and solidification can be treated separately (Li, 2013). This hypothesis has been confirmed by multiple experiments conducted by Arne Baumert in the Braunschweig Icing Wind Tunnel (Bansmer et al., 2018). For those experiments, he used a cylinder model and recorded the ice accretion caused by the impact of super-cooled droplets using an ultra-high-speed camera (Baumert, 2019). The results demonstrated that the splashing observed under icing conditions is almost independent of the ambient and surface temperature (see figure 1.3).

Although the high-speed drop impact is important for many applications, only a few fundamental investigations have been published so far, and not all of them have analysed the complex phenomena of splashing. Some examples can be found in Aboud and Kietzig (2015), Mehdizadeh et al. (2004), Visser et al. (2012) and Cimpeanu and Papageorgiou (2018). The major reason for the small number of studies is the high cost and challenging nature of the experimental and numerical methods needed for such investigations. For example, the break-up process can be simulated accurately using only direct numerical simulations; this is necessary because a large number of scales have to be solved. High-resolution and high-speed cameras are mandatory to visualize the ejected small secondary droplets; for this reason, this type of research is strongly dependent on current technological advances (Thoroddsen et al., 2008). Such experimental equipment is very expensive when considering the computational time and purchasing costs. Additionally, the majority of the studies describing the splashing phenomena have been carried out in controlled laboratory experiments at low or moderate Weber ($< 3,000$) and Reynolds numbers ($< 30,000$). However, the drops commonly impact the surface at extremely high velocities, especially in the above-mentioned technical applications, leading to dimensionless impact parameters larger than $We > 5,000$ and $Re > 50,000$.

1.4 Objectives of the thesis

The main goal of this thesis was to elucidate the physics underlying the high-speed impact of single liquid drops on dry smooth surfaces and thin moving films. The first objective was to design a precise and robust experimental set-up in order to obtain reliable and statistical data for a large number of impact conditions. The second objective was to develop automated tools to analyze a large number of images and characterize the outcome of splashing in the presence of gas flow. The third objective was to perform numerical simulations to complement the experimental study, thus providing more detailed information on the impact dynamics, which can be hardly obtained in the experiments. The goal of this thesis was also to provide a comprehensive study of the influence of the physical properties of liquids and gases on the splashing of drops at very high Weber and Reynolds numbers.

This work analyzes the liquid spreading over the surface, the thin ejected lamella, and the ejected secondary droplets from the impact on a dry surface. In case of impacts on thin moving films, it describes the crown formation, geometry, and the break-up process. This thesis aims to provide an accurate physical description of the thin spreading lamellae and precise measurements of the size, velocity, angle, and the total ejected volume of the secondary droplets. This was achieved using multiple high-resolution and high-speed cameras from different perspectives. Another relevant objective of this study is to highlight the responsible instabilities triggering the break-up process during splashing within a large range of impact conditions. The analysis of the high-speed impacts together with an extension of some existing models allows predicting the entire outcome of splashing on dry and moving films. The detailed models proposed here can be indeed used to understand, characterize, and more accurately predict the underlying physics in several applications.

2 Experimental and numerical methods

The splashing of high-speed drops was studied using experimental and numerical methods. The experimental set up was designed from scratch, taking into account the efforts and lessons learned from the prototypes previously developed at the Institute of Fluid Mechanics in the TU Braunschweig. The experimental approach presented in this chapter allows to analyse the smallest ejected secondary droplets, the gas entrapment mechanism, and the rim formation and fingering. Part of the methodology described in this chapter has already been published in different research articles (Burzynski and Bansmer, 2018a, 2019a, Burzynski et al., 2020).

Numerical simulations were performed using OpenFOAM and its standards and validated libraries. The numerical results were used to complement the limitations of the experimental methods and to support the observations with a more detailed perspective. Especially, the simulations were used to analyse the flow dynamics of the surrounding gas and the spreading liquid over the surface. Part of the numerical methods has been presented in Burzynski and Bansmer (2019b).

2.1 Flywheel experiment

The high-speed impact of drops was investigated using a newly developed flywheel experiment designed by the author of this study. The basic idea of this kind of experiments is to achieve high impact velocities by mounting the impacting surface on a rotating flywheel. While the flywheel rotates at a constant angular velocity, drops are formed and released by a drop generator located on top of the flywheel. By synchronizing this release time with the flywheel, the drops impact on the fast-moving surface at the desired position.

The experimental set-up was designed on multiple modular systems, which allow studying the impact of drops on solid dry surfaces or thin moving films. Figures 2.1 and 2.2 show the main systems responsible

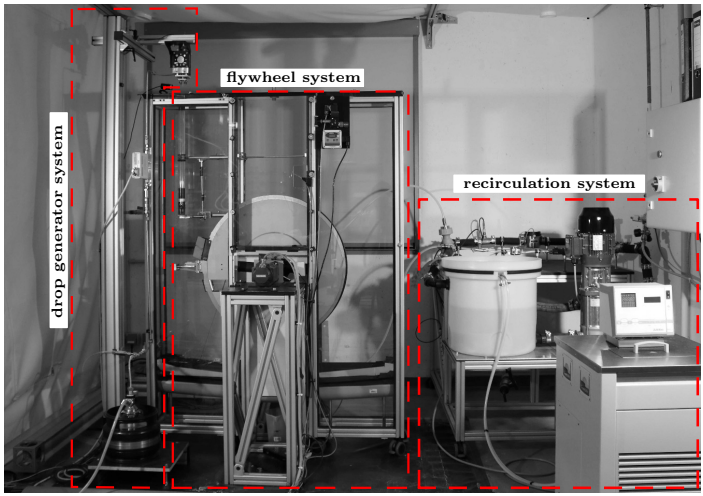

Figure 2.1: Flywheel experiment and its main functional systems.

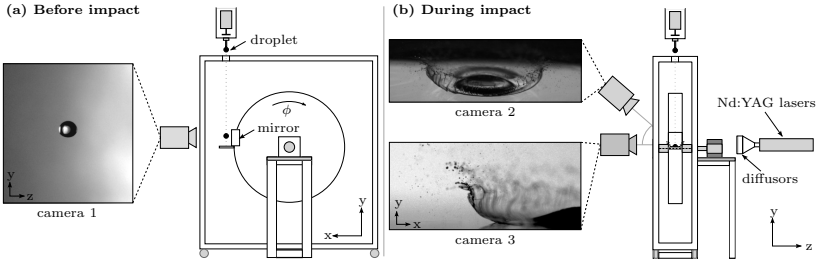

Figure 2.2: Observation methods. Sketches illustrate the shadowgraph set-up used to capture the small droplets. The images show an ethanol drop $D = 2.4$ mm impacting the surface at $U = 6.3$ m/s ($We = 3,300$, $Re = 9,500$). Adapted from Burzynski et al. (2020)

for the execution of the experiments. The experimental set-up consisted of a drop generator system, a flywheel with the impact surface mounted on it, a liquid film generator system, an observation system, data adquisition system, and a control system. Using such a set-up, it is possible to study the impact of drops with different physical properties, the impact on diverse surfaces and angles, and on liquid films of variable liquids, velocities, and thicknesses, etc.

2.1.1 Drop generator system

Part of the text described in this section has already been published in Burzynski et al. (2020).

The drops of diameter D were generated and released on demand by the droplet generator. This consisted of a cage with a solenoid and a needle where the drops are formed, as shown in figure 2.3. The drop liquid was pumped to this generator from a pressurised reservoir. The volumetric flux was measured and controlled using a Coriolis flow controller. Although the drop generator can be used to form drops of many different liquids, only three different liquids (distilled water, ethanol, and acetone) were used to investigate the effects of the physical properties of liquids and dimensionless parameters on the splashing outcome.

The drop generator allowed the formation of drops of different sizes, but mostly drops in the range from $D \approx 2$ to 4 mm in diameter (depending on the liquid used) were generated. The largest drops were generated using water, which due to the large surface tension allowed to generate drops with the sizes of 3.0 ± 0.21, 3.5 ± 0.23, and 4.0 ± 0.24 mm. When using acetone and ethanol, both with lower surface tension, it was possible to generate drops of sizes 2.0 ± 0.17, 2.5 ± 0.24, and 3.0 ± 0.22 mm. The drop size is controlled by the needle diameter and the amount of liquid pumped between each drop generation cycle. After the drop forms, it hangs at the tip of the needle until the solenoid is activated and, subsequently, the cage is hit by the plunger. The drop formation process was monitored with a small video camera during all the experiments.

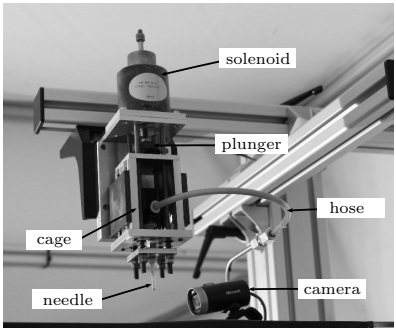

Figure 2.3: Droplet generator

After a liquid drop is released from the needle, it falls freely due to gravity for 80 cm (approximately 0.5 s) until it collides with the fast-moving surface with a velocity of $U_D = 3.3 \pm 0.2$ m/s. Previous studies performed by Faßmann et al. (2013) on this on-demand drop generator show that the drop shape after the pinch-off oscillates for until approximately 40 cm; after that, the drops become spherical. Such os-

cillation was confirmed during this study; however, it could be reduced to around 20 cm by forming as large drops as possible, decreasing the hitting power of the solenoid, and adding damping springs to the guiding bars. The drops were protected during the free fall by using a shielding tube with a closing plate at its ends, as shown in figure 2.4. This avoids additional perturbations and changes in the trajectory due to the surrounding gas flow generated by the flywheel. The closing plate is comparable to an automatic door, which opens just before the drop passes by.

The precision of the drop generator was quantified by measuring the size and velocities of multiple drops using a shadowgraph technique in an undisturbed environment, i.e., with the flywheel turned off. Details on the observation method used are explained in section 2.2. These results show that the size and velocities of the drops varied with a standard deviation of around 0.08 mm and 0.14 m/s, respectively. However, when the flywheel was rotating, the surrounding gas influenced the drops by deforming them, slowing them down, or changing their paths; as a consequence, the size and velocity of the drops just before impact was altered, and the standard deviations in the majority of experiments increased to a maximum of 0.25 mm and 0.96 m/s, respectively. These inevitable variations were the most significant source of uncertainties in the entire experiment. Nevertheless, as the size, shape, and velocity of all the drops were measured just before the drops collided with the surface, the impact conditions and standard variations are well known.

2.1.2 Flywheel system

Part of the text described in this section has already been published in Burzynski et al. (2020).

The main function of the flywheel is to move the impacting surface at a constant angular velocity ϕ and provide impact velocities higher than those achieved by just letting the drops fall (Faßmann et al., 2013, Li, 2013, Mehdizadeh et al., 2004). The impact velocity U is determined by the relative velocity between a falling drop U_D and the impact surface U_S. The fact that $U_S > U_D$ implies that the motion of the impacting surface has to be very accurate and precise; otherwise, the impact conditions would continuously change. For this reason, a synchronous servomotor (1FK7042-2AC71-1TB0) from Siemens, which was one of the most precise motor available, was chosen to drive the flywheel. After a static and dynamic balance of the flywheel, a small

variation of around 3% of the set velocity was measured for the lowest rotation speeds. This deviation decreased down to $< 1\%$ for velocities higher than 5 m/s. The flywheel could be used to investigate the impact of drops at a maximum velocity of $U_S = 28$ m/s.

The impact velocity U was varied depending on the configuration set from 3 to 30 m/s. The uncertainties in the impact velocity mainly depend on the drop deceleration caused by the surrounding gas during the drop free fall. This effect was minimised by using the above-mentioned shielding system and quantified by measuring each drop some milliseconds before the impact. The water drops are less sensitive to the perturbations caused by the fast-moving flywheel than the other liquids due to their larger size and surface tension. In the case of $U < 10$ m/s, the standard deviation was smaller than 0.27 m/s; for higher impact velocities, it increased slightly to 0.49 m/s. When using acetone or ethanol and in the case of $U < 8$ m/s, the standard deviation was 0.30 m/s; for higher impact velocities, the standard deviation was 0.54 m/s.

These uncertainties of the flywheel resulted in a maximal variation of the surface position of ± 1 mm for the low impact velocities. The variation of the surface position led to a small variation of the impact angle of $90 \pm 0.25°$; subsequently, the horizontal velocity during the impact was lower than 0.4% of impact velocity U, making its influence on splashing negligible. Another factor that can be analysed during the splashing is the effect of the centrifugal force $\sim R_F \phi^2$ caused by the rotation of the fast-moving flywheel. With a radius of $R_F = 0.45$ m, the centrifugal force compared to the dynamic force of the impact $\sim U^2$ was very small. This ratio was less than 1% due to the high impact velocity, allowing to also neglect the influence of the centrifugal force during the analysis of the splashing process.

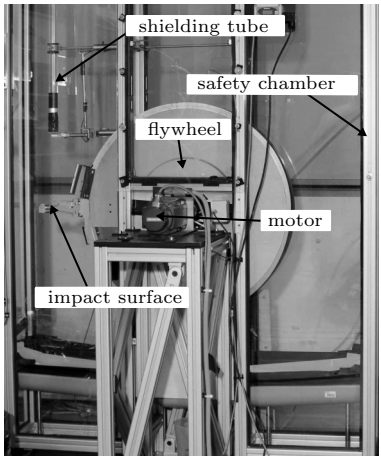

Figure 2.4: Flywheel system

The flywheel was surrounded by a safety chamber, which consisted of safety glasses and a funnel-like collecting bottom, as shown in figure 2.4. The function of the chamber was to protect the research personnel

in case of any failure and detachment of parts and from any contact with the moving flywheel, which can be lethal when rotating very fast. It also prevented the used liquids from spilling onto the measurement equipment. Further details on the design can be found in the internship report of Haar (2016), which includes stress analysis, material selection, geometrical integration, etc.

After sealing the safety chamber, it was possible to fill the chamber with a different gas. This was done by letting the gas contained in a pressurized bottle to enter the chamber through a small hole; at the same time another small hole lets the air escape from the chamber to some extent. Making use of this method, a gas mixture was always present inside the chamber. The oxygen concentration χ_{O_2} and the absolute pressure p were measured next to the impact position using an oxygen transmitter (OXY 3690 MP) from Greisinger and a pressure transmitter (CTE8001) from Frist Sensor. The sensor information was used to control diverse opening valves, which let the pressurised gas enter the chamber and clean the impact surface at the same time. The oxygen concentration varied regardless of the used gas within a range of 3%. Using the information provided by both sensors, the physical properties of the gas mixture formed with the air were calculated as demonstrated in (Jenning, 1988, Wilke, 1950). Details on the impact conditions are outlined in section 2.1.4.

2.1.3 Film generation system

Part of the text described in this section has already been published in Burzynski and Bansmer (2018a).

A robust film generator system was designed to study the high-speed impact of drops on a thin moving film using the above-mentioned flywheel. The generation of a liquid film on a rotary system is a very challenging task. On the one hand, the fluid has to be provided continuously from the outside of the flywheel onto the impacting surface. On the other hand, the film has to be extracted and reused from the flywheel to avoid any unnecessary waste of liquid. Additionally, if the extraction does not take place, the distinction between the secondary droplets and the film scattered all around by the flywheel cannot be made. For this reason, a recirculation system was designed to perform both the injection and the extraction of the film, as shown in figure 2.5.

The film liquid (distilled water, ethanol, or acetone) was stored in a 40-litre reservoir and pumped by a multistage centrifugal pump into two subsystems: one for the injection and the other for the extraction.

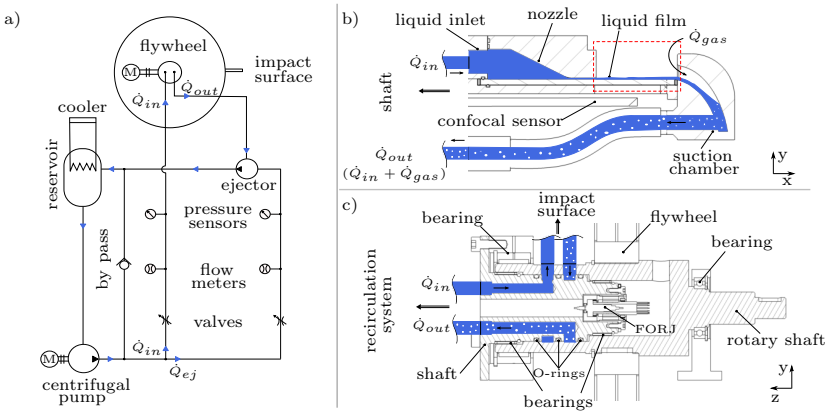

Figure 2.5: Film generation system. (a) shows a sketch of the recirculation system. (b) shows the impact surface and the confocal sensor. (c) shows the shaft used to transport the liquid from the reservoir to the impact surface. Adapted from Burzynski and Bansmer (2018a).

In *the injection subsystem*, the fluid was transported directly into the flywheel. Before it entered the flywheel, the flow rate $\dot{Q}_{in}$ and the pressure were measured to control the conditions of the fluid. A diaphragm valve attached to the measurement equipment regulated the rate of the flow onto the flywheel. By measuring and regulating the flow rate, it was possible to estimate the mean exit velocity of the film due to mass conservation $U_{f,exit} = \dot{Q}_{in}/A$, where A represents the exit area at the impacting surface. Note that the mean exit velocity differs slightly from the mean velocity of the film at the impact location due to a small change in the cross-section area. The film thickness measurements, covered in the next subsection, and the images of the tilted camera show that the cross section area changes around 5% after exiting the nozzle. Since this variation is small, the mean velocity of the film U_f is expected to equal the mean exit velocity $U_{f,exit}$. After the flow rate and the pressure were measured, the fluid passed through two hollowed shafts, as illustrated in figure 2.5(c). Once the liquid reached the surface-holding modules, a nozzle was used to accelerate and form the thin fluid film directly onto the impacting surface, as shown in figure 2.6. The film then passed through the observation window and ended up in a suction chamber, where it was mixed with the surrounding gas, as shown in figure 2.5(b).

An ejector was connected to the liquid recirculating in *the extraction*

subsystem $\dot{Q}_{ej}$ to bring the liquid film from the suction chamber back to the reservoir, as shown in figure 2.5(a). This ejector continuously created a low-pressure zone inside of it, sucking the liquid-gas mixture $\dot{Q}_{out}$ from the suction chamber through the hollow shafts. This liquid-gas mixture flow $\dot{Q}_{out} + \dot{Q}_{ej}$ was then transported directly to the reservoir to close the loop. As in the injection subsystem, the use of a diaphragm valve and the measurement of the flow rate and pressure allowed to control the suction power of the ejector. A bypass was also used as a pressure regulator to establish optimal conditions in the flow before it entered the two subsystems. The continuous pumping of the liquid led to an increase in its temperature. To control this, an ultra-low refrigerated circulator (FP51-SL) from Julabo was connected to the reservoir, keeping the liquid at a constant temperature of $T = 20 \pm 0.5°\text{C}$.

Film thickness measurement

The thickness of the film on the substrate was measured using a confocal chromatic measurement system from Micro-Epsilon. This system consisted of an IFC2451 controller and an IFS2902/90-4 miniature sensor model, which was mounted under the substrate, as shown in figure 2.5(b). The controller generated a polychromatic light, which was sent to and returned from the sensor. Inside this sensor head, a combination of lenses dispersed the light such that different wavelengths were

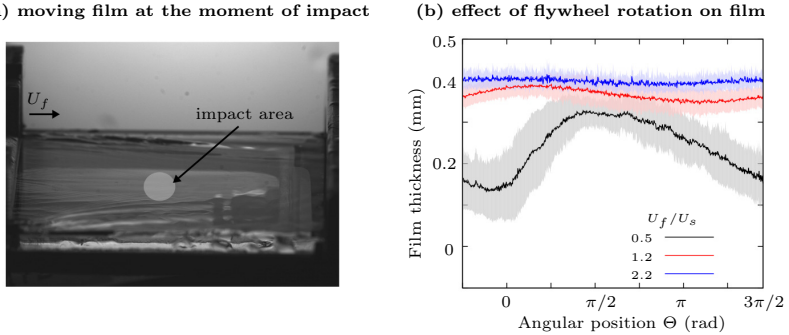

Figure 2.6: The liquid film at the moment of impact. (a) shows the capillary waves on the moving film and the impact area. (b) shows the effect of different film velocity ratios U_f/U_S on the film thickness and angular position. The grey area represents the standard deviation.

focused at different distances from the sensor head. The distance from an interface to the sensor was determined by the reflected wavelength. This method allows measuring the thickness of transparent materials and liquids. The white light was transferred from the controller to the sensor and vice-versa through the FORJ mounted on the fixed shaft. This approach allowed for measuring and controlling the thickness of the film during the experiments involving the rotation of the flywheel.

The use of the confocal sensor allowed to quantify the changes in film thickness during the experiments. Figure 2.6(b) shows an example of this by demonstrating the strong effect of gravity on the film thickness; however, the effect of gravity decreases asymptotically by increasing the angular velocity or flow rate. It could also be observed that the film at the moment of impact $\Theta \approx 0$ is the smallest possible film because the gravitational force acts totally perpendicularly to the free surface. Additionally to these effects, the measurements demonstrated that the film thickness also depends on the liquid velocity and the rotation speed of the flywheel. As the film velocity increases, the film thickness approaches the set height of the nozzle exit, and the film becomes more stable. Therefore, it is essential to measure the film thickness when a flywheel experiment is carried out.

Significant efforts have been made to generate a thin and stable liquid film; however, this is a major challenge due to the large number of perturbations applied on the liquid when transporting it from the reservoir to the impact surface. Small stationary waves, which were reduced by increasing the angular velocity of the flywheel, were observed during the commissioning and experiments, as shown in figure 2.6(a). This occurred due to the relatively large stagnation pressure at the surface, which pushed the film against the surface, reducing the amplitude of the small disturbances. The film thickness varies due to these surface waves between 0.3 and 0.4 mm in the worst-case scenario, namely water film with a static flywheel. When the flywheel rotates, the variation of the film thickness is smaller than 5% of the film thickness set. Nevertheless, Adebayo and Matar (2017) demonstrated in a detailed parametric study that such capillary waves do not notably affect the impact outcome in comparison to a completely flat film.

2.1.4 Impact conditions

Part of the text described in this section has already been published in Burzynski et al. (2020).

The flywheel experiment was designed to investigate the impact of almost any kind of liquid at low and high impact velocity; however, this study is restricted to the use of distilled water, ethanol, and acetone. The physical properties of these liquids are shown in table 2.1. The same liquid is used for the drop and the film when studying splashing in thin films, thus the impact of drops on different liquids is beyond the scope of this thesis. All the experiments were conducted with a glass surface of maximal roughness of $R_a = 22 \pm 5$ nm as the impact surface and under normal absolute pressure $p = 1,050 \pm 100$ hPa and room temperature of $T = 20 \pm 3°\mathrm{C}$.

Liquids	Density ρ_l (kg/m^3)	Viscosity μ_l (mPas)	Surface tension σ (mN/m)
Water	998	1.002	72.75
Ethanol	790	1.240	22.55
Acetone	790	0.303	23.30

Table 2.1: Fluid properties and the range of impact conditions used.

As this work focuses on the splash generated on dry and wetted surfaces, different set-ups were used for each case. In the case of experiments on a dry surface, the surface has to be dried and cleaned between each impact interval, which was chosen to be 5 s. During this time, the recirculation system was turned off, and two hoses connected to the sides of the experimental set-up blew gas or air at 5 bars directly onto the surface, removing the remaining liquid from it. The centrifugal force, the evaporation of the liquid, and the fast-moving gas flow at the surface helped to remove the remaining liquid between impacts. Different gas mixtures were used to investigate the role of the surrounding gas on splashing on a dry surface. Table 2.2 shows the calculated physical properties of the used gases.

In the case of experiments on a wetted surface, the film generator system was turned on, and each drop impacted the surface at 5 s intervals. The confocal sensor was located under the impacting surface, measuring the film thickness continuously. The liquid temperature in the reservoir was kept constant to $\sim 20°\mathrm{C}$, which is the same temperature as that of the liquid drops. The height of the nozzle exit was set to 0.3 mm and 0.1 mm to investigate the effects of the film thickness. The velocity of the film varied in the range from 0.5 m/s to 2 m/s with

	He(95%)	He(70%)	NH_3(77%)	NH_3(54%)	Air
ρ_g(kg/m^3)	0.22	0.48	0.83	0.94	1.21
μ_g(μPas)	20.3	18.9	12.7	14.8	18.2
λ_g(nm)	173	110	55	60	66
	O_2(95%)	Ar(79%)	CO_2(41%)	CO_2(74%)	SF_6(39%)
ρ_g(kg/m^3)	1.32	1.56	1.46	1.67	3.22
μ_g(μPas)	20.3	21.7	16.1	15.2	16.4
λ_g(nm)	70	69	53	47	36

Table 2.2: Gas properties calculated during the experiments. The pure gas concentration χ of each gas mixture is shown in parenthesis.

an uncertainty of around ± 0.1 m/s during each measurement. It has to be kept in mind that an increase in film velocity leads to inevitable increment in the film thickness, as shown in figure 2.6(b). The table 2.3 summarises some of the set impact conditions studied, excluding the case of analyzing the surrounding gas effects, where the impact conditions remained constant ($We \approx 5,000$ and $Re \approx 35,500$). This table provides only an idea of the impact conditions set as goals at the beginning of the study. The advantage of having relatively large variations of the boundary conditions between single impact events and at the same time measuring each drop prior the impact allowed to cluster the results from all the measurements and analyze the data within a wider range of impact conditions.

2.2 Observations techniques

Part of the text described in this section has already been published in Burzynski et al. (2020).

The observation of splashing was made using the shadowgraph technique with different cameras and locations, as illustrated in figure 2.2. The main observation set-up consisted of three high-resolution double-frame cameras PCO.4000 (4008×2672 pixel) and two pulsed Nd:YAG lasers with diffuser optics serving as light sources. Camera 1 was used for the characterisation of the primary drops before they impact the surface, providing the impact conditions. Camera 2 was used for the observation of the atomisation process and the corona structure from the inside. Camera 3 was used for the observation of the kinematics of the corona development and the characterisation of the secondary droplets. Some selected cases were observed using either an HPV-2

No.	Drop Liquid	h_f	u_f	We	Re
1	water	-	-	5,000	35,500
2	water	-	-	10,000	54,500
3	water	-	-	20,000	74,500
4	ethanol	-	-	3,500	10,000
5	ethanol	-	-	7,000	14,000
6	ethanol	-	-	12,500	18,000
7	acetone	-	-	3,500	38,000
8	acetone	-	-	7,000	62,000
9	acetone	-	-	12,500	84,000
10	water	0.05	0.05	2,200	20,500
11	water	0.13	0.15	2,200	20,500
12	water	0.14	0.30	2,200	20,500
13	water	0.20	0.05	2,200	26,000
14	water	0.30	0.02	4,500	36,500
15	water	0.03	0.04	4,500	29,000
16	water	0.04	0.10	4,500	29,000
17	water	0.05	0.20	4,500	29,000
18	water	0.30	0.01	5,700	42,000
19	water	0.60	0.01	8,800	51,000
20	water	0.45	0.01	11,000	57,000

Table 2.3: Set of conditions for impacts on dry and wetted surfaces. The absence of film quantities indicates the impact on dry surfaces.

high-speed camera from Shimadzu (312 × 260 pixel) or a v-711 (max. 1280 × 800 pixel) from Phantom, where the field of view is illuminated by a conventional halogen lamp. In such cases, the cameras were located as shown for camera 2 or 3 in figure 2.2. Regardless of the cameras used, the lenses used were a 180 mm Tamron objective with a 2× teleconverter or a Questar QM 100 long-distance microscope.

The impact captured with the high-speed cameras allowed for a good temporal resolution but a poor spatial resolution; therefore, they could be used to analyse the very small secondary droplets ejected from splashing. On the other side, the images taken with the high-resolution camera configuration allowed for a spatial and temporal resolution of 5 μm/px and 10 μs between the two frames, respectively. In such a case, only droplets with a minimum area of 3 × 3 pixels in the camera were evaluated, avoiding a false positive detection due to pixel noise. This constraint permitted reliable characterisation of droplets larger than 15 μm.

The gain in spatial resolution within this double-frame system resulted in a low temporal resolution, allowing to take only two images per impact. To compensate for this loss, more than 1,000 drop im-

pacts were captured for each condition at different elapsed times, thus creating a solid statistical database (see table 2.3).

Another important characteristic of the observation system is the limiting depth of field (DOF) caused by the use of conventional lenses. A limited DOF means that the droplets closest to the focal plane are likely to be detected, while the droplets further away are blurry or not detected at all. The quantity and size of detected droplets were proportional to the DOF because larger droplets were recognised even if they were out of the focal plane (Kim and Kim, 1994). This limitation led to a bias in the evaluation of the size distribution and volume ejected, which must be corrected. Therefore, the control volume in the direction of depth was calibrated by traversing a target plate. The calibration provided the correlation between the depth of field ψ and droplet size d, which was then used to correct the statistical results and extrapolate the counted droplets.

The synchronisation of the cameras with the drop-release point and flywheel was made using a Standford DG535 delay generator. Upon receiving the triggering signal from a light barrier mounted on the flywheel, the generator in its turn sent two signals with different delays: the first one caused the solenoid to release the pendant droplet and the closing plate to be open an instant later; the second signal triggered the cameras a few milliseconds after the drop was released to record the splashing. During the entire splashing process, the displacement of the surface in the vertical direction was smaller than 2 mm. The cameras were synchronised with the flywheel, i.e., impact surface; therefore, the camera captured the impact with the surface always in the same position.

2.3 Analysis of the recorded data

Part of the text described in this section has already been published in Burzynski and Bansmer (2019c) and Burzynski et al. (2020).

In this thesis, different methods and cameras were used to analyse the impact of drops. In most cases, the high-speed images were analysed using an in-house code developed in Matlab. This code uses the package Image Processing Toolbox to crop and align the images and to determine the conditions before the impact and the geometry of the liquid spreading or the ejected corona. The characterisation of the shadows detected (drop before the impact or the ejected liquid) was done by binarizing the grey images using a threshold value of 0.22.

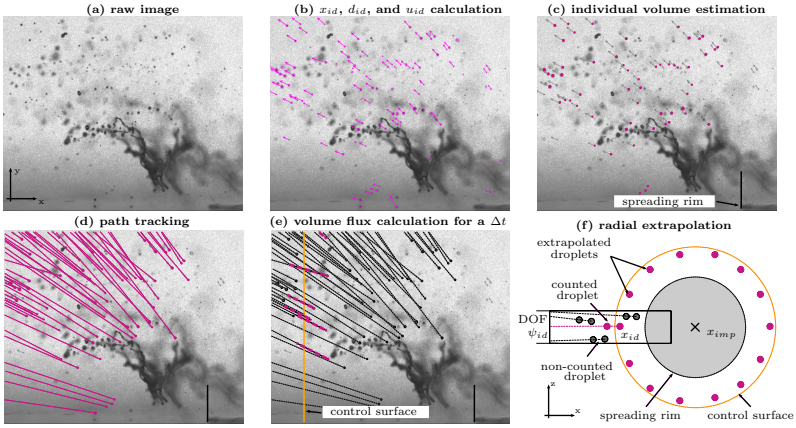

Figure 2.7: Post-processing of the high-resolution images. (a) shows a raw image with the secondary droplets ejected from a detached corona and (b) the droplet data calculated using the DaVis-ParticleMaster software. The main steps to estimate the total ejected volume using the extrapolation method are illustrated in (c-f). Adapted from Burzynski et al. (2020).

This value represents a global threshold, which specifies the degree of luminance where the drop area is recognised. The range of luminance from a single image varied between 0 and 1. By obtaining this information for each frame, it was possible to determine the drop position, size, and velocity prior to the impact and the height and diameter of the corona. All cameras were calibrated using the target plate ParticleMaster from LaVision at the focal plane. This calibration process allowed to determine a 3% uncertainty in the drop shape detection.

The drop impacts captured with the high-resolution cameras were analyzed using the commercial software DaVis-ParticleMaster (Berg et al., 2006). The operations provided by this software to detect and calculate the position, size, and velocity of the droplets can be found in Kapulla et al. (2008). The recognition of multiple droplets as one larger droplet was avoided by setting a small depth of field and analyzing only the droplets with a deviation between the diameters in the major and minor axes lower than 20%, as shown in figures 2.7(a,b). The total ejected volume was calculated by extrapolating the detected secondary droplets in the focal plane around the impact center. This method was first used by Weiss (1993) and later adapted by Faßmann et al. (2013)

considering the individual DOF of each detect drop. However, this adapted method needs to be corrected using weighting factors since the volume flux was calculated using the image borders as a control surface. As the impact center x_i changes from impact to impact, the distance between impact center and control surface varies, leading to a wrong estimation of the ejected volume (Faßmann, 2015). On the contrary, the method used for the analysis in this thesis is the one presented previously in Burzynski and Bansmer (2019c), which does not need to be corrected since the volume is only extrapolated from the droplets passing over a fixed control surface at 1.1 times the maximal spreading. The basic algorithm steps of this method were performed in Matlab and illustrated in figure 2.7(c-f). The following five steps were used to estimate the ejected volume flux:

(i) First, the volume of each detected droplet V_{id} was determined using the measured diameter d_{id} and assuming sphericity of 1. This was particularly the case some instants after the droplets were ejected from the spreading lamella. The volume then reads $V_{id} = \pi d_{id}^3/6$.

(ii) Second, the position of the droplets x_{id} over time was estimated using its measured velocity u_{id} for the entire splashing process. This position allowed to estimate the distance from the droplets centroid to the impact center x_{imp}.

(iii) Third, the droplets that passed through a fixed control surface at 1.1 times the maximal spreading or corona diameter were counted. This approach provided the volume flux of the ejected droplets at a specific time and therefore helped to avoid a single droplet being counted multiple times during the splashing.

(iv) Fourth, a radial extrapolation of the counted droplets was performed around the impact center x_{imp}. One simple possible approach to perform this extrapolation is to multiply the volume of the counted droplets by the factor 2π for each time interval of Δt. However, this would lead to an overestimation of the secondary volume since the amount and size of the secondary droplets depends on the depth of field, which in such an approach is not taken into account. To correct that, the calculated DOF values were considered for each droplet ψ_{id}. The extrapolated volume

flux for a time interval Φ_s was then calculated as

$$\Phi_s = 2\pi \sum_{id=1}^{N} \frac{(x_{id} - x_{imp})}{\psi_{id}} V_{id}, \tag{2.1}$$

where x_{id} is the droplet position before crossing the control surface, as illustrated in figure 2.7(f).

(v) Fifth, the total ejected volume during the splashing process was obtained after integrating the extrapolated mean volumetric flux Φ_s over time. This method is valid for impact normal to surfaces, where all secondary droplets spread almost equally in the azimuthal direction.

Using this approach to calculate the total ejected volume, a small volume was omitted since only droplets larger than 15 μm were evaluated. However, the volume contribution of very small droplets $V_{d=3\mu m} = 1.41 \times 10^{-17}$ m^3 is insignificant in comparison with the volume of larger droplets $V_{d=50\mu m} = 6.54 \times 10^{-14}$ m^3. This occurs because the volume is proportional to d^3; consequently, the smallest droplets are less dominant in the total volume distribution. Thus, it was not expected that the total extrapolated volume would be greatly affected when capturing all droplets smaller than 15 μm. Note that the uncertainty s of a measured quantity γ, such as the diameter or velocity of the ejected droplets, is calculated throughout this thesis as

$$s_\gamma = \left(\frac{1}{n-1} \sum_{i=1}^{n} [\gamma_i - \overline{\gamma}]^2 \right)^{1/2}, \tag{2.2}$$

where n is the number of samples and $\overline{\gamma}$ is the mean value of the quantity.

Since the total ejected volume is not measured directly but rather calculated by equation 2.1, the uncertainties of the results depend on the errors measured for each variable (Coleman and Steele, 2009). These errors propagate and contribute separately to the decrease in the level of confidence of the results. Faßmann (2015) performed a detailed analysis of the error propagation when calculating the total ejected volume. The uncertainties presented in this thesis were analyzed in accordance with his work. As a result, the error propagation analysis indicates that the error of estimating the total ejected volume is relatively small ($\sim 10^{-10}$ mm^3). This is because the droplet positions and sizes used in equation 2.1 are measured directly. However, the major contribution

to the uncertainties results from the clustering of similar impacts. This is due to the fact that even when the impact conditions are almost the same, the break-up process always leads to a different number of ejected drops. These inevitable variations were the most significant source of uncertainties in the entire experiment.

2.4 Numerical simulations

The numerical simulations were used in this thesis to provide information about the velocity fields inside the spreading lamella and the surrounding gas, which are challenging to obtain using experimental methods. Although the simulations are complementary to the extensive theoretical and experimental investigations of this thesis, the results were used to improve the interpretation of the complex impact dynamics. The numerical simulations were performed using the open-source code OpenFOAM and the toolboxes available in version 2.3.1. This code was chosen due to the modular code structure and the wide range of functions available for complex multiphase flows, which have been validated in several studies (Berberović et al., 2009, Iturrioz et al., 2015, Jasak, 2009, Moukalled et al., 2016). All the simulations were performed using the *multiphaseInterFoam* solver, which is based on the Volume of Fluid (VOF) method for interface tracking and takes into account surface tension effects for N number of incompressible fluids (Greenshields, 2019). Using this solver, the incompressible Navier-Stokes equations that had to be solved directly in the finite volumes are:

$$\frac{\partial u_i}{\partial x_i} = 0, \qquad \text{and} \tag{2.3}$$

$$\frac{\partial u_i}{\partial t} + u_j \frac{\partial u_i}{\partial x_j} = -\frac{1}{\rho}\frac{\partial p}{\partial x_i} + \nu \frac{\partial^2 u_i}{\partial x_j^2} + f_{\sigma,i} + f_{g,i}, \tag{2.4}$$

where the source terms $f_{\sigma,i}$ and $f_{g,i}$ represent the surface tension and gravity, respectively. In addition to these equations and in accordance with the implemented algebraic VOF methodology (see Hirt and Nichols (1981)), the volume fraction α of a given fluid n had to be introduced to track the interface of each fluid (Berberović et al., 2009). This scalar represents how much volume of a specific fluid is occupied in a given control volume; therefore, it can vary between 0 and 1. The transport equation for this volume fraction α is expressed as

$$\frac{\partial \alpha}{\partial t} + \frac{\partial \alpha u_i}{\partial x_i} = 0. \tag{2.5}$$

This kind of representation allowed to treat the multiple fluids as a one effective fluid in the entire domain, while the corresponding physical properties of each fluid were calculated as weighted averages based on α as

$$\rho = \rho_n \alpha + (1 - \alpha)\rho_0, \qquad \text{and} \tag{2.6}$$

$$\mu = \mu_n \alpha + (1 - \alpha)\mu_0, \tag{2.7}$$

where the subscript n represents a given fluid and 0 the reference phase, which in this study is the surrounding gas.

To account for the surface tension effects, Brackbill et al. (1992) proposed to calculate the source term $f_{\sigma,i}$ using the surface curvature κ as $f_{\sigma,i} = \sigma\kappa\partial\alpha_i/\partial x_i$. However, the surface tension term suffers from the fact that the surface curvature within the VOF method $\kappa(\alpha)$ cannot be calculated accurately since the interface of a given fluid varies between 0 and 1 and is never sharp. To overcome this problem with the actual *multiphaseInterFoam* solver, a large number of cells have to be used in order to reduce the physical length of the diffused interface.

2.4.1 Computational set-up

The simulations of drop impacts on dry and wetted surfaces were performed in an axisymmetrical set-up, where the mesh geometry was generated using the *blockMesh* utility. Figure 2.8(a) gives an example of the entire computational domain for the different studied cases. To estimate the size of the cells required to simulate the splashing phenomenon, the thickness of the lamella at the ejection time was first calculated as a reference using the theory of Riboux and Gordillo (2014). Further details on how this estimation was done can be found in section 3.4.4. The theory predicts that for a water drop of $D = 3$ mm impacting at $U = 10.79$ m/s ($We = 5,000$ and $Re = 32,264$), the lamella at the moment of ejection is around 3 μm thick, and the thickness increases over time. The region near to the center, where the lamella is expected to be ejected, is refined. The refinement leads to cells of around 1.56 μm and 0.23 μm in x and y direction, respectively. This resolution allowed to capture the thickness of the ejected lamella with at least ten cells. The cell size expanded uniformly outward the refinement area, resulting in a total number of cells of around 5×10^6 in the entire computational domain of 10×10 mm^2. This computational set-up is the result of a grid convergence study, in which the minimal

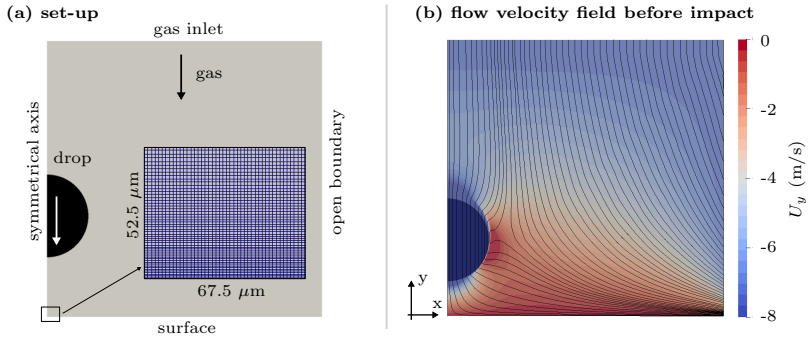

Figure 2.8: Computational set-up. (a) shows the axisymmetrical set-up used during the simulations and an example of the grid size. (b) shows the velocity field and the streamlines prior the impact.

grid resolution needed to correctly solve the dynamics of the spreading film is determined. The discussion about this convergence study is included in the following section.

One important feature of these simulations is that it was set up to reproduce the impact as similar as possible to the experimental configuration; therefore, the relative gas flow around the impacting surface was taken into account, as shown in figure 2.8(b). The boundary conditions in the axisymmetrical simulations were defined in 6 patches, where the axis of symmetry and the wedge front and back patches were three of them. The remaining three patches were used to define the gas inlet, outlet, and surface, as shown in table 2.4. The drop center was located at a specific height so that it would contact the surface $\tau = tU/D \approx 0.2$ after the simulation was started. The drop velocity was given by the impact velocity U, while the gas velocity was set as the velocity of the flywheel U_S.

The computational set-up for a drop impacting on a moving liquid layer was similar as the one used when studying the impact on dry surfaces. However, it has to be pointed out that it is not possible to replicate the complex and three-dimensional dynamics of a moving film in an axisymmetric simulation. For this reason, the numerical simulations were performed to obtain information about the dynamics only in the downstream direction. As shown later in section 4.5, the dynamics in this direction are the most interesting since the hole formation and break-up started from this location. The numerical simulations in this case were performed also for a $D = 3$ mm drop impacting at

Quantity	Inlet	Open boundary	Surface
α_0	inletOutlet	zeroGradient	static contact angle
α_n	inletOutlet	zeroGradient	zeroGradient
U	fixedValue	pressureInletOutletVelocity	fixedValue = 0
p	zeroGradient	totalPressure	fixedFluxPressure = 0

Table 2.4: Overview of the boundary conditions.

$U = 10.79$ m/s ($We = 5,000$ and $Re = 32,264$), but the drop impacted on a water film of $h_f = 0.1$ mm moving at $U_f = 1$ m/s. To keep the film flowing while the drop is in a free fall, an inlet boundary condition of the same height as the film was included in the symmetrical axis.

All the numerical simulations presented here were run without turbulence models and using the same numerical schemes. The set of these schemes was based on the results of a detailed parametric study conducted to obtain accurate and stable simulations. In order to guarantee that the volume fraction remains between 0 and 1, the multidimensional universal limiter for explicit solution (MULES) was used to solve the equation 2.5. This method had to be defined together with a limiter to treat the volume fraction advection; the applied limiter equaled 1 in the interface area and 0 in the rest of the domain. When the limiter was 1, the advection was treated using an interfacial compression flux and high-order schemes; however, when it was 0, the advection was calculated using a first-order upwind scheme (Deshpande et al., 2012).

The time derivatives ($\partial/\partial t$) were discretized using an implicit first-order upwind Euler scheme, while the gradient terms were estimated using the Gauß's theorem with linear interpolation or central differencing (Greenshields, 2019). For the momentum flux (div $(\rho u_i u_j)$), a second-order total variation diminishing (TVD) scheme with limited linear differencing was used with a coefficient of 1. A coefficient of 0 gives the best accuracy, while 1 provides the best convergence (Greenshields, 2019). The divergent terms (div (αu_i)) were discretized using another second order TVD scheme based on the formulation proposed by Van Leer (1974). The advantage of using TVD schemes when solving the velocity gradients is that they switch from a high-order to a low-order scheme regardless of discontinuity (phase change) being present or not (Zhang et al., 2015). Laplacian terms (typical for the diffusion term in the momentum equation) were discretized using the Gauß's theorem. A limiting correction in the Laplacian term was used to treat the mesh non-orthogonality between the center-to-center vector and the face normal vector, which can produce a negative diffusion and

generate instabilities in the calculation. The correction allows a plausible physical value of the diffusion term regardless of the degree of mesh non-orthogonality (Moukalled et al., 2016). All these discretization methods are summarized in Table 2.5. Further information on the methods, their implementation, and the applied mathematical concepts can be found in the user guide presented in Greenshields (2019) and the comprehensive works of Berberović et al. (2009), Jasak (2009), Kuzmin et al. (2012), Moukalled et al. (2016).

Terms	Scheme	Order
$\partial/\partial t$	Euler	1
grad Φ	Gauss linear	2
div $(\rho u_i u_j)$	Gauss limitedLinearV 1	2
div (αu_i)	Gauss vanLeer	2
div(gradΦ)	Gauss linear corrected	2

Table 2.5: Overview of the numerical schemes with Φ as a given scalar.

2.4.2 Verification of the numerical approach and comparison with experiments

The numerical results are verified using the experimental data available in order to corroborate the accuracy of the simulations. A quantitative verification was done by analyzing the spreading diameter with different grid resolutions and at multiple impact times, while a qualitative verification was obtained by comparing the high-resolution images obtained in the experiments. This approach has been widely adopted by many authors when studying the drop impact dynamics (Guo and Lian, 2017, Raman et al., 2016, Shetabivash et al., 2014).

The grid convergence study was performed with a total of seven different grids. The first set-up was run with a coarse grid containing $\approx$ 78.000 grid points; subsequently, the number of grid points was increased until a fine grid was obtained with approximately 15 million points. The spreading diameter was determined using the advancing contact point with the surface, as shown in figure 2.9(a). The result of this convergence study demonstrated that the coarse grids with less than 1 Mio. points do not predict the diameter of the spreading lamella correctly at larger impact times ($\tau > 1$). However, as shown in figure2.9(b), the numerical simulations show agreement with the experiments also at later impact times when the number of grid points is increased. As the numerical results were used to analyze the spreading

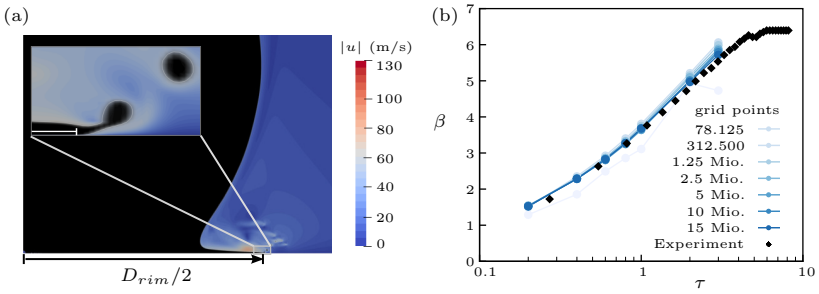

Figure 2.9: Verification of the numerical simulations. (a) shows an impacting drop and the estimation of its spreading diameter. (b) shows the grid convergence study for different time steps and the comparison with the experiments of Burzynski and Bansmer (2018b).

liquid film and the surrounding gas at the early stage of impact ($\tau < 1$), the numerical simulations were then performed using only the set-up with 5 Mio grid points. This set-up predicts a spreading diameter of 11.2 mm at $\tau = 1$, while the experimental data indicates 11.3 mm. The set-up with 15 Mio. grid points at the same predicts the impact time and the spreading diameter of 11.2 mm, demonstrating that up to this time point, the results do not depend on the grid size, as shown in figure2.9(b). To demonstrate the sufficient resolution of the numerical simulations in the gas phase, the thickness of the laminar boundary layer of the moving gas prior the drop impact was estimated over the entire domain as $\sim 5(\nu_g x/U_S)^{1/2}$, where $x = 0.01$ m and $U_S = 7.5$ m/s. This estimation suggested that the boundary layer is around 0.7 mm thick and therefore is resolved in the computation set-up selected with more than $3,000$ grid points.

The qualitative verification of the numerical simulations was performed using the high-resolution images obtained during the experiments, as shown in figure 2.10. Although the comparison seems to be a priori in good agreement with the experiments, the numerical simulations were not performed to reproduce the complex and three-dimensional dynamics of the lamella break-up. This is very challenging due to the different large scales to be solved, especially for the cases shown here with low viscosity liquids. For example, the length and time scales to be solved for a water drop impacting at high velocity varied from millimetres ($\sim D$) and milliseconds ($\sim D/U$) down to ($\sim \rho_l \nu_l^2/\sigma \approx 13.8$) nanometres and ($\sim \rho_l^2 \nu_l^3/\sigma^2 \approx 0.19$) nanoseconds,

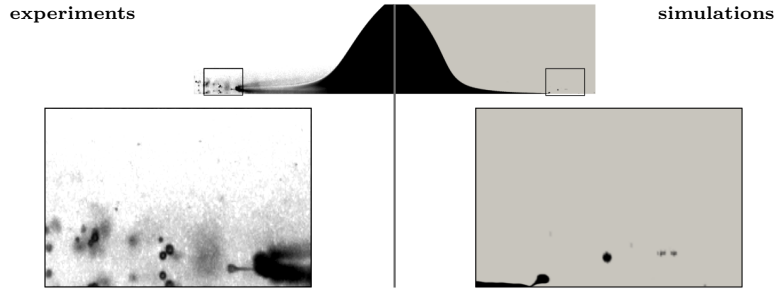

Figure 2.10: Comparison of the numerical results with the experiments involving a water droplet impacting at $We = 5,000$. The axisymmetrical simulations describe the spreading lamella fairly well.

respectively (Eggers and Villermaux, 2008).

In addition to the quantitative verification done using the spreading diameter, the results of the computational set-up chosen were also compared with the size and velocity of the secondary droplets ejected during splashing. It has to be highlighted that what was observed as droplets in the axisymmetrical simulations were rings or tori and not spherical droplets. However, the study of Dodds et al. (2012) demonstrated that the shape and volume of resting droplets after the break-up remain the same when comparing axisymmetric and three-dimensional simulations. A similar conclusion is found in the investigations of Malgarinos et al. (2017), Zhou et al. (2010), indicating that the three-dimensional effects, such as viscosity and surface tension, have a weak influence on the dimension and shape of the ejected droplets. Hence, the diameters obtained by the tori in a very refined mesh can provide a fair estimation of the diameter of the ejected secondary droplets. To corroborate this assumption, the tori diameters were compared with the predictions made by the theory of Riboux and Gordillo (2014), the measurements of Thoroddsen et al. (2012a), and the measurements presented here.

In the case of water drops of $D = 3$ mm impacting at $U = 10.79$ m/s on a dry surface, the simulation revealed that at the beginning of splashing $\tau < 0.1$ secondary droplets with sizes between 3.5 and 9.2 μm and 9.2 μm were ejected at a horizontal velocity between 36 and 41 m/s. These values were in agreement with the predictions made in the theory and with the existing experimental data for similar impact conditions. It is important to mention that this is a simple comparison with the experimental results and that the tori for the numerical investigation

do not provide sufficient information to make conclusions about the break-up mechanism. The number of ejected secondary droplets was not well simulated since the resolution of the numerical simulations was insufficient. Nevertheless, the good agreement with the experiments allowed to use the simulations to analyse the details of the flow inside the spreading liquid and the surrounding gas.

3 Drop splashing on dry surfaces

In this chapter, the physical phenomena of a drop impacting on dry smooth surfaces at high velocity are analysed, focusing on the dynamics prior, during, and shortly after the ejection of secondary droplets. The focus was to provide detailed experimental data and numerical simulations that help to develop a theoretical model for describing the entire outcome of splashing. This chapter is structured according to the evolvement of drop dynamics over time, starting with the gas entrapment mechanism, following with the ejection of secondary droplets and ending with the spreading dynamics until the maximal spreading diameter is reached, as illustrated in figure 3.1.

Part of the theoretical and experimental studies presented in this chapter have been taken with slight adaptations from previous publications presented in Burzynski and Bansmer (2018b, 2019a,c), Burzynski et al. (2020), Pierzyna et al. (2021). Section 3.3.2 includes text from Burzynski et al. (2020) preparated in cooperation with Professor Dr. Ilia V. Roisman from the TU Darmstadt. The numerical data has been presented in Burzynski and Bansmer (2019b) and is elaborated to some extent in this thesis.

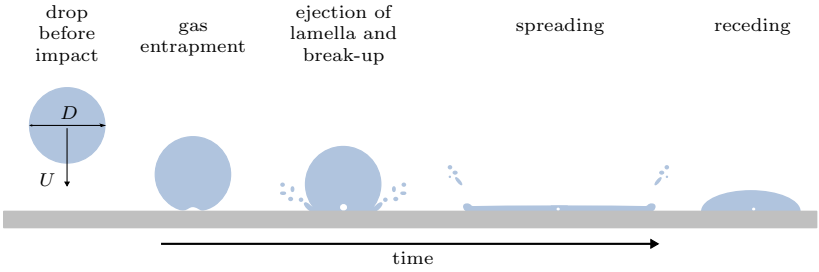

Figure 3.1: Illustration of drop splashing on a dry smooth surface.

3.1 Time evolution of an impacting drop

The drop impact on dry smooth surfaces can be described in four fundamental phases depending on the elapsed time: (1) Drop deformation and gas entrapment before contact with the surface, (2) ejection of a thin lamella with possible break-up into small secondary droplets,(3) spreading at the surface until a maximum diameter is reached, and (4) receding of the deposited liquid until it breaks up again, slowly wets the surface, or stays in equilibrium depending on the surface properties. Figure 3.1 illustrates these drop dynamics, which govern the impact at low and high velocity. One particular characteristic of the drop impact on dry surfaces is that the dynamics can be influenced by the surface properties, for example, roughness (Roisman et al., 2015), porosity (Sahu et al., 2012), wettability (Quetzeri-Santiago et al., 2019), temperature (Liang and Mudawar, 2017), and stiffness (Howland et al., 2016). However, this thesis concentrates on the splashing phenomena on smooth surfaces and the related physics shortly before and after the ejection of secondary droplets; therefore, the reader is referred to (Yarin et al., 2017) to obtain a comprehensive review of the drop impact on surfaces with complex morphology.

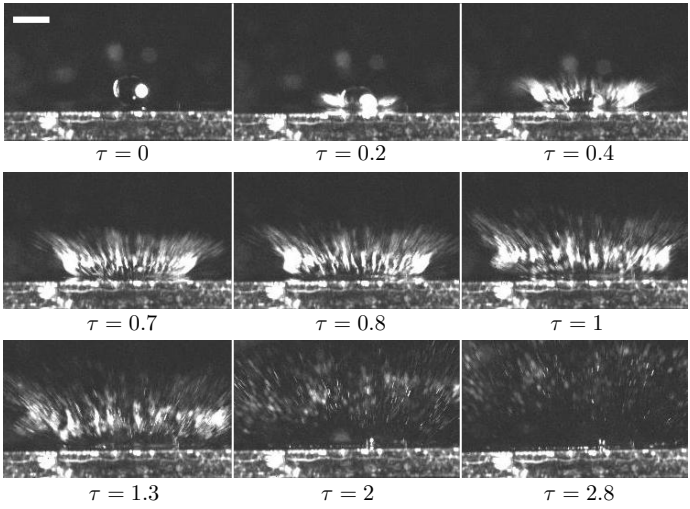

Figure 3.2: Time evolution of a water drop impacting on a smooth dry surface at $We = 3,500$. The impact is recorded at $32,000$ fps with a scale bar of 3 mm. Adapter from Burzynski and Bansmer (2018b).

The sequence of images from figure 3.2 demonstrate the complex splashing phenomena on a dry smooth surface. It can be clearly observed that the splashing of drops generates a large number of secondary droplets in the early stage of impact. On the first impression, it looks like the impact of water drops generates a crown-like liquid sheet in the azimuthal direction, which is known as the corona splash. However, it is demonstrated later in section 3.3.2 that such impact conditions generate a lot of small droplets next to each other or even jets directly from the spreading liquid at the surface, but never a fully developed and levitated corona. The wrong impression in figure 3.2 is caused by the low spatial resolution of the high-speed camera; therefore, it is not accurate to use such resolutions to determine the type of impact outcome.

3.2 Gas entrapment at the early stage of impact

Part of the text described in this section has already been published in Burzynski and Bansmer (2019c).

Technological advances in cameras have increased their temporal and spatial resolution, thus allowing to capture the very fast dynamics occurring at the early stages of impact.(Thoroddsen et al., 2008). These advances allow many authors demonstrate that a drop never impacts the surface in a spherical form; instead, the drops slightly deform just before the contact with the surface due to an increase of gas pressure beneath the drop, as illustrated in figure 3.3. This deformation results in the entrapment of a small amount of gas in the form of a bubble, as shown by the experimental study of Chandra and Avedisian (1991); however, the authors did not provide a physical explanation of the gas entrapment phenomenon. Thoroddsen et al. (2003) for the first time showed the time evolution of the gas entrapment process and the consequent

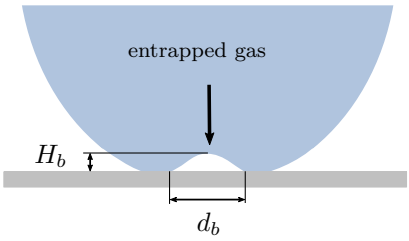

Figure 3.3: Gas entrapment at the moment of contact with the surface and the corresponding dimensions of the formed dimple.

drop contact with the surface along a ring. The dynamics of this gas entrapment can be described by the lubrication theory in the gas neglecting any compressibility effect (Smith et al., 2003); however, for high-velocity impacts, the gas compression cannot be neglected (Mandre et al., 2009). According to the theory proposed by Mandre et al. (2009), the distance between the droplet bottom and the surface at which the droplet starts to deform is defined as

$$H_b = 1.6\epsilon^{1/3} DSt^{*2/3}, \tag{3.1}$$

where $\epsilon = p_{atm}(DU^7\rho_l^4/(2\mu_g))^{-1/3}$ is the compressibility factor, and the inverse Stokes number is defined as $St^* = 2\mu_g/(\rho_l UD)$. These expressions are used to calculate the deformation height for different impact conditions investigated in this thesis.

To analyze how the gas entrapment mechanism affects the splashing of high-speed drops, a tilted high-resolution camera (see section 2.2) was used to capture the spreading of the liquid at the last stages of the spreading phase when the liquid film thickness is very small. At this moment, the footprints of the gas entrapment mechanism can be clearly observed, as shown in figure 3.4. The experiments were conducted by changing the surrounding gas mixture (see table 2.2) while the kinematic impact conditions were kept constant, i.e., water drops of $D = 3.7 \pm 0.2$ mm impacted the glass surface at a constant velocity of $U = 10 \pm 0.5$ m/s. All the experiments where splash could be observed were characterized by the ejection of multiple droplets from the spreading rim located at the surface, also known as the prompt splash.

The deformation height H_b from equation 3.1 revealed a variation between $100 < H_b < 150$ nm for the gas mixtures used. One interesting observation is that in the experiments conducted with low-density gas He(95%) the predicted height $H_b \approx 140$ nm was smaller than the mean free path of gas molecules $\lambda_g = 173$ nm, which implies that the continuum equations without slip correction are not able to properly describe the gas between the droplet and the surface. Hence, either lubrication theory with slip models or kinetic gas theory must be applied instead (Shen et al., 2007). The model of Mandre et al. (2009) suggests that at $H_b \leq \lambda_g$ the deformation of the droplet starts in a region where the probability to find gas molecules is very low (or zero); therefore, gas entrapment should not be expected. Despite this, the experiments revealed that a small amount of gas is always entrapped. Mandre and Brenner (2012) later suggested on the basis of their numerical simulations at reduced pressure that in this particular case the gas beneath the droplet is compressed rather than drained out, which

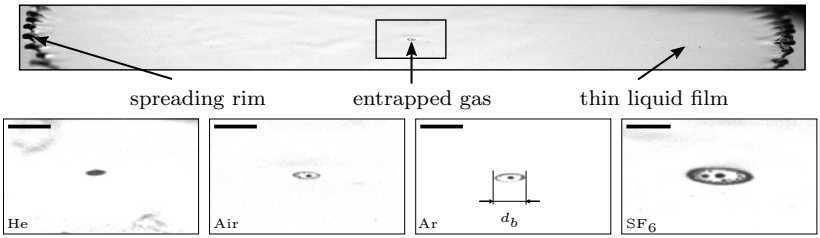

Figure 3.4: Footprints of the gas entrapment mechanism. The top image shows the impact at the latest stages of the spreading phase and the entrapped gas in a box. The boxes highlight the different morphologies that were observed by changing the gases used. Scale bars 500 μm. Adapted from Burzynski and Bansmer (2019c).

again leads to entrapment. The numerical simulations for high-speed impacts conducted for the case of air as a surrounding gas show that the drop is deformed at the height of ≈ 5 μm, which is in agreement with the measurements of Li and Thoroddsen (2015). The gas exits the area beneath the drop just before an amount of gas is entrapped at a very high velocity $> 13U$ as a result of the compression, as shown in figure 3.5. The velocity of the gas in the neck region decreases after the lamella becomes larger than the diameter of the drop.

Different morphologies of the gas entrapment mechanism can be obtained depending on the gas used, as demonstrated in figure 3.4. Although the most common morphology observed during the experiments was a ring of microbubbles with single or multiple larger bubbles in the center (Thoroddsen et al., 2005), a single bubble was observed only when using helium. Li et al. (2017) demonstrated that for cases where gas compressibility plays an important role ($\epsilon^{-}1 \gg 1$), the gas can be entrapped by a double contact, forming a torus of gas. It is possible that this torus cannot be preserved until the final stages of the spreading phase; therefore, the experimental method presented here could not capture the footprints of this phenomenon. An increase in gas density resulted in more bubbles in the center and thicker rings. During the experiments with SF_6(39%), the primary droplet slightly deformed to an oblate before the impact. Keep in mind that the pure gas concentration compared to the air is given in parentheses after the name of each gas, as explained in section 2.1.2. This was caused by the high stagnation pressure at the impact surface, which was generated by the flywheel rotation.

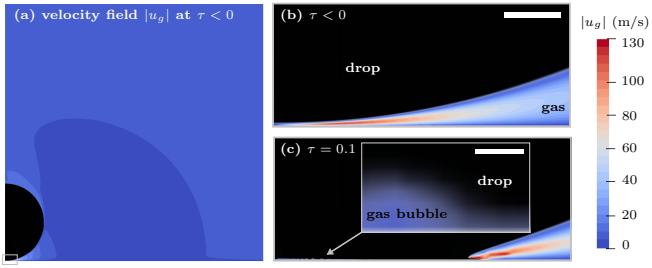

Figure 3.5: Simulated velocity magnitude field during the early stage of impact for a drop of $D = 3$ mm impacting at $U = 10.79$ m/s. (a) shows the velocity field of the entire domain during the drop deformation. (b) shows the gas exit velocity during drop deformation; scale bar 1 mm (c) shows the fast-moving gas and the entrapped small bubbles; scale bar 20 μm.

3.2.1 Size of the entrapped ring

Part of the text described in this section has already been published in Burzynski and Bansmer (2019c).

The diameter of the ring of microbubbles d_b was measured to quantify the entrapped gas bubble and compare the results with the existing theories (Hicks and Purvis, 2010, Mandre et al., 2009). This diameter determines the position of the droplet and substrate contact Thoraval et al. (2013), Thoroddsen et al. (2005). Although it has been suggested that either the density Guo et al. (2016) or the viscosity Jian et al. (2018) dominate the early stage of splashing, it was found that the gas bubble diameter is strongly influenced by both ρ_g and μ_g. To elucidate how each gas property affected the entrapment size, the following two cases are examined. In the first case, two gases with the same viscosity but significantly different densities were compared, $\Delta\rho_g \approx 83\%$ (He(95%) and O_2(95%)), and the measurements demonstrated that the diameter d_b varied by approximately 30%. In the second case, when selecting another two gases with similar densities but different viscosities $\Delta\mu_g \approx 30\%$ (CO_2(74%) and Ar(79%)), d_b varied by about 14%. These comparisons clearly show that both properties can influence the early stage of impact.

Regarding the role of compressibility, the model of Mandre et al. (2009) predicts that the gas bubble diameter becomes smaller when ϵ^{-1} increases, but the experiments conducted at high impact velocity

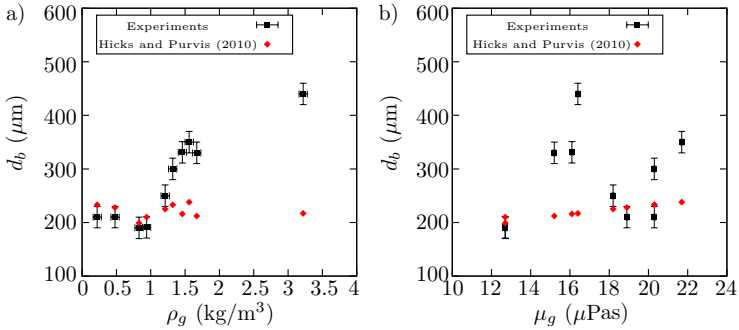

Figure 3.6: Diameter of the ring of microbubbles d_b as a function of the gas density and viscosity at normal atmospheric pressure. The diameter and velocity of the water drops were kept constant as $D = 3.7 \pm 0.3$ mm and $U = 10 \pm 0.1$ m/s, respectively. Adapted from Burzynski and Bansmer (2019c).

demonstrated the opposite. For example, it was found during the experimental work conducted for this thesis that a diameter of 210 μm was formed in the case of He(95%, $\epsilon^{-1} = 89$), while in the case of CO_2(74%, $\epsilon^{-1} = 98$) the diameter was 330 μm. The reason for this difference probably lies in the theoretical approach of their model, which assumes either an isothermal or adiabatic gas state. Hicks and Purvis (2013) have shown with a full analysis of the gas, including energy conservation equations, that the gas bubble diameter is independent of the compressibility. This independency is the result of the interaction between the gas density, temperature, and interface, which leads to a greater lateral spreading of the gas than that predicted by Mandre et al. (2009); therefore, the decrease in size is compensated due to energy conservation. Since the gas bubble diameter is independent of the compressibility, it can be predicted using the incompressible theory of Hicks and Purvis (2010). The expression for this diameter reads as follows:

$$d_b = C_0 \left(\frac{4\mu_g}{\rho_l U} \right)^{1/3} (D/2)^{2/3}, \tag{3.2}$$

with $C_0 = 3.8$ as calculated in Hicks and Purvis (2013). This formula agrees with the experimental data obtained by Li and Thoroddsen (2015), where they investigated the droplet impact using only air as the surrounding gas. As shown in figure 3.6(a), the model of Hicks and Purvis predicts the diameter of the ring of microbubbles d_b en-

trapped at the early stages of splashing accurately only for the high-speed impact of drops when the surrounding gas density is relatively low ($\rho_g < 1.2$ kg/m^3). By increasing the gas density, this model predicts almost the same diameter, while the measurements clearly demonstrated an increase. This discrepancy can be attributed to the absence of gas density in the expression 3.2, which increases in relation to ρ_g. The slight deformation of the primary droplet observed during experiments with SF_6 probably led to more entrapment than expected for a perfectly spherical droplet Li and Thoroddsen (2015). Considering this effect in equation 3.2, the model predicts a diameter of ≈ 250 μm; consequently, the droplet deformation caused by the substrate movement is insufficient to explain the observed discrepancy.

By analyzing the numerical simulations for high-speed drops, it can be observed that the generation of multiple small bubbles is resolved to some extent. The result of the simulations is more or less comparable with the images obtained within the experiments (see figure 3.4). As mentioned at the beginning of this section, the experimental data revealed that the ring of microbubbles can grow up to a diameter of ≈ 180 μm, while the numerical simulation predicts that the ring of microbubbles elongates at later stages of impact ($\tau > 1$) up to ≈ 300 μm. However, it is challenging to define the exact diameter of the ring in the simulations since the VOF method does not capture a sharp interface. The zoomed area in figure 3.5(c) shows this diffuse interface, where a small gas bubble is formed. As can be seen in this image, it is not possible to define the boundary of the gas bubble since it is not clear where the bubble ends. This fact makes a precise definition of the size of the microbubbles entrapped very challenging. Nevertheless, the results are relative close to those predicted by the theory and observed in the experiments.

Although a small amount of gas was entrapped in the experiments regardless of the gas used, a water drop impacting at such high velocity does not necessarily splash. This was shown in the experiments using helium or NH3(77%) and is analyzed in detail in the next section 3.3, where the mechanism of splashing is theoretically, numerically, and experimentally investigated. The results demonstrate that droplet deformation at the early stage of impact and the subsequent gas entrapment is not the mechanism responsible for splashing. In cases where low-density gases (without splashing) were used, the gas beneath the droplet was compressed rather than drained out, which again led to the entrapment of gas.

The experiments and numerical simulations conducted using different gases demonstrate that the gas entrapment is not the mechanism responsible for splashing.

3.3 Mechanisms of splash

Part of the text described in this section has already been published in Burzynski and Bansmer (2019c) and Burzynski et al. (2020).

One of the first studies on drop impacts providing a model that identifies when splashing occurs was presented by Mundo et al. (1995). They developed a theory stating that splashing occurs when the kinetic and surface energy of the drop before the impact is larger than the dissipated energy when the drop spreads. This theory is supported by multiple measurements of the size and velocity of these secondary droplets. The extensive work of the authors resulted in the proposition of a composited parameter to distinguish between the deposition and splashing based only on the Reynolds and Weber numbers. This composited parameter can be written as:

$$K = OhRe^{1.25} = We^{1/2}Re^{1/4}, \tag{3.3}$$

where $Oh = \sqrt{We}/Re$ is the Ohnesorge number. This K-Parameter is widely used in engineering applications and has been adapted over the years to provide a splashing threshold depending on different impact conditions (Moreira et al., 2010). However, the splashing of liquid drops on dry surfaces is a phenomenon that also depends on the surface properties, such as roughness, porosity, wettability, etc. (Yarin et al., 2017). Hence, a prediction of splashing using this K-Parameter is inappropriate.

The experiments of Xu et al. (2005) demonstrated that splashing is additionally influenced by ambient gas properties and can be suppressed by reducing air pressure. The emergence of a corona during splashing is explained by the authors as a weak shock in the air, which destabilizes the liquid film and bends it upwards. Xu et al. (2005) concluded that the stress on the expanding lamella destabilizes the liquid and leads to its break-up. The stress in their theory is estimated as:

$$\Sigma = \frac{\rho_g We}{2Ma\rho_l\sqrt{Re}} \tag{3.4}$$

with $Ma = U/c_g$ as the Mach number and c_g the speed of sound in the gas. When $\Sigma > 0.45$, a splash is expected. The remarkable experiments of Xu et al. (2005) motivated a large number of theoretical, numerical, and experimental investigations over the last 15 years and reinforced the fact that the use of the K-Parameter is not suitable to predict the splashing of drops on dry surfaces (Pierzyna et al., 2021).

In a more detailed theoretical investigation, Riboux and Gordillo (2014) considered an inviscid and incompressible flow and concluded that splashing is attributed to a lift force F_L experienced by the spreading lamella (hereafter RG theory). Their theoretical analysis shows that this lift force results from the lubrication force induced by the gas beneath the lamella and the suction force induced at the top of it. An example of this acting force is shown in figure 3.7.

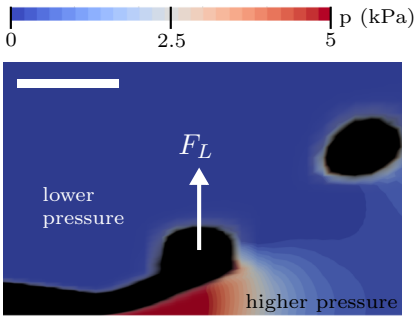

Figure 3.7: Lift force (suction and lubrication forces) acting on the spreading lamella during splashing. Scale bar 10 μm.

The lift force exerts a vertical velocity to the spreading lamella, and if this velocity is larger than the retraction velocity due to capillarity, the atomization process starts. Riboux and Gordillo (2014) proposed a splashing parameter, which is defined as:

$$\beta = \sqrt{F_L/(2\sigma)}. \tag{3.5}$$

If this ratio is larger than 0.14, splashing occurs. The agreement of this theory with multiple experiments has led to recent modifications that consider the drop impact on heated, moving, inclined or hydrophobic surfaces (Gordillo and Riboux, 2019, Hao and Green, 2017, Quintero et al., 2019, Staat et al., 2015).

To investigate the transition between deposition and splash in this work, multiple experiments were performed at high velocity using different gases. As mentioned before in section 3.2, such experiments were conducted with water drops of $D \approx 3.7 \pm 0.2$ mm impacting at a constant velocity of $U \approx 10 \pm 0.5$ m/s. The results indicate that splashing can be suppressed when using helium or $NH_3(77\%)$ even at such high impact velocities and normal ambient pressure. The prediction of this behavior using the widely popular K parameter was not possible due to the fact that equation 3.3 does not depend on the gas properties. The

stress analysis from equation 3.4 indicated that only deposition was to be expected in the case of He(95%), which was in agreement with the observations. By increasing the density of the gas, it was possible to come closer to the splashing threshold, as in the case of NH_3(77%), where the ejection of secondary droplets was detected in some images. Using this particular gas mixture (NH_3(77%)), a stress of $\Sigma = 0.46$ was estimated, which is very near to the splashing threshold of $\Sigma = 0.45$. This again is in agreement with the observations. On the contrary, stress of $\Sigma = 0.61$ was estimated for He(70%), clearly suggesting a splash. However, the measurements showed that the transition from deposition to prompt splash in this configuration is about to happen, since splashing was only observed in some images. This fact suggests that the stress theory proposed by Xu et al. (2005) does not predict with accuracy the splashing threshold for high-speed impacts.

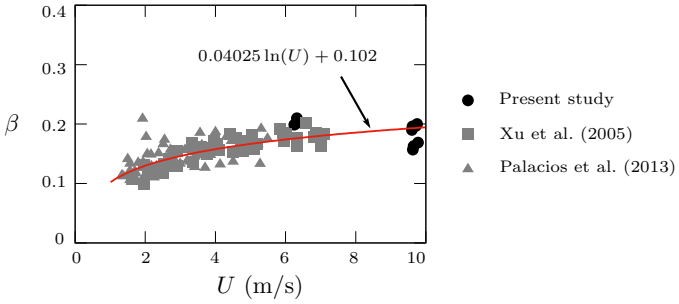

Figure 3.8: Splashing threshold as a function of the impact velocity. The diagram shows that β is not constant and increases with U.

The splashing parameter β from the RG theory predicts only the absence of splashing for the experiments shown here using He(95%). This model also indicates that the cases with He(70%) and NH_3(77%) are very close to the splashing threshold of $\beta = 0.16$ and 0.19, respectively. All the experiments conducted near to this transition point indicated that splashing in high-speed impacts occurs when $\beta > 0.19$ instead of 0.14. This was confirmed by the experiments performed using acetone drops of $D \approx 2.5$ mm impacting at $U \approx 6.3$ m/s, where a very small amount of ejected droplets was observed but could not be detected by the post-processing software. The splashing threshold of 0.14 results from analyzing multiple experiments with a wide range of viscosities, surface tensions, and surface wettabilities at low impact velocities (Ri-

boux and Gordillo, 2014). However, the analysis of the results obtained by Xu et al. (2005) and Palacios et al. (2013) shows that the splashing threshold tends to increase with the impact velocity, as shown in figure 3.8. Using machine learning algorithms Pierzyna et al. (2021) developed a data-driven splashing threshold model and demonstrated that not only the impact velocity affects the splashing threshold but also the liquid viscosity, surface tension, and gas density. Nevertheless, the RG theory describes very well the boundary between the deposition and splashing when drops impact at low or high impact velocities, regardless of the surface properties (Gordillo and Riboux, 2019, Hao and Green, 2017, Staat et al., 2015)

All the studies published indicate that splashing on dry smooth surfaces can be attributed to an aerodynamic lift force, as proposed by Riboux and Gordillo (2014).

3.3.1 Typical outcomes of high-speed drop impact

Part of the text described in this section has already been published in Burzynski et al. (2020).

The drop splashing on dry surfaces can be subdivided into three distinct regimes: the corona splash, the prompt splash, and the receding break-up (Rioboo et al., 2001). However, when the drop impacts at high velocity on a smooth surface, the only two possible outcome are either the corona or prompt splash, as shown in figure 3.9. The corona splash is formed from the liquid of the primary drop if the aerodynamic lift force is high enough to levitate the outer part of the spreading lamella. The prompt splash is characterized by the emergence of multiple jets without corona formation and has been typically attributed to drop impact on rough or structured surfaces (Aboud and Kietzig, 2015, Marengo et al., 2011, Roisman et al., 2015). In such cases, the surface morphology affects the flow of the spreading lamella, contributing to the ejection of jets (Yarin et al., 2017). However, the attribution of the prompt splash exclusively to the surface morphology seems to be incomplete because this splashing regime can be observed on smooth surfaces at higher Reynolds numbers. The sequence of images from figure 3.9 show the major differences between the corona and prompt splash regimes over time. While the levitated lamella remains visible in the corona splash regime almost during the entire splashing time

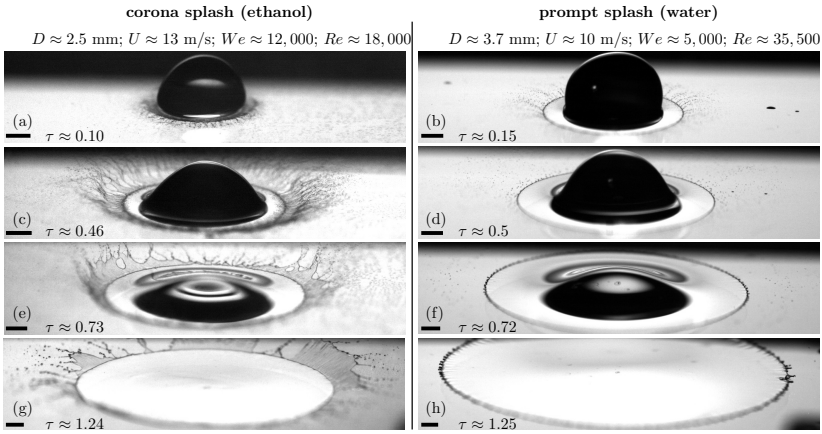

Figure 3.9: Reconstruction of the evolution of splashing. The images demonstrate the differences between the corona and prompt splash on a dry smooth surface at different impact times. Scale bar 1 mm at the focal plane. Adapted from Burzynski et al. (2020).

$\tau = tU/D$, a free liquid sheet in the azimuthal direction is not formed or visible in the prompt splash regime.

The corona splash formed on dry surfaces differs significantly from the corona observed after drop impact on a liquid film. The key difference is the composition of the corona: during the drop impact on a wetted surface, the corona is formed by the liquid from the surface film and the drop, while the single droplet impact on a dry surface only contains liquid from the drop. The splash of drops on wetted surfaces is the result of rim instability leading to cusp formation and fingering (Yarin et al., 2017). When a drop impacts a smooth dry surface at high velocity, the complex free liquid film becomes unstable. This corona instability creates a wavy structure, which leads to the emergence of the jets at the corona rim. The corona subsequently breaks up at some height above the surface. As the images in figure 3.11(c,f,i) demonstrate, the height of this corona decreases with increasing Reynolds numbers. In the prompt splash regime, the corona does not appear, and the splash occurs as the result of the break-up of single jets emerging from the surface-bound lamella, as shown in figures 3.9 and 3.10. By increasing the impact velocity, the flow of the spreading lamella becomes unstable; instead of droplet formation directly at the rim, large jets are formed with a thin liquid sheet connecting them occasionally

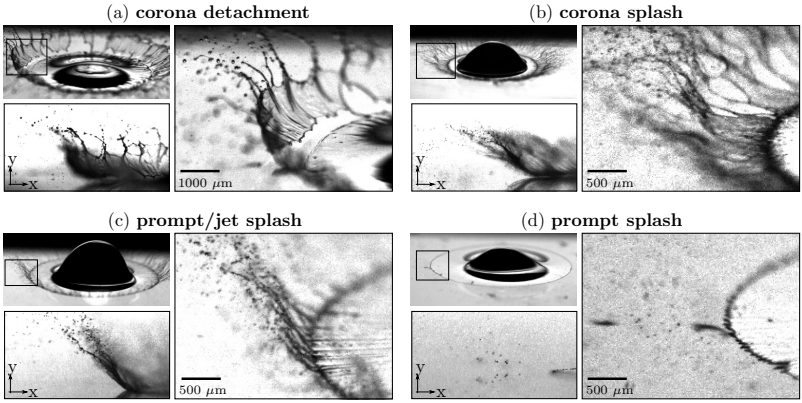

Figure 3.10: Typical break-up regimes at relatively high impact velocities: (a) corona detachment with consequent disintegration of an ethanol drop, $We = 3,300$, $Re = 9,500$; (b) corona splash of an ethanol drop, $We = 6,500$, $Re = 14,000$; (c) limiting case of the prompt splash with relatively short corona and long jets observed with water drop, $We = 10,700$, $Re = 54,400$; (d) the prompt splash of an acetone drop, $We = 7,000$, $Re = 62,000$. Adapted from Burzynski et al. (2020).

in some azimuthal locations. Note that in figure 3.10(c) the side view would suggest the corona splash; however, this is not the case as the tilted view shows. The analysis of multiple images from that perspective shows that those jets can be formed in some cases from a very small and irregular detached lamella, which is ejected at the beginning of splashing. Hence, the distinction between the corona and prompt splash only from a side view perspective is not reliable.

The outcome of high-speed drop impact can be divided into four categories: the corona splash, the corona splash with detachment, the prompt splash, and the prompt/jet splash.

Effect of Reynolds and Weber numbers on splashing

Examples of the effects of the liquid properties and impact velocity on the splashing are shown in figure 3.11. A strong influence of liq-

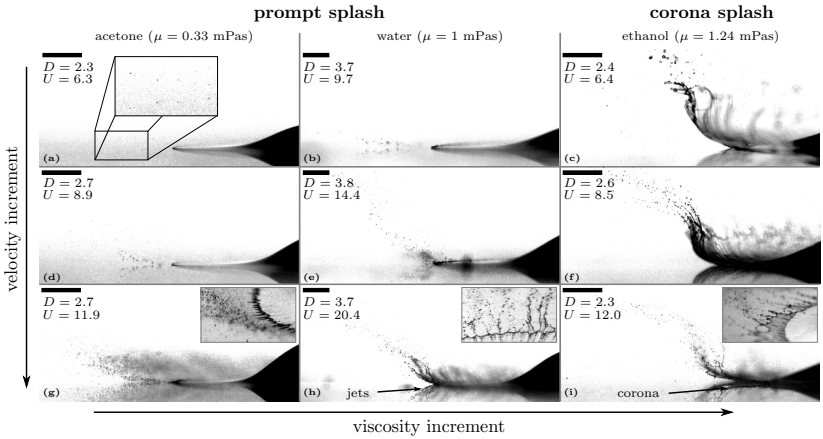

Figure 3.11: Effect of the Weber and Reynolds numbers on splashing. The influence of We is shown when comparing the water and acetone impacts, where We varies but Re is almost constant. The dominant role of Re is revealed by comparing the ethanol and acetone impacts. The impact time is $\tau \approx 0.5$, the diameters are in mm, and velocities in m/s. Scale bars 1 mm. Adapted from Burzynski et al. (2020).

uid viscosity on splashing can be clearly identified from these images by comparing the impact of ethanol drops with that of acetone drops. Here, the density and surface tension of both liquids are nearly identical, but the viscosity of ethanol is more than four times higher than that of acetone. This leads to a change in the Reynolds number of the same magnitude, while the Weber number remains constant; as a result, the increase in viscosity switches the regime from the prompt to corona splash.

One difference between these liquids is that acetone evaporates much faster, which leads to a reduction of the drop diameter over time. By measuring all the drops prior to impact, it is assured that the drops of both liquids analyzed here possess the same diameter; therefore, it was expected that the fast evaporation of acetone would not affect the splashing outcome as the change in viscosity does. Such drastic changes in the splashing regime due to liquid viscosity have also been reported previously by Palacios et al. (2013) and Stevens et al. (2014) but for low-speed impacts and even more viscous drops. The changes in splashing regime at the highest impact velocities are shown in figure 3.11; here, the splashing outcome seems to be identical from a side view. However,

the detailed tilted view demonstrates that the prompt/jet splashing regimes dominate the impact of water drops, while a clear corona is formed in the case of ethanol drops. All these observations underline the fact that the splashing regime strongly depends on the physical properties of the liquids used and not on the impact conditions.

To analyze the effect of surface tension on splashing, experiments were performed with acetone and water drops. The physical properties between these liquids are similar with the exception of the surface tension, which for water is more than three times higher than that of acetone. The use of these liquids allowed to double the Weber number and keep the Reynolds number almost constant $\Delta Re \approx 10\%$. As can be seen from figure 3.11, the splashing from both liquids resulted in the prompt splash. Pasandideh-Fard et al. (1998) and Rioboo et al. (2002) investigated the surface tension effect on the drop impact on smooth surfaces and demonstrated that surface tension has almost no influence at the early stage of impact when the secondary droplets are generated. In the detailed work of Palacios et al. (2013), it has been argued that the surface tension stabilizes the spreading lamella at large Re, while the viscosity only affects its thickness; therefore, the larger the viscosity, the thicker the spreading lamella. This increase in the lamella thickness leads to a drastic change from the prompt to corona splash regime. The observations made by previous authors and the experiments presented here provide evidence that the Reynolds number plays a more important role than the Weber number on the splashing process in high-speed impacts.

3.3.2 Conditions for the prompt splash regime

Part of the text described in this section has already been published in Burzynski et al. (2020).

One possible mechanism leading to the prompt splash is the Rayleigh-Taylor instability of the spreading liquid (Chandrasekhar, 2013). This instability has been speculatively assumed by Li et al. (2018) after examining the structure and wavelengths of the unsteady azimuthal undulations present in the spreading lamella at the early stage of impact. Xu et al. (2005) have shown that aerodynamic effects determine the splashing threshold; however, in section 3.2 of this thesis it is shown that the properties of the surrounding gas do not affect the type of splash regime (Roisman et al., 2015, Stevens et al., 2014).

To estimate the threshold conditions, the perturbation growth ω of the small antisymmetric disturbances of a thin accelerating liquid film

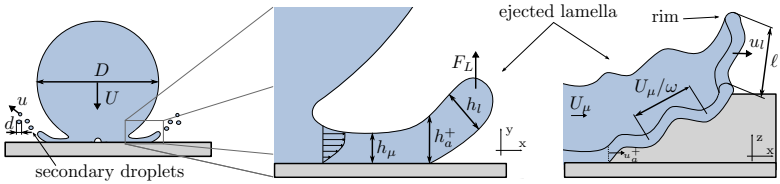

Figure 3.12: Sketch of an impacting drop and its lamella. It shows the splashing mechanism and the most relevant quantities used in the theoretical analysis, such as the lift force acting on the lamella F_L, the break-up length of the corona U_μ/ω, and its corresponding wavelength ℓ. Reprinted from Burzynski et al. (2020).

was calculated from the inviscid solution (Entov et al., 1985, 1986, Yarin, 1993) as

$$\omega = \frac{a_l^{1/2}\zeta^{1/2}}{2h_\mu^{1/2}\tilde{We}^{1/2}}\left[\sqrt{16\tilde{We}^2+\zeta^2\left(\zeta^2-4\right)^2}-\zeta^3-4\zeta\right]^{1/2}, \qquad (3.6)$$

where a_l is the film acceleration in the direction normal to its median surface, h_μ is the film thickness, $\tilde{We}$ is the film Weber number, and ζ is the dimensionless wave number. The film Weber number is defined as $\tilde{We} = \rho_l h_\mu^2 a_l/\sigma$, where $h_\mu \sim DRe^{-1/2}$ is the scale for the lamella thickness (Lagubeau et al., 2012, Roisman et al., 2006) and $a_l \sim U^2/D$ is the scale for the film acceleration (de Ruiter et al., 2010). The Reynolds number of the film is analogously defined as $\tilde{Re} = \rho_l h_\mu^{3/2} a_l^{1/2}/\mu_l$. The value of the film Reynolds numbers $\tilde{Re}$ is $O(10^1)$, while the value of the film Weber numbers $\tilde{We}$ is $O(10^{-2})$. These estimations suggest that the influence of surface tension in the film is more significant than the influence of viscosity. Figure 3.12 illustrates the main variables used in this section to describe the mechanism of drop splashing and the ejection of secondary droplets.

The linear relation of the film thickness and the scale h_μ was first assumed by Yarin and Weiss (1995) and then experimentally confirmed by de Ruiter et al. (2010). Roisman et al. (2006) roughly estimated the thickness of the lamella at the dimensionless time $\tau = 1$ from the mass balance using experimental data for the spreading diameter (Fukai et al., 1995, Roisman et al., 2002a,b). As a result, they have shown that the thickness of the lamella scales well as $h_\mu \sim DRe^{-1/2}$ in the range $500 < Re < 5000$. Bird et al. (2009) studied the drop impact on moving

surfaces and successfully used the scale $h_\mu \sim DRe^{-2/5}$ for modelling the splashing threshold. The same scale for the residual film thickness has been analytically obtained by Roisman (2009) from the exact solution for the flow in the lamella. The numerical and experimental study of Visser et al. (2012) on the dynamics of high-speed micro-drop impact corroborates that the thickness of the spreading lamella for the normal impact of drops on dry surfaces can be scaled as $h_\mu = DRe^{-1/2}$.

Approximation using the impact parameters

The estimation of the rate of growth of the fastest unstable mode in the spreading film is made from equation (3.6) for very small values of the Weber number of the film. A simplification can be obtained using this equation and the related most unstable dimensionless wave number $\zeta \approx \tilde{We}^{2/3}/\sqrt{2}$, which reads as $\omega \approx (a_l \tilde{We}/2h_\mu)^{1/2}$. It should be noted that the Weber number of the film associated with the prompt splash for the experiments presented here and all the experiments found in the literature are $\tilde{We} < 0.1$. Furthermore, the corresponding wavelength of the most unstable mode is expressed as $\ell \approx 2\sqrt{2}\pi h_\mu \tilde{We}^{-2/3}$. These expressions can be rewritten using the terms based on the drop impact parameters as

$$\omega \approx \frac{UWe^{1/2}}{\sqrt{2}DRe^{1/4}}, \quad \ell \approx 2\sqrt{2}\pi D \frac{Re^{1/6}}{We^{2/3}}. \tag{3.7}$$

The break-up length of the corona due to the Rayleigh-Taylor instability can be estimated as U_μ/ω (Huang, 1970), where U_μ is the typical velocity of the liquid in the lamella. This estimation of the break-up length results from the analysis of the linear wave motion of a thin liquid sheet, neglecting the internal flow motion. The velocity of the lamella is influenced by its thickness, which can be roughly estimated from the mass balance equation, resulting in $U_\mu^2 \sim DU^2/h_\mu$. The break-up length determines two important parameters: the height at which the corona starts to disintegrate and the number of uprising jets. In this work, the prompt splash is defined as a situation where the break-up length is comparable to the thickness of the lamella and multiple jets are formed in the azimuthal direction. The first necessary condition for prompt splash is therefore $U_\mu/\omega < h_\mu$, which can be rewritten with the help of equation (3.7) in the following form:

$$We^{1/2} \leq Oh^\star Re, \tag{3.8}$$

where $Oh^\star$ is the threshold Ohnesorge number.

The second necessary condition for the prompt splash is the development of multiple jets close to each other in the azimuthal direction. This implies that the wavelength of the most unstable mode must be much smaller than the drop diameter; otherwise, this length ℓ, as illustrated in figure 3.12, would only lead to a very small or non-existent number of jets at the early stage of impact. Thus, the second condition for the prompt splash can be defined with the help of the expression for wavelength ℓ from equation (3.7) yielding

$$We \geq Z^{\star} Re^{1/4}, \tag{3.9}$$

where $Z^{\star}$ is a dimensionless empirical constant. These two equations represent the boundaries within which the prompt splash for high-speed impacts is expected. Outside these thresholds, another regime such as the corona splash, the deposition, or the receding break-up can result from the impact on a dry smooth solid surface.

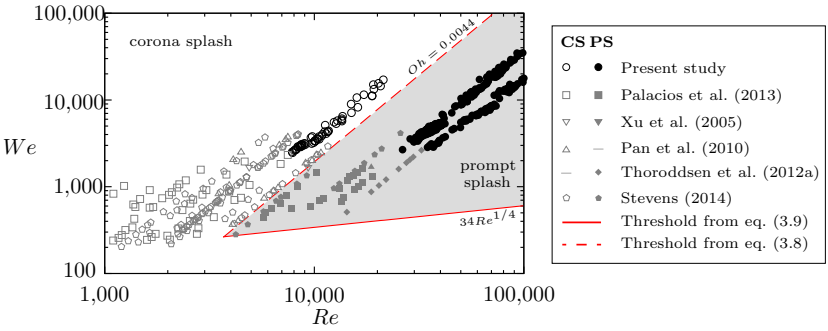

Figure 3.13: Impact conditions for the prompt (PS) and corona (CS) splash obtained from different liquids, drop sizes, and impact velocities. The grey area represents the zone where the prompt splash is expected. This area is defined by the conditions calculated from equations (3.8) and (3.9). Reprinted from Burzynski et al. (2020).

The validation of this analysis is made considering the presented experimental data, the numerical simulations, and the existing experiments for drops impacting a dry smooth surface at relatively high impact velocities. The different outcomes from those experiments are shown in figure 3.13 as a function of the Weber and Reynolds numbers. The threshold $Oh^{\star}$ in the form obtained in equation (3.8) successfully predicts the boundary between the prompt and corona splash; this

prediction is validated using the available experimental data from low-speed impacts and the measurements from this thesis at much higher values of the Weber and Reynolds numbers. Palacios et al. (2013) empirically obtained this threshold for the prompt splash at $Oh^\star = 0.0044$, which has been confirmed by Roisman et al. (2015).

The threshold $Z^\star$ as predicted in equation (3.9) sets the boundary between the prompt splash and the deposition or receding break-up. The definition of a value for this threshold is challenging because, as it was argued in section 3.1, the prompt splash generates small droplets, which can be hardly recognized by set-ups with insufficient spatial resolution. Therefore, many authors may have erroneously claimed deposition when actually prompt splash occurs. Figure 3.11(a) illustrates this challenging detection, even with a spatial resolution of 5 μm/px. Nevertheless, all the observed cases of prompt splash belong to the range of parameters satisfying the condition (3.9) with $Z^\star = 34$. The derived threshold conditions determine very well the boundaries defining the region of the prompt splash on a smooth dry surface, as shown in figure 3.13. This result indicates that the Rayleigh-Taylor instability could indeed be the main mechanism leading to the prompt splash.

> The prompt splash is defined as a situation where the break-up length is comparable to the thickness of the lamella and multiple jets are formed in the azimuthal direction. The main mechanism causing the atomization in this splashing regime is the Rayleigh-Taylor instability.

3.4 The outcome of drop splashing

Part of the text described in this section has already been published in Burzynski and Bansmer (2019c) and Burzynski et al. (2020).

The high-speed impact of drops on a dry smooth surface generates a spray of secondary droplets upon the surface, as shown in figure 3.14. The ejection of these small secondary droplets is a continuous process, starting shortly after the liquid lamella is detached from the surface at the early stage of impact. The characterization of these secondary droplets can be extremely challenging and at the same time fundamental for a wide range of technical applications such as aircraft icing, vehicle soiling, and ink-jet printing. Despite the technical importance, almost nothing is known about these small droplets.

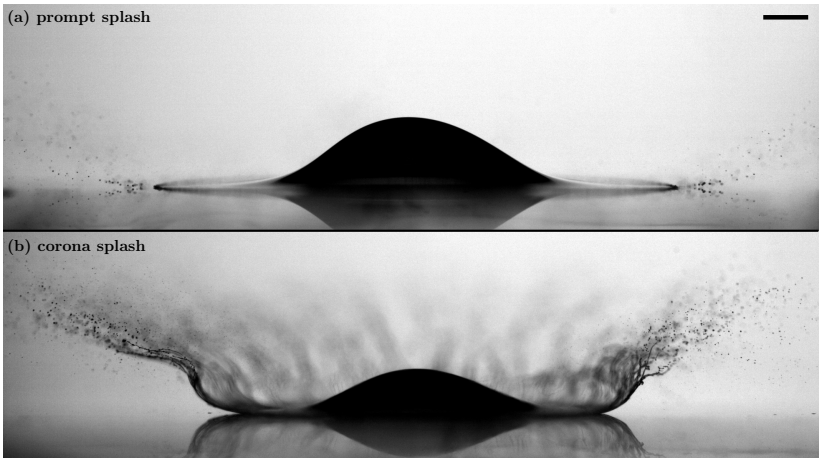

Figure 3.14: Drop splashing at high-speed on smooth dry surfaces. (a) shows the impact of a water drop at $We \approx 5,000$. (b) shows the impact of an ethanol drop at the same Weber number. Scale bar 500 μm. Adapted from Burzynski et al. (2020)

One of the first experiments conducted to characterize the secondary droplets was presented by Stow and Stainer (1977). They demonstrated that kinetic energy, surface tension, and surface properties affect the size and amount of the ejected droplets. Decades later, Mundo et al. (1995) provided more detailed measurements of the size and velocity of these secondary droplets and proposed the well-known splashing parameter K, as described in section 3.3. Xu et al. (2007) measured droplets larger than $d > 100$ μm after they impacted on a surrounding paper sheet and showed that air pressure in combination with surface roughness can alter the outcome of splashing. The experiments of Thoroddsen et al. (2012a) revealed a size range from $d \sim 5$ to ~ 60 μm for prompt splash on smooth surfaces. Faßmann (2015), Faßmann et al. (2013) made use of shadowgraph techniques and captured droplets larger than 30 μm, providing more resolved size and velocity distributions than previously available. They demonstrated than the arithmetic mean diameter decreases with increasing impact velocity, while the droplet velocities increase.

Many other studies have been carried out in order to quantify the position, size, and velocity of the smallest droplets ejected after the impact close to dry edges or on small targets (Lejeune and Gilet, 2019,

Villermaux and Bossa, 2011, Wang and Bourouiba, 2018). In those cases, the secondary droplets are generated from a free expanding sheet, which emerges in the later stages of splashing beyond the surface border. Since there is no surface, almost the entire free lamella atomizes, generating a larger amount of droplets (Chen et al., 2019). Therefore, the impact close to the edges or on small targets completely differs from the impact on a larger target (Rozhkov et al., 2002); for this reason, it is expected that the size, velocity, and volume of the ejected droplets diverge from those presented in this thesis. Similarly, the splash generated after the impact on a liquid film cannot be associated with the impact on a dry surface because the corona is formed by the liquid from the surface film and the drop, while the single droplet impact on a dry surface only contains liquid from the drop.

3.4.1 Size of the secondary droplets

Part of the text described in this section has already been published in Burzynski and Bansmer (2019c) and Burzynski et al. (2020).

The splash generated by the high-speed drops produces a host of secondary droplets either from the levitated lamella (corona splash) or directly from the rim (prompt splash). Since the origin of these droplets in both regimes is the spreading lamella, it is reasonable to expect that

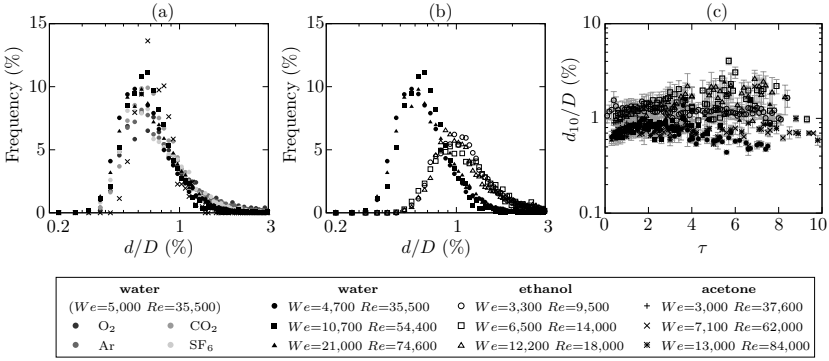

Figure 3.15: The size of the secondary droplets. (a) shows the size distribution in the prompt splash regime. (b) demonstrates the major differences between the corona and prompt splash regimes. (c) shows the time evolution of the arithmetic mean diameter over time. Reprinted from Burzynski et al. (2020)

the diameter of the droplets correlates with the lamella thickness. This thickness changes over time (de Ruiter et al., 2010), suggesting that droplets of different sizes should be generated during splashing. This is demonstrated in figure 3.15(a-b), where the droplet size distributions for the prompt and corona splash are plotted. The measurements indicate that the normalized size distributions for high-speed drop impacts are in a specific splashing regime almost independent of the kinematic conditions before impact; however, there is a notable difference between the prompt and corona splash regimes. This difference is attributed to the larger size of ejected droplets due to the break-up of the levitated lamella, which never develops in the prompt splash.

Regarding the role of the surrounding gas on the size of the ejected droplets, figure 3.16 clearly demonstrates that the size distribution is independent of the gas, even though the number of droplets detected increases with the gas density. Similarly to this observation, Latka et al. (2012) reported the ejection of more droplets with increased pressure, which is then proportional to the gas density. By analyzing the gas Weber number on the basis of the spreading lamella, which in the case of small thickness and low gas density is very small, it becomes clear that small perturbations of the gas velocity field do not influence the instability of the lamella. Therefore, the characteristic droplet size is determined exclusively by the liquid properties. All the conducted experiments revealed that the droplets expelled in the prompt splash regime are very small and rarely larger than 2% of the primary drop diameter. These results agree well with the measurements of Thoroddsen et al. (2012a) at the early stage of impact, where the authors observed instabilities in the cusp and related them to the prompt splash. On the contrary, the corona splash ejected larger droplets ranging between 0.6% to 3% of D. This difference between the splashing regimes is explained due to the formation of a large corona, which generates a large number of droplets with a significantly larger diameter.

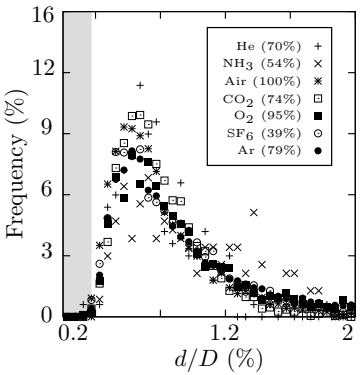

Figure 3.16: Effect of the surrounding gas on droplet size. Adapted from Burzynski and Bansmer (2019c).

Mean diameter over time

To elucidate the transient splashing phenomena (see figure 3.9), the time evolution of the dimensionless arithmetic mean diameter d_{10}/D is plotted in figure 3.15(c). The measurements demonstrate that d_{10} increases with τ at the early stage of impact for the corona and prompt splash regimes, which leads to a wide range of sizes of the ejected droplets. This is caused primarily by viscous effects on the spreading lamella, which lead to its deceleration and subsequently to an increase in the rim thickness (de Ruiter et al., 2010, Riboux and Gordillo, 2017, Thoroddsen et al., 2012a).

After this initial phase and between the impact times $1 < \tau < 3$, d_{10} stabilizes into a relatively constant value. Later on, the arithmetic mean diameter decreases in the case of the prompt splash for the lowest impact velocities. On the contrary, d_{10} increases for the higher impact velocities due to the break-up of the larger jets, which generate much larger droplets. The arithmetic mean diameter of the secondary droplets for the corona splash is always larger than the prompt splash due to the formation and break-up of the corona. The corona break-up occurs in the later stages of impact, as can be seen in figure 3.15(c).

The mean secondary droplet diameter scaled by h_μ is plotted in figure 3.17 as a function of the Reynolds number. The diagram shows that the scaled droplet diameter stays relatively constant for a wide range of the Reynolds numbers. It also demonstrates that the diameter of

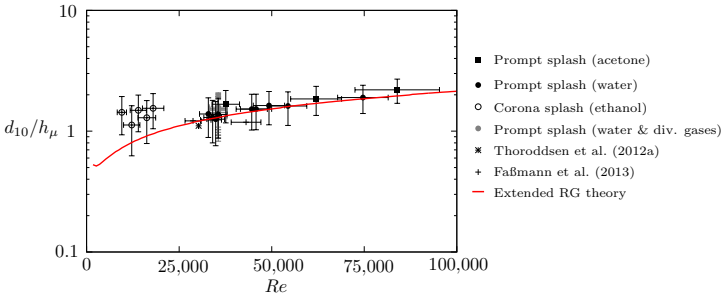

Figure 3.17: The arithmetic mean diameter of the ejected droplets scaled by $h_\mu = DRe^{-1/2}$. The available experimental data for the corona and prompt splash is plotted together with the prediction made using the extended RG theory and previous experiments conducted using water drops. Reprinted from Burzynski et al. (2020).

the secondary droplets produced by the high-speed impact on smooth dry surfaces scales well with the length scale $h_\mu = DRe^{-1/2}$.

> The normalized droplet size distribution in a splashing regime is weak dependent of the kinematic impact conditions and surrounding gas; however, it differs drastically between the corona and prompt splash.

3.4.2 Velocity of the secondary droplets

Part of the text described in this section has already been published in Burzynski and Bansmer (2019c) and Burzynski et al. (2020).

The velocities of the secondary droplets resulting from the prompt and corona splash are shown in figure 3.18, where each point on the graph corresponds to a single detected droplet. The data represent the correlations between the velocity magnitude and size, the velocity components, and the ejection angle and size of the secondary droplets. These diagrams demonstrate the difference between the corona and prompt splash, which are manifested not only in the droplet sizes but also in their velocities. For better visualization purposes, the color in the range of scale in figure 3.18 is set up to $\tau = 6$, although the splashing phenomena were captured for both regimes until $\tau \approx 10$. The measurement results indicate that a certain velocity does not necessarily correlate to a specific droplet diameter; thus, a direct relationship such as $u \sim \sqrt{\nu_l DU}/d$ (Thoroddsen et al., 2012a) is not appropriate to describe the plethora of velocities observed.

A clear temporal trend can be identified in all diagrams of figure 3.18, showing that the velocity magnitude significantly exceeds the impact velocity $\sim 6U$ but then decreases with time. Thoroddsen et al. (2012a) demonstrated that the droplets decelerate by 30% just 40 μs after the pinch-off due to the aerodynamic forces acting on the droplets. Since the experimental set-up does not allow to capture the ejection velocity precisely at the beginning of splashing, the range of velocities measured in this study are lower than those calculated by the inviscid theories $u > 10U$ (Philippi et al., 2016, Riboux and Gordillo, 2015) at the pinch-off moment (Thoroddsen et al., 2012a). The presented results also show that the horizontal velocity of the droplets is almost independent of the surrounding gas. This evolution over time is also well predicted by theory and numerical simulations, as shown in figure 3.19. This

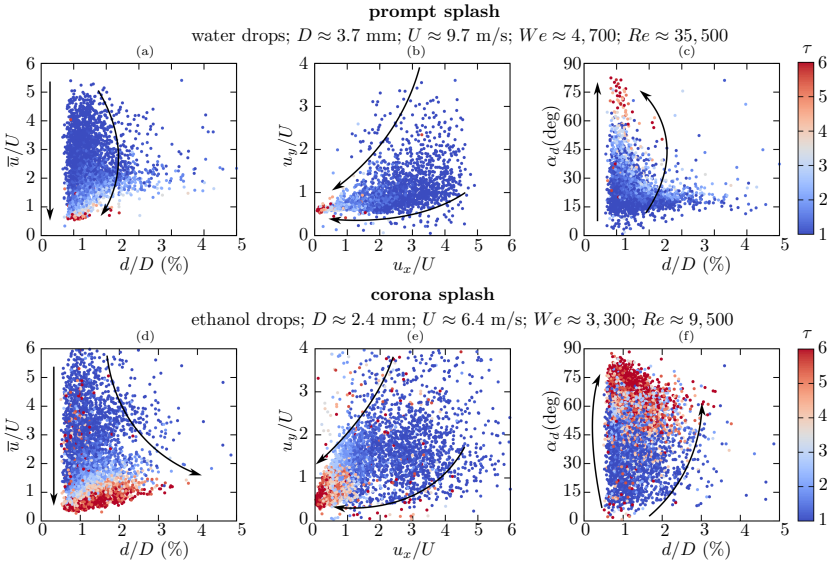

Figure 3.18: The velocity of the ejected droplets over their diameter, the velocity components, and the ejection angle. The colors indicate the dimensionless time τ, and the arrows highlight the tendency. Adapted from Burzynski et al. (2020)

reinforces the previous observation made by different authors, where $U \sim \tau^{-1/2}$ Riboux and Gordillo (2014), Thoroddsen et al. (2012a). Contrary to the droplet size and horizontal velocity, the vertical velocity of the droplets is affected by the gas and liquid properties. The ejection angle of the droplets is small at the beginning of splashing but later on increases drastically depending on the splashing regime. The differences in the ejection angles for each splashing regime become clearer after calculating its average over time. The results indicate that the ejection angle for the corona splash $\alpha_d \sim 47°$ is always larger than for the prompt splash $\alpha_d \sim 28°$. This is caused by the aerodynamic forces acting on the lamella, which deflect the lamella during its formation (Moore et al., 2018).

Mean velocity and angle over time

The evolution of the mean velocities and secondary droplet angles for various impact conditions are shown in figure 3.20. The mean mag-

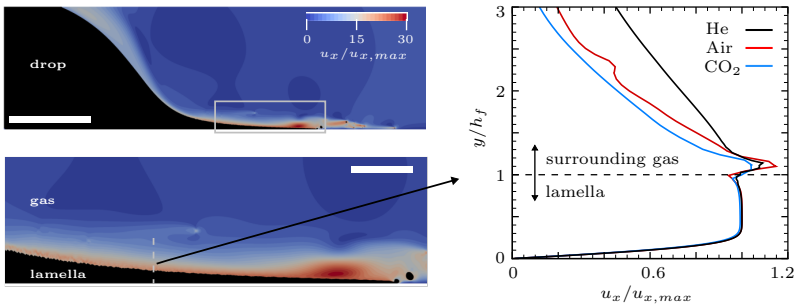

Figure 3.19: Horizontal velocity of the spreading lamella for a drop of $D = 3$ mm impacting at $U = 10.79$ m/s; scale bar 1 mm. The simulations show the velocity profile of the flow inside the lamella and of the gas just above it. The profiles are taken at $x = 3/4D$ and $\tau = 0.9$ when using different gases. Velocity scale in m/s.

nitude of the velocity decreases with time for all impact parameters, which reinforces the previous observation, where $U \sim \tau^{-1/2}$ (Riboux and Gordillo, 2014, Thoroddsen et al., 2012a).

The measurements indicate that this velocity is not influenced by surface tension or viscosity at the initial stage of drop impact and spreading. This is because the lamella spreading velocity is much higher than the relative Taylor velocity $U \sim \sqrt{2\sigma/(\rho_l h_\mu)}$ (Taylor, 1959), and the lamella is thicker than the viscous boundary layer, as accurately described by the inviscid solutions (Riboux and Gordillo, 2014, 2017, Roisman, 2009). Therefore, the effect of the liquid properties on the magnitude of the velocity is rather small. In fact, the extensive measurements presented here indicate that the mean velocity of the secondary droplets may be universal for high-speed impacts. This behavior is independent of the different liquids, gases, drop sizes, and impact velocities analyzed in this thesis. An example of this is also shown in figure 3.19, where the simulations demonstrate that the spreading velocity of the lamella is very similar in all the cases. However, the horizontal velocity of the gas on top of the lamella changes due to the differences in the momentum of the gases ($\sim \rho_g u$).

The mean ejection angle of the secondary droplets monotonically increases over time, as shown in figure 3.20(b). Its evolution is slightly affected by the splashing regime; as a result, higher ejection angles are detected in the cases corresponding to lower values of the Reynolds number. However, the experiments presented here capture the droplets

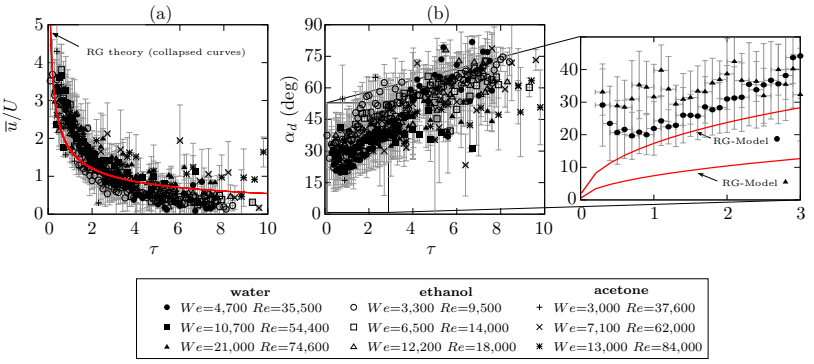

Figure 3.20: The evolution of secondary droplet velocities and angles over time. (a) shows the evolution of the measured mean droplet velocity and its agreement with the theoretical prediction ($\overline{u} \sim \tau^{-1/2}$) within the RG theory. (b) shows the evolution of the ejection angle over time and its theoretical estimation. The error bars represent the standard deviation calculated using equation 2.2. Reprinted from Burzynski et al. (2020)

once they have detached from the lamella. These small droplets are normally not spherical in the moment of detachment, as shown in figure 3.10. Therefore, the aerodynamic forces, such as drag and lift, may play an important role on the deformed droplets directly after the detachment and therefore should be considered. Lift in such small droplets may occur for different reasons; for example, because they are exposed to a shear flow field close to the wall (Cherukat and McLaughlin, 1994, Mannan and Leiderman, 2020, Saffman, 1965), they can rotate from the slingshot mechanism (Thoroddsen et al., 2011), causing the Magnus effect (Kray et al., 2012), and also because they deform when flying away from the rim (Armandoost et al., 2018).

> The time evolution of the secondary droplet velocity is weak dependent of the impact conditions for high-speed impacts.

3.4.3 Total ejected volume during splashing

Part of the text described in this section has already been published in Burzynski and Bansmer (2019c) and Burzynski et al. (2020).

Although the characterization of the secondary droplets has revealed important information about splashing, it is of extreme importance for a host of technical applications to know the volume of the primary droplets that fly away during splashing. In the performed experimental studies, the total ejected volume during splashing V_{tot} was calculated using the extrapolation method, as explained in section 2.3. As it is later shown, the ejected volume depended on the splashing regime. Figure 3.21(a) quantifies these large differences in the generation of secondary droplets between the corona and prompt splash over time. The results demonstrate that in the prompt splash regime the droplets are generated over a short period of time, while in the corona splash regime the droplets are expelled for longer due to the corona formation and the subsequent break-up.

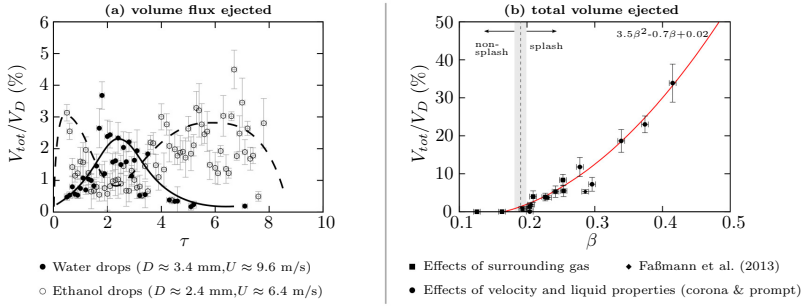

Figure 3.21: Total volume ejected during splashing. (a) illustrates the volume flux ejected over time in the prompt and corona splash regimes. (b) shows the ratio between the total secondary volume ejected and the initial drop volume as a function of the splashing parameter β for all the experimental data available. Adapted from Burzynski et al. (2020).

Two peaks can be observed in the ejected volume in the corona splash regime over time, suggesting two main instabilities in the spreading lamella. The first instability was captured at the very beginning of splashing when the ejected lamella moves very fast. The atomization process starts in this case with the rim instability and generates a notable quantity of droplets. Then the viscous forces decelerate the lamella considerably, and the corona can be fully formed above the surface. During this process, fewer droplets are expelled from the rim. The second and major peak in figure 3.21(a) results afterwards, when the unstable film breaks up, atomizing the entire corona rapidly. It has to be kept in mind that τ in figure 3.21(a) represents the time at

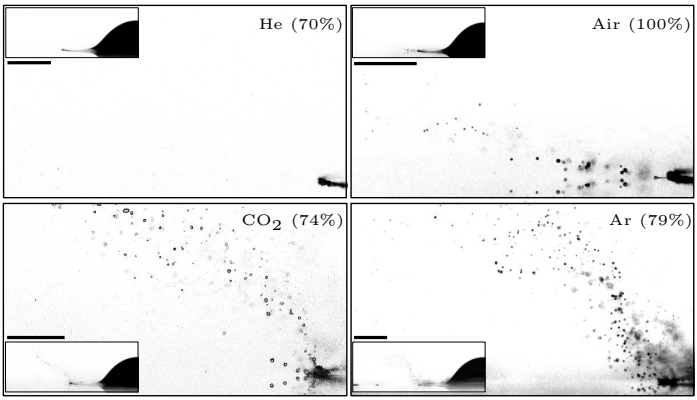

Figure 3.22: The role of the surrounding gas on the splashing outcome. This effects are well predicted using the theory of Riboux and Gordillo (2014). The scale bars are 500 μm. Adapted from Burzynski and Bansmer (2019c).

which the droplet passes through our control surface and not the time at which the droplets break-up from the rim of the expanding lamella, as explained in section 2.2 and shown in figure 2.7. Note that the uncertainty of the ejected volume shown in these images is the result of the error propagation of each measured quantity, as explained in section 2.3.

The images in figure 3.22 show an example of how the properties of the surrounding gas change the outcome of splashing. To determine which property of gas affects the splashing the most, the number of droplets and total ejected volume were analyzed after changing the surrounding gas. By taking two gases with similar viscosities but significantly different densities, $\Delta\rho_g \approx 60\%$ (He(70%) and air), it can be observed that the total volume loss V_{tot}/V_D differed by approximately 99%. By comparing another two gases with similar densities but different viscosities, $\Delta\mu_g \approx 30\%$ (CO_2(74%) and Ar(79%)), V_{tot}/V_D varied by approximately 34%. The comparison of He(95%) and He(70%) shows that the mean free path changes $\Delta\lambda_g = 50\%$ but $\Delta\mu_g < 7\%$; it was also noted that the total volume loss V_{tot}/V_D changed from 0 to 2%, suggesting that the mean free path has almost no influence on the total volume, taking into account that $\lambda_g \propto \rho_g^{-1}$. It can then be concluded that the most dominant property of gas affecting the gen-

eration of secondary droplets is the density, followed by viscosity and mean free path. This conclusion is also valid for the total number of ejected droplets since the droplet size distribution is independent of the properties of the gas.

According to Riboux and Gordillo (2014), the generation of secondary droplets is caused by the lift force acting on the spreading lamella, which results from the combination of the lubrication force exerted by the gas beneath the lamella and the aerodynamic suction force exerted above the lamella. This theory states that by increasing the vertical velocity of the lamella (due to the acting lift force on the lamella) a point is reached where this velocity is equal to the capillary retraction velocity; above this limit, the lamella gradually starts to fragment into secondary droplets. The balance between these velocities leads to the previously mentioned splashing parameter in equation 3.5, which reads as $\beta = \sqrt{F_L/(2\sigma)}$. It is then reasonable to expect that this ratio is directly proportional to the quantity of ejected droplets, as shown in figure 3.21(b). The measurements presented in this thesis corroborate that the splashing on dry surfaces is indeed evoked by the lift force acting on the spreading lamella.

> Splashing on dry smooth surface is caused by a lift force acting on the spreading lamella. The break-up of this lamella is primarily affected by the density, followed by viscosity and mean free path of the gas.

3.4.4 Extension of RG's theory

Part of the text described in this section has already been published in Burzynski and Bansmer (2019c) and Burzynski et al. (2020).

The size, velocity, and the total ejected volume of the secondary droplets can be estimated using the theory of Riboux and Gordillo (2014). The estimation of the size and velocity is based on the fact that the droplets are expelled directly from the spreading lamella; therefore, these quantities correspond to the thickness and velocity of the lamella tip. The droplets are expelled if the lamella de-wets the surface and its tip moves faster than the wetted region. To estimate the dimensionless ejection time of the lamella τ_e, its thickness h_l, and velocity u_l, Riboux and Gordillo (2014) considered the liquid flow as both inviscid and incompressible, allowing the use of potential and Wagner's theory (Wagner, 1932). The first step of applying the RG theory to model

the drop splashing is to determine the ejection time T_e and then the tangential velocity U_l and its corresponding thickness H_l. The ejection time is estimated assuming that the dimensionless radius of the region wetted by the drop $a(\tau) = R_{wet}/R$ is parallel to the ejecta sheet in the moment of ejection. Using Wagner's theory, Riboux and Gordillo (2014) estimated that the wetted region evolves as $a(\tau) = \sqrt{3\tau}$. If this wetted region is passed by the tip of the lamella, it gets ejected over the surface. Therefore, the condition for ejection can be estimated using the momentum equation

$$\frac{Du_l}{D\tau} = -\frac{\partial p^*}{\partial x} + \frac{1}{Re_R}\nabla^2 u_l \geq \ddot{a}, \tag{3.10}$$

where p^* is the dimensionless pressure defined as $p^* = p/(\rho_l U^2)$. By neglecting surface tension and viscous effects and applying the steady Euler-Bernoulli equation ($p + \rho_l U_l^2/2 = \rho_l \dot{R}_{wet}^2/2$) to estimate the momentum inside of the spreading droplet, Riboux and Gordillo (2014) determined the related approximations of the unknown terms from equation 3.10. They concluded that $\partial p^*/\partial x \sim Re_R^{-2} Oh_R^{-2}/h_l^2$, $\nabla^2 u_l \propto \tau_e^{-1/2}/h_l^2$, and $\ddot{a} \propto \tau_e^{-3/4}$. Using those estimations in the ejection condition (equation 3.10), the dimensionless ejection time is calculated as

$$\frac{\sqrt{3}}{2} Re_R^{-1} \tau_e^{-1/2} + Re_R^{-2} Oh_R^{-2} = 1.21 \tau_e^{3/2}, \tag{3.11}$$

where the Reynolds and Ohnesorge numbers are defined as $Re_R = \rho_l U D/(2\mu_l)$ and $Oh_R = \mu_l/\sqrt{\rho_l D/(2\sigma)}$, respectively. The thickness of the lamella at the rim position is calculated from the flux of tangential momentum per unit length, which is shown to behave like $\sim \rho_l U^2 R$. The velocity of the film is estimated from the speed relative to the wall, which is given by $u_l = 2a = \sqrt{3/\tau_e}$. Using the experimental data available, Riboux and Gordillo (2014) concluded that the lamella thickness and velocity can be approximated as

$$h_l = \frac{\sqrt{12}\tau_e^{3/2}}{\pi}, \tag{3.12}$$

$$u_l = \frac{1}{2}\sqrt{\frac{3}{\tau_e}}. \tag{3.13}$$

The dimensional quantities of the ejection time, thickness, and velocity correspond to

$$T_e = \tau_e D/(2U), \quad H_l = h_l D/2, \quad \textit{and} \quad U_l = u_l U. \tag{3.14}$$

It should be noted that the dimensionless parameters in the RG theory are defined using the drop radius $D/2$ instead of the diameter, as commonly done in the literature related to drop impacts.

In the case of prompt splash or corona splash with short corona, the droplets are ejected near the surface; therefore, the effects of viscous shear force at the spreading rim must be taken into consideration (Riboux and Gordillo, 2015, 2017). This shear force affects the velocity and the rim thickness simultaneously over time. It increases the rim thickness at the radius a of the wetted region from h_a to h_a^+ and decreases its horizontal velocity from $u_{a,x}$ to $u_{a,x}^+$ (see figure 3.12 for an illustrated representation). The force per unit length in the spreading drop was estimated in Riboux and Gordillo (2015) as $F \sim \mu U_l R/\Delta u_{a,x} h_a$, where Δ is the width of a boundary layer. Again using mass and momentum balance in the spreading lamella and considering the mentioned viscous forces, Riboux and Gordillo (2015) showed that the lamella thickness and velocity are better expressed as

$$h_a^+ = \frac{h_a}{(1-\sqrt{2}/\sqrt{Re_R u_a h_a})}, \tag{3.15}$$

$$u_{a,x}^+ = u_a(1-\sqrt{2}/\sqrt{Re_R u_a h_a}), \tag{3.16}$$

where $h_a = h_l/3$ and $u_a = 2u_l$. The droplet size and horizontal velocity can be determined as $d_{model} \sim R h_a^+$ and $u_{x,model} \sim U u_{a,x}^+$, respectively.

This theory reveals that the first secondary droplets for a water drop impact at $We \approx 5,000$ and $Re \approx 35,500$ under atmospheric air pressure are ejected at $T_e \simeq 1.7$ μs with a diameter of $d_{model} \sim 3$ μm and a velocity of $u_{x,model} \sim 80$ m/s. Such impact conditions correspond to top right image of figure 3.22. These estimated values agree well with the measurements of Thoroddsen et al. (2012a), who conducted experiments under almost identical conditions.

The RG theory attributes splashing to the aerodynamic lift force acting on the lamella. The force F_L is defined as the sum of the viscous force induced by the gas beneath the lamella and the suction force at the top of it, which reads as follows:

$$F_L = K_{lub}\mu_g U_l + K_u \rho_g U_l^2 H_l, \tag{3.17}$$

where $K_{lub} \simeq -2(\ln(19.2\lambda_g/H_l) - \ln(1+19.2\lambda_g/H_l))$ is a variable obtained from the lubrication theory, $K_u = 0.3$ is a drag coefficient obtained from numerical simulations. This model also accounts for the effective slip, which is relevant to describe the thin layers of the rarefied

gases (Gordillo and Riboux, 2019). The vertical velocity of the lamella $U_{l,y}$ can be estimated from the force balance in the vertical direction $\rho_l H_l^2 U_{y,l} \propto F_L$ (Riboux and Gordillo, 2017), which leads to an approximated dimensional vertical velocity of $u_{y,model} \sim 10U\sqrt{F_L/(\rho_l H_l U_l^2)}$. Further details on the RG theory and its complete derivation can be found in Gordillo and Riboux (2019), Riboux and Gordillo (2014, 2015, 2017).

This theoretical approach does not provide any information about the elapsed time for the generation of secondary droplets. However, this elapsed time must be known; otherwise, the model estimates a continuous increase in the droplet size over time, as can be noted from equations (3.12, and 3.15), where $d_{model} = Rh_a^+ \sim \tau^{3/2}$. To extend the RG theory in this direction, the splashing duration was calculated by making use of the Rayleigh-Taylor instability analysis from section 3.3.2. This analysis demonstrates that the ejection time is determined by the process of multiple jet formation at the edge of the expanding lamella. The splashing duration is estimated using the growth rate of the fastest unstable mode in the spreading film caused by Rayleigh-Taylor instability, which reads as

$$\omega \approx \frac{UWe^{1/2}}{\sqrt{2}DRe^{1/4}}. \tag{3.18}$$

This expression is made dimensionless using the impact condition U/D, yielding to

$$\tau_d \sim U/D\omega. \tag{3.19}$$

By combining those equations, the splashing duration is predicted to be

$$\tau_d \approx Re^{1/4}We^{-1/2}. \tag{3.20}$$

The estimations using this equation were presented in Burzynski et al. (2020), and they agree with the ultra-high-speed images from the experiment of (Thoroddsen et al., 2012a), where they observed that most of the secondary droplets in the prompt splash regime were generated in the first 100 μs after the impact, i.e., $\tau_d = 0.2$. Using the equation (3.20), the duration of splashing in the experiments of (Thoroddsen et al., 2012a) is predicted as $\tau_d \approx 0.18$.

The total ejected volume can be estimated within this theory using the splashing parameter β, which determines that if the lift force F_L acting on the lamella is greater than the retraction force due to capillarity, the lamella starts to detach from the surface and then atomizes into secondary droplets. It is then reasonable to expect that this ratio is directly proportional to the quantity of ejected droplets. The large

number of experiments conducted in this study for different liquids, droplet sizes, and impact velocities allowed to develop a semi-empirical model in the following form:

$$\frac{V_{tot}}{V_D} = 3.5\beta^2 - 0.7\beta + 0.02, \tag{3.21}$$

which is applicable to a wide range of Weber and Reynolds numbers. This expression can be used to predict the total ejected volume regardless of the splashing regime, kinematic conditions, and the surrounding gas.

Comparison with the experimental data

The extension of the RG theory using the expression for the characteristic time of the corona instability allows calculating the arithmetic mean diameter of the secondary droplets for the prompt splash with high accuracy. The measurement results and the estimations using this approach are shown in figure 3.17 for a wide number of impact conditions. It should be noted that equation (3.20) is valid only for the prompt splash or corona splash with a short corona, where the Rayleigh-Taylor instability is the main mechanism causing the splashing. For the corona splash, the generation of secondary droplets takes more time, and different instabilities may play an important role. This explains why this extended model underestimates the secondary drop diameters for small Reynolds numbers, corresponding to the fully developed corona splash.

The mean velocity of the secondary droplets can also be well predicted using the RG theory, as shown in figure 3.20(a). The measurements demonstrate that the evolution of the average velocity follows the dependence $\overline{u} \sim 1/\sqrt{\tau}$ predicted by the RG theory within the equation (3.16) and also measured in (Thoroddsen et al., 2012a) This theoretical approach together with the experiments demonstrates that the mean velocity of the secondary droplets is indeed universal for high-speed impacts. Figure 3.20(b) shows that this theory accurately predicts the tendency of the ejection angle for moderate impact velocities over time. The RG theory predicts a decrease of this angle by increasing the impact velocity; however, the measurements and the images in figure 3.11 clearly demonstrate an increase in the ejection angle. One possible reason for this discrepancy may be the influence of the aerodynamic forces acting on the droplets once they detach from the rim, such as drag or lift; additionally, the dynamics of the jets appearing during the prompt splash are not considered in the RG theory.

Therefore, the RG theory is not applicable to accurately predict the ejection angle of secondary droplets, but its tendency is well predicted by the model. Figure 3.22 shows some further examples of the effect of the surrounding gas in the generation of secondary droplets, which can be estimated using the RG theory.

The model to describe the total ejected volume is verified using all the experimental data available. Figure 3.21(b) clearly shows that β is indeed directly proportional to the number of ejected droplets and the total ejected volume. The evaluation of more than 1000 individual impacts for each impact condition provides a solid dataset for statistical determination of the impact outcome. The equation 3.21 accurately predicts the total ejected volume from the measurements presented here as well as for the available experimental data. Moreover, it allows to explore the conditions at which a drop would entirely atomize into secondary droplets $V_{tot} = V_D$. This hypothetical case leads to $\beta = 0.64$, and in order to reach such value, an undisturbed water droplet of $D = 1$ mm would have to impact the surface at 75 m/s under normal ambient pressure. These conditions lead to a limiting Weber number of $We \approx 77,000$. However, it is quite unlikely that such a large drop would not deform itself due to the large lubrication pressure beneath the drop. This deformation would drastically change the impact conditions, and, in an extreme case, the drop would break up before contacting surface, as shown by the experiments of Garcia-Magariño et al. (2018). Nevertheless, all the available experimental data together with the extension of the RG theory presented here demonstrate that β is not only useful to determine whether splashing occurs or not, but also to predict the size, velocity, and total ejected volume of secondary droplets generated in these high-speed impacts.

> The extended RG theory can be used to predict with high precision the size, velocity, and total ejected volume of the secondary droplets.

3.5 Spreading dynamics at the surface

After the secondary droplets are ejected from the rim, the drop mass that sticks on the surface continues spreading until a maximum is reached. During this time, the thin lamella is bounded by a relatively thicker rim with several undulations in azimuthal direction. The

spreading rim is then formed by capillary forces. These undulations develop into more pronounced fingers once the maximal spreading diameter is reached, as observed in figures 3.4 and 3.23. In this phase, the dynamics for low-speed impacts are governed mainly by inertial, viscous, and capillary effects. However, Roisman et al. (2009) demonstrate that the time evolution of the lamella thickness in high-speed impacts near the impact center is almost independent of the viscosity or surface tension. This spreading thickness decreases with time as $h_l \sim 1/t^2$. Later on, the spreading diameter increases while the lamella becomes very small, and the viscous forces dominate the internal flow. These viscous effects slow down the liquid and determine its thickness and rim shape, which can be described using primarily the Reynolds number (Rioboo et al., 2002, Roisman, 2009).

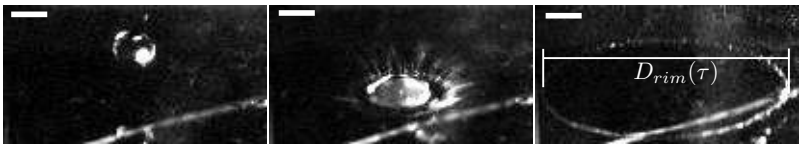

a) $\tau < 0$ b) $\tau > 0$ c) $\tau >> 0$

Figure 3.23: Measurements of the spreading diameter β_s using a high-speed camera (Shimadzu HPV-2) from a tilted perspective at $We \approx 5,000$. The images recorded the impact of water drops at 32,000 fps, showing (a) the droplet before the impact, (b) the ejection of secondary droplets, and (c) the estimation of the rim diameter D_{rim}. Adapted from Burzynski and Bansmer (2018b)

Figure 3.24 shows an example of how the dimensionless spreading diameter $\beta_s = D_{rim}/D$ evolves over time for low and high impact velocities. The impact at low velocity is, as mentioned above, dominated by viscous and surface tension forces; therefore, the rate of spreading as well as the maximal spreading diameter are strongly dependent on the liquid and surface properties. This results in a slower rate of spreading and a smaller maximal spreading diameter than the impact at moderate or high velocity. As the impact velocity increases, the rate of spreading and the maximal spreading diameter increase. However, the rate of spreading is independent of the initial impact velocity, as shown in figure 3.24. These observations corroborate the theoretical, numerical, and experimental analysis presented in the section 3.4.2, where it was shown that the velocity of the secondary droplets and simultane-

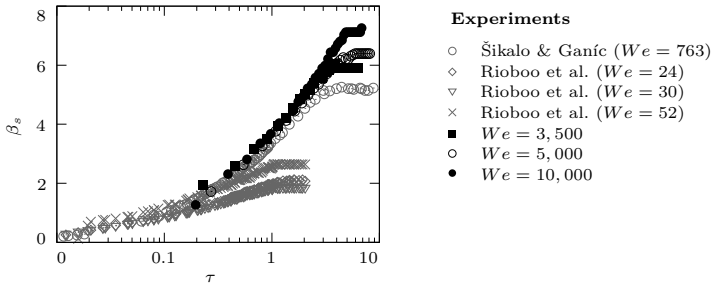

Figure 3.24: Time evolution of the spreading diameter β_s. The experimental results are compared with the data of Rioboo et al. (2002) and Šikalo and Ganić (2006) for low impact velocity. Adapted from Burzynski and Bansmer (2018b)

ously the velocity of the lamella are universal for high-velocity impacts. Contrary to the almost universal behavior of the spreading velocity, the maximal spreading diameter $\beta_{s,max}$ depends on the impact conditions, as it increases with the impact velocity. This can be explained by viscous effects, which slowly dissipate the kinetic energy of the impacting drop in the latter stages of the spreading. In other words, the higher the kinetic energy of the drop, the longer it would take to slow down the spreading lamella. As a consequence, a larger maximal spreading diameter can be reached. At the same time, the lamella thickness must decrease due to mass conservation.

Over the years, several models have been introduced to predict the maximal spreading diameter (Josserand and Thoroddsen, 2016). For example, Scheller and Bousfield (1995) performed several experiments and correlated the results with a combination of Ohnesorge and Reynolds numbers, as $\beta_{s,max} \sim 0.61(Re^2Oh)^{1/6}$. An alternative method to estimate the maximal spreading diameter was presented by Clanet et al. (2004), who assumed that the deformed drop would form a disk-like puddle at the moment of reaching its maximum. Based on this assumption, they used mass conservation to calculate the maximal spreading diameter as $\beta_{s,max} \sim We^{1/4}$. A more theoretical approach was presented by Roisman (2009) by taking into account an unsteady viscous flow to describe the residual thickness and maximal spreading diameter of the liquid film. In order to provide a simplified model in this approach, they estimated $\beta_{s,max}$ on the basis of mass conservation after

considering that the film accumulated in the rim can be neglected for high Weber numbers. These assumptions led to the following expression:

$$\beta_{s,max} = 0.87Re^{1/5} - 0.4Re^{2/5}We^{-1/2}, \tag{3.22}$$

where the coefficients are obtained empirically. Laan et al. (2014) used a similar scaling as proposed by Roisman (2009) and Eggers et al. (2010) and argued that $\beta_{s,max}$ behaves differently for two different regimes. One regime is the case of high viscosity liquids and the other describes the inviscid case. Their scaling leads to the following equation:

$$\beta_{s,max} = Re^{1/5}P^{1/2}/(C_A + P^{1/2}), \tag{3.23}$$

where $P = WeRe^{2/5}$ and $C_A = 1.24$ is an experimental fitting constant. When viscosity dominates the spreading phase $P \gg 1$, in the inviscid case $P \ll 1$. More recently, Gordillo et al. (2019) proposed a different approach to estimate the thickness and maximal spreading lamella by coupling the instationary flow in the spreading film with the expanding flow in the rim. Similarly to the analysis of Roisman (2009), this method quantifies the fluxes of mass and momentum over the spreading phase. The expression of this recent theory for $\beta_{s,max}$ reads as follows:

$$We^{-1}\beta_{s,max}^2 + 0.45Re^{-1/2}\beta_{s,max}^{5/2} - 0.45 = 0, \tag{3.24}$$

where the physical result is the positive real solution from this equation. This theory seems to describe very well the initial phase of spreading, where the previous theories were less accurate.

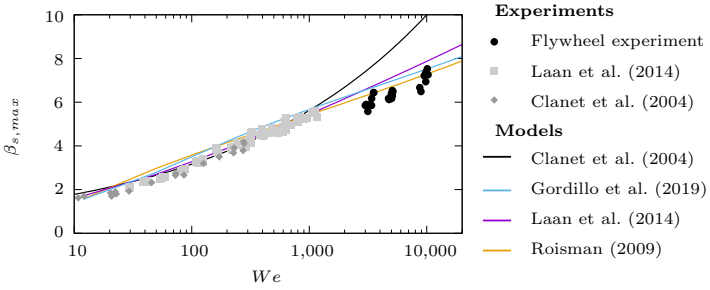

Figure 3.25: Maximal spreading diameter $\beta_{s,max}$ as a function of the Weber number. The lines represent the different models proposed.

To compare these theories, the obtained results for this thesis and the results of other authors are shown together with the recent models in figure 3.25. This figure shows the maximal spreading diameter $\beta_{s,max}$ as a function of the Weber number. The results demonstrate that all the recent models predict $\beta_{s,max}$ rather well for different impact velocities. It is interesting that all the recent models describe well the maximal spreading diameter in a wide range of conditions, even when the approach of each model and their formulations are quite different. However, the models of Scheller and Bousfield (1995) and Clanet et al. (2004) overestimate the experimental results when the drops impact at a very high velocity.

The maximal spreading diameter for high-speed impacts can be accurately predicted by taking into account inertial, viscous, and capillary forces.

4 Drop splashing on wetted surfaces

In this chapter, the splashing of high-speed drops on thin films of the same liquid is analyzed, with particular focus on the crown formation and break-up dynamics. The purpose of this chapter is to elaborate on the physical phenomena underlying the generation of secondary droplets and to provide an accurate theoretical approach that can describe and model the outcome of splashing at high impact velocities.

Similarly to the previous chapter, this section is structured according to the evolvement of the drop dynamics over time. It starts with the gas entrapment mechanism, moving on to the crown formation and break-up, and concluding with the collapse of the formed liquid sheet and the final delayed splash. Some of the results presented in this chapter are taken with slight adaptation from Burzynski and Bansmer (2018a), Burzynski et al. (2020).

4.1 Evolution of splashing on thin films

The time evolution of a drop splashing on a wetted surface of the same liquid can be divided into four fundamental phases:

1. **Gas entrapment** before the drop contacts the film with a later formation of micro-bubbles between the free surfaces;
2. **Ejecta sheet formation** with a strong bending of the free sheet leading to the break-up and ejection of the first secondary droplets;
3. **Crown formation** and development until the maximal extension with continuous generation of larger secondary droplets;
4. **Crown collapse** with the crown receding back to the film or its complete atomization into the largest droplets.

These phases are illustrated in figure 4.1 and provide a basic representation of the complex splashing phenomenon that occurs at moderate

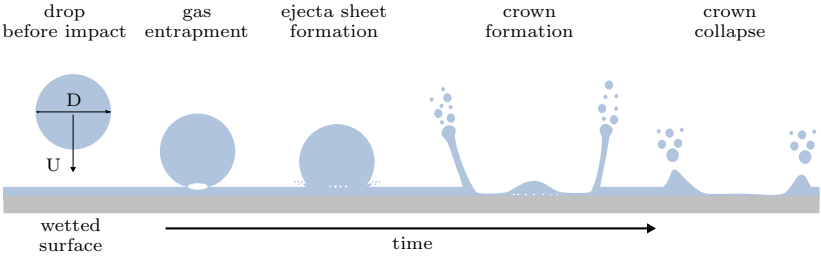

Figure 4.1: Sketch of the time evolution of an impacting drop on a wetted surface for moderate and high impact velocities.

and high impact velocities. A similar approach to define the phases of splashing for low impact velocities has been proposed by Cossali et al. (1997). These authors proposed to separate the splashing in the following phases: crown formation, rim instability, break-up into secondary droplets, and crown collapse. However, the gas entrapment mechanism is missing in this description because it was reported for the first time some years later by Thoroddsen et al. (2003).

The proposal of Cossali et al. (1997) is a widely accepted concept for describing the impact at relatively low velocity, but, as it will be demonstrated in this thesis, the drop impact at moderate and high velocity leads to the propagation of instabilities in the lamella from the early to the final stages of impact. These instabilities promote the break-up of the ejected thin liquid sheet during the entire splashing process, as shown in figure 4.2. As a result, the crown formation, instability propagation, and liquid break-up occur almost immediately after the drop contacts the film without a clear time delay between these phenomena. Unlike proposed by Cossali et al. (1997), the formation of instabilities in the crown and the subsequent break-up into secondary droplets are considered in this thesis as a part of the ejecta sheet and crown formation phases during the high-speed impacts.

4.2 Dynamics at the early stage of impact

When a drop approaches the thin liquid film, part of the surrounded gas is compressed beneath the drop. The increase in pressure deforms the drop and the film surface prior to the impact; subsequently, a disk of gas is entrapped between both free surfaces at the moment of contact (Thoroddsen et al., 2003). The dynamics of this entrapment mechanism

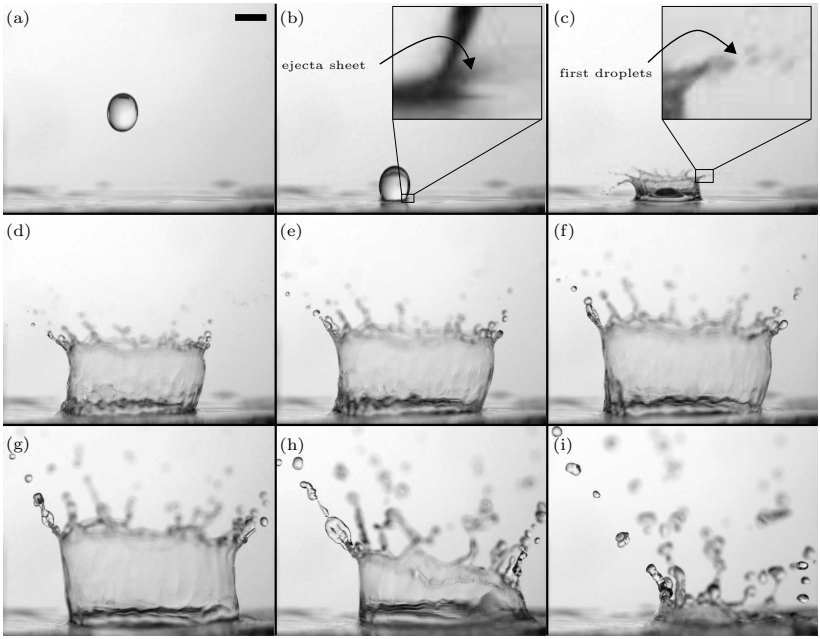

Figure 4.2: Typical outcome of a large drop of $D = 4.4$ mm impacting on a thin film of the same fluid at moderate impact velocity $U = 3.8$ m/s. The film thickness and velocity are $h_f = 0.4$ mm and $U_f = 0.07$ m/s. The panels show (a) the drop before impact, (b) the ejecta sheet and the ejection of the first secondary droplets, (c-f) crown formation until the maximal extension, (g-i) crown collapse and ejection of the final droplets. Recording time $6,200$ fps and scale bar 4 mm.

are described by the lubrication theory in the gas, similarly to drop impacts on dry solid surfaces. In the theory proposed by Hicks and Purvis (2011), the compressibility effects in the gas play an important role when

$$U \gg \frac{p^{3/7}\mu_g^{1/7}}{\rho_l^{4/7}(2D)^{1/7}}. \tag{4.1}$$

For a water drop of $D \approx 3.5$ mm, the theory implies that compressibility effects are relevant when the drop impacts at a velocity larger that 3 m/s. Hicks and Purvis (2011) provided the corrections to be applied in the lubrication theory in order to estimate the conditions for the gas entrapment. The theory predicts the entrapment of a gas layer between

both free surfaces when neglecting or accounting for gas compressibility.

Some instants after the gas becomes entrapped, the thin gas disk ruptures due to a combination of azimuthal and longitudinal instabilities in the ring of micro-bubbles (Thoraval et al., 2013). However, if the thickness of the gas disk is less than 100 nm, the van der Wals forces dominate and lead to the rupture (Tran et al., 2013). Hendrix et al. (2016) quantified the entrapped volume V_b and demonstrated that this quantity is proportional to $\sim St^{-4/3}V_D$, where $St = \rho_l DU/(2\mu_g)$ is the Stokes number. This implies that the ratio between the entrapped volume and the drop varies in this study between approximately 8.3×10^{-9} and 3.6×10^{-8}. It is very interesting that the volume ratio decreases with an increase in the impact velocity or drop diameter. This means that at a certain velocity no gas should be entrapped.

As mentioned previously, Hicks and Purvis (2013) demonstrated that the gas bubble diameter and, therefore, the volume become independent of the compressibility effects when the energy conservation equations are included in the gas phase. Li et al. (2017) demonstrated that the ring of microbubbles can also be the result of a double contact of the drop with the film, but only in a rarefied gas regime. This double contact forms a toroidal strip of gas, which contracts by rupturing and thus generates larger bubbles. Although micro-bubbles were expected in all the experiments conducted here, this phenomenon was not observed due to the different conditions used here (non-rarefied gas regime) and the restriction caused by the large crown that developed between the expected location of bubble formation and the camera. Additionally, as the thin film was inevitably moving, the transport of the small bubbles with the film made the tracking of the bubbles once the crown had collapsed very challenging. Nevertheless, it is to expect that some gas amount is entrapped for the experiments conducted here with a thin moving film, as all the previous investigations indicate (Hicks and Purvis, 2011, Josserand et al., 2016, Marston et al., 2011, Thoroddsen et al., 2003, Yarin, 2006).

Shortly after the drop contacts the film, a thin sheet is ejected at high velocity from the neck between both liquids. The ejecta sheet is generated as the liquid interface is violently displaced outwards due to the large velocity difference between the fast-oncoming drop and the relatively slow-moving film (Yarin, 2006). This ejecta sheet was first predicted by Weiss and Yarin (1999) using numerical simulations and some years later confirmed by the remarkable experiments of Thoroddsen (2002). From a more analytical point of view, Howison et al. (2005) adapted the inviscid theory of Wagner (1932) to predict the ejecta sheet

in liquid-liquid interactions. Such adaptation is necessary since Wagner's theory was first postulated considering the impact of solids on liquids. However, this theory has some limitations because it predicts that the ejected jet is infinitely long and thin with a velocity tending to infinity near the jet tip; hence, it is only suited to provide estimations about the root of the ejecta sheet (Cimpeanu and Moore, 2018, Howison et al., 2005, Moore et al., 2018).

The dynamics of the ejecta sheet can be very different when changing the impact velocity and physical properties of the liquids. For example, in the case of high viscosity and low impact velocity, the ejecta sheet bends during its development, in some cases contacting the film again (Thoroddsen, 2002). An increase in the impact velocity leads to the break-up before the sheet contacts the films; this is, in fact, the first moment of droplet generation (Thoroddsen et al., 2011, Zhang et al., 2012a). In the case of high-speed drops and low viscosity, the lamella bends even stronger, forming a very irregular structure, which subsequently generates a spray of secondary droplets. This irregular form and the formation of the first droplets are shown in figure 4.2(b) and in more detail in the high-resolution image and simulations of figure 4.3. Thoraval et al. (2012) studied the transition from this slightly bent ejecta sheet to the irregular and broken lamella. They used numerical simulations to demonstrate that the lamella becomes unstable when

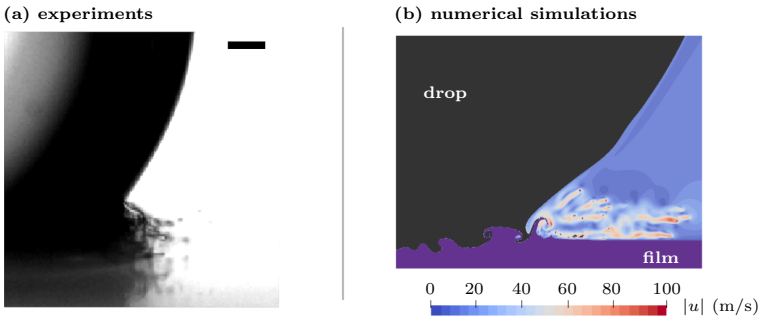

Figure 4.3: Chaotic ejecta sheet and the ejection of the first secondary droplets. (a) shows a large drop $D \approx 4$ mm impacting at $U \approx 10$ m/s on a thin film and the formation of the ejecta sheet. Scale bar 250 μm. (b) reveals the von Kármán-vortex-like instabilities between the liquids and the air velocity field. The simulation represents a drop of $D = 3$ mm impacting at $U = 10.79$ m/s on a film moving at $U_f = 1$ m/s.

the Reynolds number is increased, forming a von Kármán vortex street between the drop and film liquid. The generated vortex promotes the break-up of the ejecta sheet at the ejection moment. Castrejón-Pita et al. (2012) confirmed for the first time the existence of these von Kármán vortices between the drop and the film using experimental methods. The ejection of this thin lamella, whether it breaks up or not, induces the formation of the large crown (Agbaglah et al., 2015). The numerical simulations performed in this study also reveal that the formation of the chaotic ejecta sheet during high-speed impact is induced by von Kármán-like vortices formed between the interface of the liquids, as shown in Thoraval et al. (2012).

The first secondary droplets are ejected at the earliest stage of impact when the ejecta sheet breaks up.

4.3 Crown formation and evolution

After the thin ejecta sheet emerges between the drop and the liquid film, it expands continuously, forming a crown-like liquid sheet almost normal to the surface. At the top of this crown, a notable portion of liquid mass always accumulates, forming a thick free rim. This rim is the result of capillary forces acting on the liquid sheet. The theory proposed by Yarin and Weiss (1995) describes the crown formation as a result of a kinematic discontinuity in the film thickness and velocity distributions. A mass sink in the front of this discontinuity forces the liquid to be expelled parallel to the discontinuity, as illustrated in figure 4.1 and shown in figure 4.4.

Multiple numerical and experimental studies have proved the theory of Yarin and Weiss (1995) by showing the good prediction capability of the theory, even though it neglects the effects of the surrounding gas, viscosity, and gravity(Josserand and Thoroddsen, 2016, Liang and Mudawar, 2017, Moreira et al., 2010, Yarin et al., 2017). By generalizing this theory for arbitrary impact velocity vectors, Roisman and Tropea (2002) concluded that these effects indeed do not drastically affect the crown formation in high-velocity impacts; therefore, the impact dynamics are primarily dominated by inertial forces. According to these investigations, it can then be expected that the quantities affecting the crown formation are only the drop diameter D, the impact

Figure 4.4: Example of the crown formed during the drop splashing on thin films from different perspectives demonstrating the limitations of observing the impact only from a lateral perspective.

velocity U, the film thickness h_f, and the mean film velocity U_f. However, more recent experimental data indicate that the thickness of the crown lamella depends on the liquid viscosity since it has been shown in multiple occasions that this thickness scales well with the boundary layer thickness as $h_\mu \sim DRe^{-1/2}$ (Kittel, 2019, Roisman et al., 2006, Visser et al., 2012). The effect of viscous forces indeed plays a more important role in the crown formation process than assumed by Yarin and Weiss (1995). In fact, the viscous effects slow down the spreading of the lamella, leading to thicker crowns (Kittel, 2019); as a consequence, the secondary droplets ejected during the break-up are larger and slower than those ejected at the early stage of splashing.

The use of liquids with different physical properties leads to a very complex scenario, where each liquid may lead to the production of different lamellae depending on whether the liquids are miscible or not. In such cases, the splashing produces a double crown formation, which leads to a bimodal droplet size distribution (Kittel, 2019, Murphy et al., 2015). Since this study concentrates on the outcome of splashing from liquids with the same properties and with air as the surrounding gas, the reader is referred to the recent contributions of Aljedaani et al. (2018), Chen et al. (2017), Geppert et al. (2017), Kittel (2019), Liang and Mudawar (2017) for further details on different outcome scenarios when different liquids are used. Contrary to this significant role of liquid properties on splashing, several studies have shown that the surrounding gas seems not to affect the crown formation process (Guo et al., 2016, Liang et al., 2014a, Zhang et al., 2012b). This is particularly true when the density ratio ρ_l/ρ_g is large, which is the case in the

present investigation.

As the inertial forces are the most dominant in the high-speed drop splashing, a slight increase in the drop diameter D or impact velocity U alone can promote the crown formation and the subsequent generation of many secondary droplets. According to the theory of Yarin and Weiss (1995), the crown emerges if the condition

$$U \gg \left(\frac{\sigma}{\rho_l}\right)^{1/4} \nu_l^{1/8} (U/D)^{3/8} \tag{4.2}$$

is satisfied. This expression is equivalent to the forces balancing expression $K = WeOh^{-2/5} \gg 1$, which has been defined in Mundo et al. (1995) for impacts on dry surfaces. Cossali et al. (1997) adapted this formulation for impacts on wetted surface and demonstrated that the boundary between deposition and splashing in such cases can be defined as a function of the dimensionless film thickness as

$$K = WeOh^{0.4}/(2100 + 5888\delta^{1.44}), \tag{4.3}$$

where $\delta = h_f/D$ is the dimensionless film thickness. This expression implies that the generation of secondary droplets is expected if $K > 1$. More recently, Gao and Li (2015) extended this threshold definition to the case of thin moving films leading to a generalized expression which reads as follows:

$$K = WeRe^{1/2}(1 + \delta u^{*2})(1 + \delta u^*)^{1/2}, \tag{4.4}$$

where $u^* = U_f/U$ is the dimensionless film mean velocity. The adapted K-model presented in Gao and Li (2015) indicates that the splashing would occur when $K > 3378$. Note that this kind of formulation of splashing using the K parameter is valid for the drop impact on films since the outcome is almost independent of the surrounding gas. However, this is not the case when drops impact on dry surfaces, as explained in chapter 3.

Although splashing is expected when the impact velocity exceeds the splashing threshold velocity, the outcome of splashing at moderate and high velocity can be very different. As shown in figure 4.5, the high-speed impact leads to a smaller crown thickness and a chaotic shape with multiple undulations. Interestingly, the numerical simulations performed by Guo et al. (2016) on films at rest also indicate that the crown becomes chaotic at very high Weber and Reynolds numbers. This is also confirmed within the numerical simulations presented in

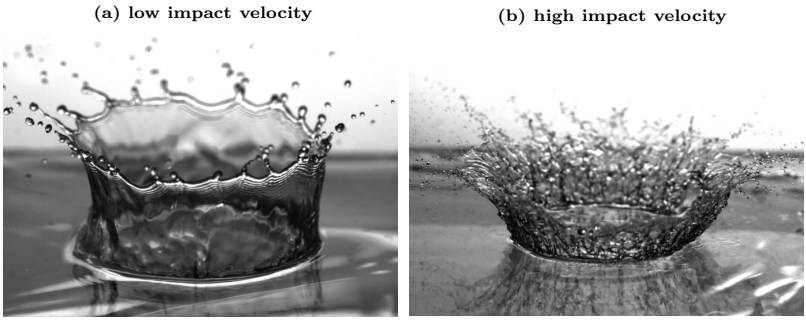

Figure 4.5: Effect of impact velocity on crown formation. (a) a water drop of $D \approx 4.2$ mm impacting at $U \approx 5$ m/s and (b) a water drop of the same size impacting at $U \approx 13$ m/s.

this thesis, as shown in figure 4.6. It is important to highlight that the undulations of this thin lamella might not be promoted by previous perturbations on the film, which are not visible in the images of figure 4.5 and not considered in the numerical simulations. One possible mechanism leading to these small but strong perturbations in the thin lamella could be related to the Rayleigh-Taylor instability, which is the result of antisymmetric disturbances in the fast-accelerating liquid sheet. This kind of instability has been assumed by Li et al. (2018) when investigating the unsteady azimuthal undulations present at the early stage of impact. The work of Thoroddsen and Sakakibara (1998) showed that undulations generated at the early stage of impact propagate within the lamella, and, as a result, the undulations can merge or split during the entire spreading process. It is reasonable to expect the same behavior for impacts on a wetted surface. The numerical simulations conducted for this thesis indicate that the surrounding gas is strongly perturbed by the crown formation at high speed. Hence, these chaotic velocity and pressure fields might accelerate the break-up process and promote the local thinning observed in the lamella, as shown in figure 4.5(b).

The effect of film thickness on splashing on a fluid at rest has been investigated by a host of authors over the last decades (Chen et al., 2017, Deegan et al., 2007, Hammond et al., 2005, Rioboo et al., 2003, Vander Wal et al., 2006b, Wang and Chen, 2000). One of the first studies elucidating the role of film thickness on splashing was presented by Gregory et al. (1959), who observed that the thinner the film, the

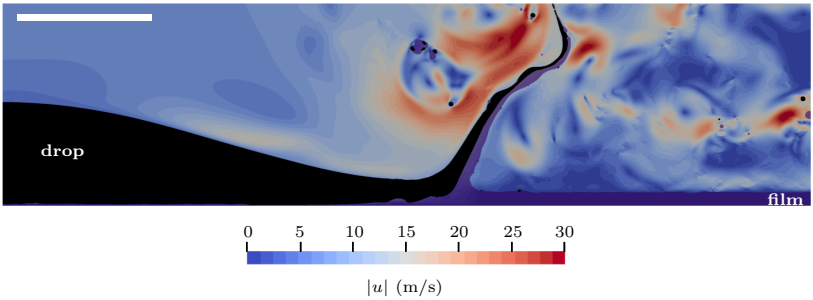

Figure 4.6: Crown formation in high-speed impacts (We=5,000) on thin moving films ($h_f = 0.1$ mm and $U_f = 1$ m/s). The simulations demonstrate the chaotic and turbulent gas flow around the crown and the strong bending of the ejected lamella at its top. Scale bar 1 mm.

higher the probability to induce splash. These results were later confirmed and quantified in the experimental work of Cossali et al. (1997). Since the outcome morphology clearly changes depending on the film thickness, Tropea and Marengo (1999) proposed to separate the impact phenomenon into four categories depending on the film/drop ratio δ: thin film $L_a/D < \delta < 3(R_a/D)^{0.16}$, liquid film $3(R_a/D)^{0.16} < \delta < 1.5$, shallow film $1.5 < \delta < 4$, and deep pool $\delta \gg 4$. Here, L_a represents the length scale of the surface roughness. The existing experimental data indicate that the thinner the liquid film, the stronger the influence of the surface properties on the crown formation. However, the majority of experimental studies only observe the morphology of the generated crown without providing a detailed quantification of the ejected droplets. Recent experiments conducted to quantify the outcome of splashing demonstrate that the film thickness has a weak effect on determining the size and velocity of the ejected secondary droplets when the dimensionless film thicknesses δ is between 0.26 and 1.29 (Li et al., 2019, Okawa et al., 2006). The study of Faßmann (2015) also reveals a similar behavior when varying the film thickness δ from 0.1 to 0.2. The results of all mentioned quantification studies lead to the conclusion that the film thickness does not notably affect the splashing outcome of a drop impacting on a liquid film ($3(R_a/D)^{0.16} < \delta < 1.5$). As this thesis concentrates on the splashing on liquid films, the findings of Li et al. (2019), Okawa et al. (2006) are adapted throughout the upcoming analysis. However, it is important to mention that if the ratio of film thickness to drop diameter changes so considerably that it leads to an

impact phenomenon of another category, it is also expected that the outcome of splashing differs notably, as shown in the reviews ofLiang and Mudawar (2017), Yarin et al. (2017).

4.3.1 Effect of film flow on high-speed impacts

The simple movement of the film layer can alter the outcome of splashing and the generation of the secondary droplets. Alghoul et al. (2011) demonstrated that the shape of the crown is asymmetric and similar to the estimated when single drops are impacting on an inclined surface (Roisman and Tropea, 2002). More recently, Gao and Li (2015) showed that by increasing the film velocity of thin films, the splashing and ejection of secondary droplets can be promoted. Using sophisticated experimental set-up, Castrejón-Pita et al. (2016) studied the impact of drops on very fast-moving liquid films and demonstrated that if the film velocity is much larger than the impact velocity $U_f > 0.2U\sqrt{Re}$, the impact never leads to splashing and the drop surfs, emits a small lamella, or coalescences. In such cases, the splashing threshold of $K_{lim} \sim 2100$ defined by Cossali et al. (1997) may change due to the inertia added by the moving liquid, as assumed by Gao and Li (2015). The movement of a liquid film on a surface can lead to different instabilities and generate waves of different amplitudes and frequencies (Ostrach and Koestel, 1965). Adebayo and Matar (2017) investigated the effect of these waves on splashing and showed that if the amplitude of the waves is relatively small (capillary waves), the outcome of splashing is similar as in the case of impacting on a flat film. However, the impact on a hump wave can change the impact outcome drastically because the film thickness considerably increases.

The experimental results of this thesis demonstrate how the simple movement of the film can drastically affect the geometry and development of the crown. The images of figure 4.7 show the deformation of the crown in high-speed impacts at different phases of impact. At the early stage $\tau < 1$, the geometry is almost symmetric regardless of the impact velocity or film thickness. The high inertia of the drop is more dominant at this stage than the film inertia; therefore, the outcome is similar to the impact on films at rest. Similar behavior was speculatively assumed by Roisman and Tropea (2002) for the deformation of the base crown, which in the theoretical model developed in a circular form. Nevertheless, when the kinetic energy of the spreading drop is dissipated by viscous effects, the moving film inertia plays a more important role, affecting the development of the crown. In such a case,

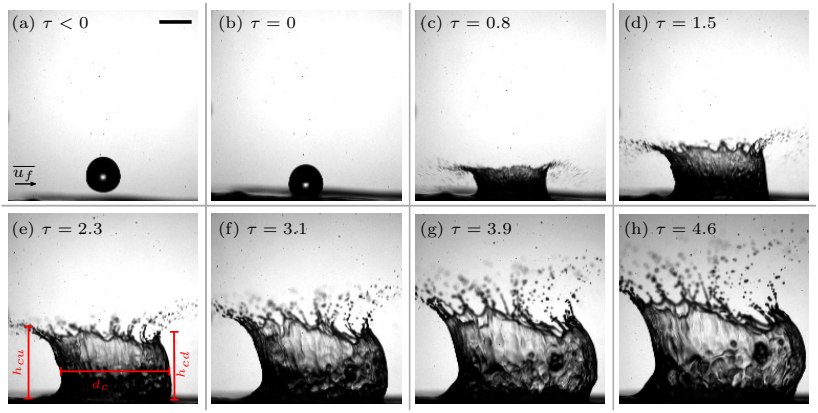

Figure 4.7: Evolution of a high-speed drop impacting on a thin moving film. Impact conditions: $We = 2,281$, $u^* = 0.15$, and $\delta = 0.13$. Standard deviation of impact time τ of 0.15 and scale bar of 3 mm. Adapted from Burzynski and Bansmer (2018a).

the upstream side of the crown is strongly influenced by the film velocity because the spreading velocity and the film develop in opposite directions. On the downstream side, the crown emerges more in normal direction to the film. At later stages of the splashing $2 < \tau < 5$, the crown is no longer perpendicular to the base, and the curvature of both crown sides has increased. This occurs because the inertial forces from the moving film flow become stronger. The curvature variation in the upstream side is almost negligible but still noticeable, while the curvature of the downstream side varies drastically, as shown in figure 4.7(h). Once the crown is approaching the maximal height $\tau > 5$, almost no liquid flows into the lamella, and the curvature on the downstream side decreases gradually until the crown becomes perpendicular to the surface. This final symmetrical development over time agrees with the observations made by Alghoul et al. (2011) on moving pools at low impact velocities $We < 460$.

It is demonstrated here that crown formation depends on the film velocity since it affects the amount of liquid moving into the crown, as shown in figure 4.8. When the inertia of the film is much smaller than 5% of the drop inertia ($u^* < 0.05$), a symmetric shape in the azimuthal direction is formed, which is similar to the observed shape when drops impact on films at rest. Hence, an increase in the film velocity reduces the ratio between both inertial forces, and the film

(a) $u^* \approx 5\%$ (b) $u^* \approx 15\%$ (c) $u^* \approx 30\%$

Figure 4.8: Effects of film velocity on the crown formation at $We = 2,281$ and $\tau = 4.6$. The crown remains symmetric at $u^* < 5\%$, but it starts to bend by increasing the flow velocity. Film flows from left to right; scale bar 3 mm. Adapted from Burzynski and Bansmer (2018a)

flow influences the crown formation, generating a curved crown. This effect becomes more noticeable when the film velocity is greater than 20% of the impact velocity. The translation of the entire crown in the flow downstream direction has also been observed if the film velocity is very high. As mentioned above, if the mean film velocity is further increased $U_f > 0.2U\sqrt{Re}$, the drop surfs, emits a small lamella, or coalescences (Castrejón-Pita et al., 2016).

> The film movement can drastically affect the crown formation for high impact velocities; however, the lamella develops axisymmetrically when the film velocity is $< 0.05U$.

4.3.2 Crown geometry for high-speed impacts

Part of the text described in this section has already been published in Burzynski and Bansmer (2018a).

The crown geometry is quantified by measuring the evolution of its diameter and height over time. The diameter d_c is evaluated approximately at the middle of the crown, while the crown height h_c is obtained by taking the average between the upstream h_{cu} and downstream side h_{cd}, as shown in figure 4.7(e). These values are made dimensionless using the drop diameter D, such that $D_c = d_c/D$ and $H_c = h_c/D$. This kind of characterization is also very important to validate numerical simulations for engineering applications (Lee et al., 2011, Liang et al., 2014b). Figure 4.9(a) shows the crown diameter evolution at different

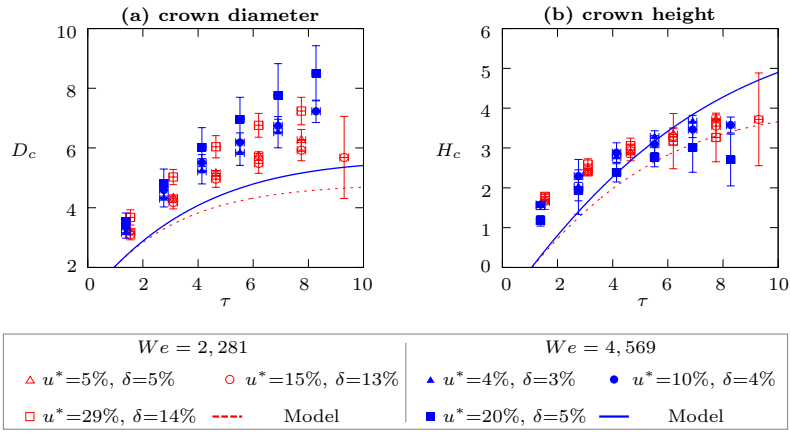

Figure 4.9: Time evolution of the crown geometry. (a) shows that the crown diameter increases with the film velocity and impact velocity. (b) shows that the crown height seems to be weakly dependent on the film and impact conditions. Adapted from Burzynski and Bansmer (2018a)

impact and film velocities. During the early stage of impact $\tau < 2$, the diameter developed similarly in all cases regardless of the impact and film velocity. However, at later stages of impact $\tau > 5$, the crown diameter becomes larger with increasing Weber numbers. This can be explained by the higher inertial forces of the drops, which intensify the expansion of the crown, leading to a larger diameter. It can also be observed that the influence of the moving film increases with the impact velocity; however, in this experimental set-up, a simultaneous increase in the film velocity leads to an inevitable increment in the film thickness.

The analysis of the results obtained for the time evolution of the crown height shows that this quantity depends on the impact and film velocity, as shown in figure 4.9(b),. For example, when the drops impact at $We = 2,281$, an increase in the film velocity results in a smaller crown height on the downstream side due to the crown curvature, as shown in figure 4.8. Even though this effect is notable, the mean height can be assumed to be constant regardless of the film velocity. This phenomenon can be observed until $\tau \approx 6$; thereafter, the formed crown for the lowest film velocity breaks up and, as a result, the crown height starts to decrease. This indicates that the moving film supplies the

crown with more liquid in the upstream direction, delaying the break-up process. It can be concluded that the higher the film velocity and thickness, the longer it takes to start the break-up process.

> The crown height seems to be weakly dependent of the impact velocity, while the crown diameter increases notably with the impact velocity.

Modeling the crown geometry

The theory of Yarin and Weiss (1995) allows modeling the crown formation and the related geometrical quantities. Roisman and Tropea (2002) generalized this theory for impacts from different angles and provided an analytical solution for the crown shape in the case of high-speed impacts ($We \gg 1$ and $Re \gg 1$), where the surface tension and viscosity effects can be neglected. The radius vector $\boldsymbol{X}_J(t_B, t)$ defining the crown shape as a function of the elapsed time t is in this approximation expressed as

$$\begin{aligned}\boldsymbol{X}_J(t_B,t) =& \beta_{RT}(t_B+\tau_{RT})^{1/2} \\ &\times\left[1+\frac{\eta_{RT}}{(t_B+\tau_{RT})[\eta_{RT}+\delta(t_B+\tau_{RT})^2]}(t-t_B)\right]\boldsymbol{e}_r \\ &+\beta_{RT}(t_B+\tau_{RT})^{1/2}\frac{\eta_{RT}^{1/2}\delta^{1/2}}{\eta_{RT}+\delta(t_B+\tau_{RT})^2}(t-t_B)\boldsymbol{e}_z \\ &-\frac{1}{2Fr}(t-t_B)\boldsymbol{e}_z,\end{aligned} \tag{4.5}$$

where t_B is the time of ejection from the surface, δ is the dimensionless film thickness, $Fr = U^2/(gD)$ is the Froude number, and β_{RT}, η_{RT}, and τ_{RT} are dimensionless constants depending on the impact conditions Re, We, and δ. Roisman and Tropea (2002) argued that by neglecting the momentum loss during the drop deformation prior to the impact and taking into account the mass balance of the drop, the constant parameters can be expressed as

$$\beta_{RT} = \left(\frac{3\delta}{2}\right)^{-1/4}, \tau_{RT} = \frac{1}{\sqrt{24\delta}}, \eta_{RT} = \frac{1}{24}. \tag{4.6}$$

To estimate the position of the rim and the crown shape within this theory, it is also necessary to calculate t_B and t_R, where the latter

corresponds to the time at which the discontinuity reaches the rim. The solution of the system of equations that includes both times is extensive and therefore not shown here. For further information, the reader is referred to section 3 of the study presented in Roisman and Tropea (2002), where a detailed description of how these quantities are obtained is provided. Finally, the dimensionless height of the crown is the calculated as $Z_R = \boldsymbol{X}_J(t_R, t)\boldsymbol{e}_z$, and the dimensionless diameter of the crown as $\boldsymbol{X}_J(t)\boldsymbol{e}_r$. The review of Liang and Mudawar (2017) shows that the existence of a kinematic discontinuity has been validated using numerical simulations and experiments in multiple studies.

The experimental investigation of Cossali et al. (2004) demonstrated that the model predicts the crown height for low impact velocities and thin films $\delta = 0.29$ well. Additionally, the authors showed that the crown height is weakly dependent on the film thickness, which is also confirmed by our experiments. On the contrary, the initial film thickness plays an important role in the theoretical model when predicting crown geometry. In the model, the film thickness is used as a constant length scale for the spreading liquid sheet. This scaling subsequently leads to a wrong estimation of the crown geometry for thicker films. The comparison of the model with the experimental results at high impact velocity $We = 4,569$ suggests that the crown height is underestimated at the early phase ($\tau < 5$) but overestimated at later time points, about 40% at $We = 4,569$ and $u^* = 0.04$. However, for $We = 2,281$, the model underestimates the crown height for longer impact times, as shown in figure 4.9(b). It is worth mentioning that the break-up processes always started first on the downstream side of the crown, where no fluid film flow stimulates the crown formation. Hence, at very high impact velocities the crown breaks up earlier, which results in even smaller dimensionless crown heights compared to the case of low Weber numbers.

The experimental results demonstrate that the diameter of the crown seems to be more sensitive to changes in the impact velocity than the crown height. The increase in crown diameter with the impact velocity is fairly predicted by the model; however, it tends to underestimate the measured diameter for all the studied Weber numbers. The difference between the measured diameters and those predicted by the model at $\tau > 7$ and for $We = 4,569$ was about 44%; however, the prediction at lower Weber numbers is more accurate. Another reason for the inaccuracy of the model is probably linked with neglecting the surface tension and viscosity for the entire crown formation; this assumption is only true at the early stage of impact when the inertial forces domi-

nate. When the droplet spreads across the film, the viscous dissipation between the drop and film results in the reduction of the flow inertia. Especially at the last stages of impact, when the crown reaches its maximum, the velocity of the lamella becomes 0, and surface tension and viscosity dominate the dynamics.

The model presented by Yarin and Weiss (1995) and adapted in Roisman and Tropea (2002) makes a fair prediction of the crown diameter and height for high-speed impacts on thin films.

4.4 The ejected secondary droplets

The ejection of secondary droplets is caused by periodic instabilities acting on the free rim. If the rim becomes unstable, it leads to the generation of cusps with finger-like ligaments, which then rupture into secondary droplets, as shown in figure 4.10. This phenomenon starts at the early stage of impact with the ejection of the ejecta sheet and continues until the receding phase. Different instability mechanism has been proposed to describe the emergence of the ligaments; up to date, there is no consensus on the underlying mechanism of splashing (Roisman, 2010, Villermaux, 2007, Yarin, 2006, Yarin et al., 2017).

Some theories attribute the rim instability to the Rayleigh-Plateau instability, to the Rayleigh-Taylor instability, or to a combination of longitudinal and azimuthal instabilities. The most common instability used to describe the break-up is the Rayleigh-Plateau instability, which is understood as the capillary instability of a free cylindrical jet (Villermaux, 2007). However, Roisman (2010) argued that since the perturbations in the Rayleigh-Plateau instability are always relative to the rim centerline of a straight cylindrical jet, this instability alone cannot be responsible for the splashing. This argument is particularly true when analyzing the crown formation of high-speed drops, where the lamella bends and deforms during its entire evolution. As demonstrated in figures 4.5 and 4.10, the ejected crown and the finger-like jets are not straight.

Yarin and Weiss (1995) showed that the rim-bending disturbances become non-linear at the final stage of impact, leading to the formation of cusps and subsequently ligaments. Roisman (2010) additionally demonstrated that the rim acceleration notably influences the growth rate of

Figure 4.10: Close-up of the break-up process at $We \approx 11,500$.

these rim-bending disturbances. This suggests that the Rayleigh-Taylor instabilities can be indeed one of the most dominant instabilities in the rim, as observed in the prompt splash regime on dry surfaces. Nevertheless, Agbaglah et al. (2013) and Agbaglah and Deegan (2014) have suggested that the rim is susceptible to both the Rayleigh-Plateau and the Rayleigh-Taylor instabilities depending on the time at which this mechanism occurs. It is reasonable to expect that different mechanisms are acting at different stages of this complex splashing phenomenon.

4.4.1 Size of the secondary droplets

The size of the ejected secondary droplets provides essential information about the dynamics responsible for the atomization process (Villermaux and Bossa, 2011). In general, the splashing of liquid drops leads to the generation of broad size distributions. This poly-dispersity of the size of ejected secondary droplets during the high-speed impact is shown in figure 4.11(a). In the case of the lowest impact velocity studied here ($We \approx 2,400$), the poly-dispersity of the size can be clearly observed. This distribution has two peaks. The first peak is caused by the finest secondary droplets ejected at the early stage of impact, while the second peak is caused by the largest secondary droplets. For moderate impact velocities, the standard deviation of the distribution is relatively large, and the arithmetic mean diameter is around 3% of the impacting drop diameter. Once the impact velocity increases, the standard deviation decreases together with the mean droplet diameter. The cause of this shifting in the mean droplet diameter can be ex-

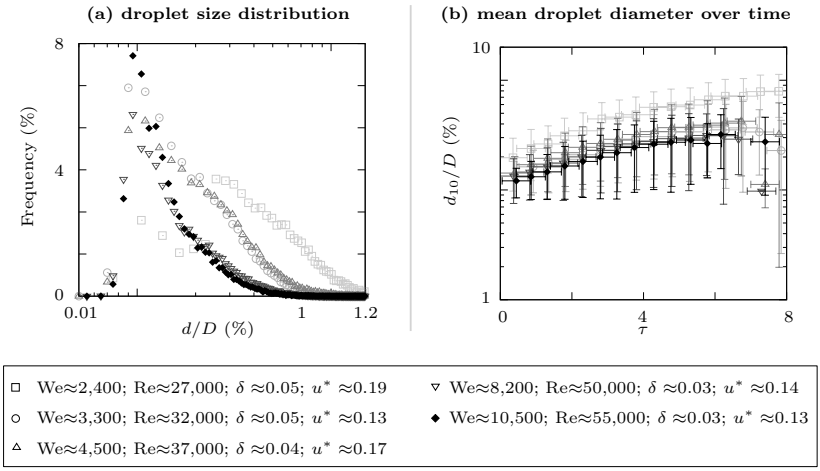

Figure 4.11: The size of the secondary droplets. (a) shows the size distribution for different impact velocities. (b) shows the evolution of the arithmetic mean diameter over time.

plained by the thinning of the lamella with increasing impact velocity (Roisman et al., 2006). The high-resolution images demonstrate that an increase in impact velocity leads to an increase in the perturbations in the lamella and rim. As the crown expands, the very strong perturbations promote the pinch-off and merging of the jets, producing a plethora of secondary droplet sizes.

Analogously to the observations made from the impact on dry surfaces, it is reasonable to expect that the size of the secondary droplets is strongly correlated to the crown thickness since the crown is the origin of the droplets. This idea has been corroborated by many authors when studying the impact on dry, moving, or wetted surfaces (Bird et al., 2009, de Ruiter et al., 2010, Roisman et al., 2006, Thoroddsen et al., 2012a). In the case of the spray impact, Roisman et al. (2006) demonstrated that the thickness of the crown can be scaled using the boundary layer thickness as $h_\mu \sim DRe^{-1/2}$. Therefore, the higher the Reynolds number, the thinner the crown and the smaller the ejected secondary droplets, as demonstrated in figure 4.11(b).

The measured probability density of the secondary droplets is well described using a log-normal distribution, which indicates the stochastically independent process during the generation of droplets. The log-

normal distribution of droplet size has been used previously to characterize the ejected droplets in experiments (Berthoumieu and Djean, 2017, Faßmann, 2015, Mundo et al., 1995, Wang and Bourouiba, 2018, Yarin and Weiss, 1995) and numerical simulations (Cimpeanu and Papageorgiou, 2018, Xavier et al., 2019). Wang and Bourouiba (2018) analyzed the origin of the disperse size distribution and concluded that the secondary droplets can be ejected in the form of end-pinching, ligament-merging, and satellite droplets. Accordingly, the drop size distribution obtained during the fragmentation of an unsteady free sheet is the result of 90% end-pinching and ligament-merging with only 10% from satellite droplets. It is very likely that this is also the case in high-speed drop impacts on thin films; however, further experimental and numerical studies are needed to confirm this assumption.

Some relevant correlations to the lamella can be made by analyzing the time evolution of the arithmetic mean diameter of the ejected droplets, which is shown in figure 4.11(b). The results indicate that the lamella thickness and, therefore, the arithmetic mean diameter scales rather well with the thickness of the boundary layer h_μ in the case of high-speed drops impacting on thin moving films. In this case, $h_\mu \sim DRe^{-1/2}$ represents the viscous layer thickness at the thin film surface, as porposed by Tropea and Roisman (2000), Yarin and Weiss (1995) and illustrated in figure 3.12. The mean droplet size diameter is estimated from the existing experimental data to be scaled as $d_{10} \approx 5DRe^{-1/2}$. The results corroborate that the higher the impact velocity, the smaller the ejected secondary droplets. Moreover, this result demonstrates the different physical mechanisms involved during splashing on dry, wetted, or spray impacts. The impact on dry surfaces generates droplet sizes almost identical to the boundary layer thickness $d_{10} \approx 1.5DRe^{-1/2}$, while droplets generated during the spray impact are much larger than the ones observed in this study $d_{10} > 10DRe^{-1/2}$ (Roisman et al., 2006). This indicates that the different splashing phenomena have to be described separately. It can also be concluded from figure 4.11(b) that the longer the impact time τ, the larger the secondary droplets ejected. This is explained by the thickening of the crown caused by the viscous forces, which become more dominant at the latter stages of impact. As a consequence of viscous forces, the lamella slows down, promoting the agglomeration of liquid at the rim.

The arithmetic mean diameters of the secondary droplets can be scaled by the boundary layer thickness.

4.4.2 Velocity of the secondary droplets

The velocity of the secondary droplets is strongly related to the ejection time. Following the analogy of the high-speed impacts on dry surfaces, it is reasonable to expect that small but fast secondary droplets are ejected at the early stage of impact. Over time, the ejected droplets become larger and their velocity decreases. This is shown in figure 4.12(a), where the velocity of the ejected droplets is plotted as a function of their size. The colors indicate the time at which they were captured with the recording system. The results demonstrate the plethora of droplets sizes ejected and the different velocities during the entire splashing process. In accordance with the measurements on a dry surface and the analysis provided above, the velocity of the droplets is higher than the impact velocity at the moment of impact, but it decreases with time. It is assumed that the secondary droplets can be ejected at velocities higher than $3U$; however, they were not measured in this study since only droplets with a diameter larger than $d > 30$ μm could be evaluated. Thus, the small ejected droplets are excluded from this analysis.

The time evolution of the droplet mean velocity, as shown in figure 4.12, indicates that the drop velocity behaves like $\overline{u}/U \sim 1/\tau$. This

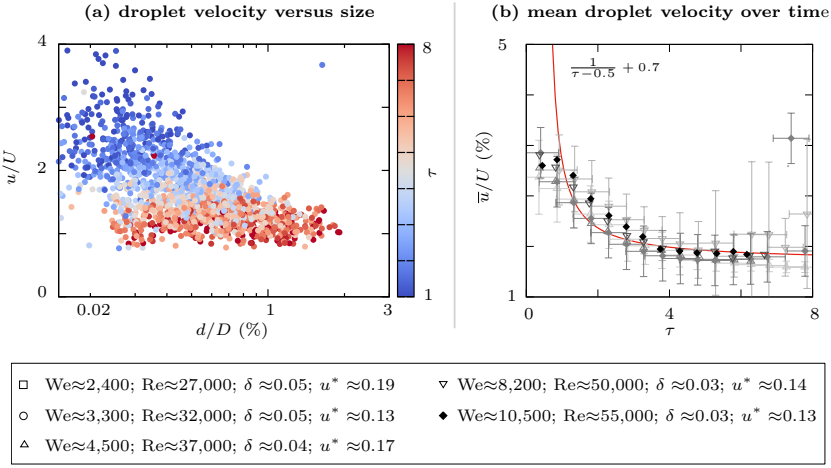

Figure 4.12: The magnitude velocity of the secondary droplets. (a) shows the velocity of each ejected droplet at $We \approx 2.300$, $Re \approx 27.000$, $\delta \approx 0.05$, and $u^* \approx 0.19$. (b) shows the time evolution of the arithmetic mean velocity, which behaves like $\sim \tau^{-1}$.

behavior has been proposed multiple times and seems to provide an acceptable prediction of the secondary droplet velocities (Riboux and Gordillo, 2014, Thoroddsen et al., 2012a, Yarin and Weiss, 1995). The difference between the impact velocities measured in this work is explained by the strong fluctuations in the crown. Using the theories of Yarin and Weiss (1995) or Howison et al. (2005), it is possible to some extent predict the ejected crown velocity at the base. However, those theories have some limitations because they are suited to provide estimations about the root of the crown, while the nonlinear movement of the ejected crown at high velocity cannot be estimated. Although the mean velocity of the droplets can be roughly estimated using the simple empirical relation $\overline{u}/D \sim (\tau - 0.5)^{-1} + 0.7$, the strong fluctuations of this lamella made the modelling of high-speed drops on wetted surfaces very challenging.

4.4.3 Ejected volume during crown expansion

The total volume ejected during the crown formation of high-speed impacts is shown in figure 4.13. The volume is plotted as a function of the splashing parameter K proposed by Cossali et al. (1997) for impacts on wetted surfaces. This K-Parameter balances the most relevant forces, such as surface tension, viscosity, and inertia. As mentioned above, the use of this parameter is valid for high-speed impacts on thin films since the existing experimental data indicate that the surrounding gas does not affect the crown formation and the generation of secondary droplets (Guo et al., 2016, Liang et al., 2014a, Zhang et al., 2012b).

Figure 4.13 also demonstrates that the higher the inertial forces prior impact, the larger the amount and volume of ejected secondary droplets. However, the volume ejected during the break-up of the ejecta sheet is not taken into consideration due to the small amount ejected in this phase ($d < 30$ μm), which is negligible when comparing it with the largest droplets generated during the crown formation or delayed break-up. When this delayed break-up occurs, the total amount of volume during the splashing changes notably. Such a scenario is described in the following section, where the crown collapse through two different break-up mechanisms is explained. It is demonstrated in this thesis that if the crown completely atomizes, the ejected volume can exceed the volume of the initial drop. This means that the amount of liquid in the film is reduced during the splashing phenomena.

To verify this assumption, the composition of the lamella was studied using numerical simulations. The results demonstrate that the volume

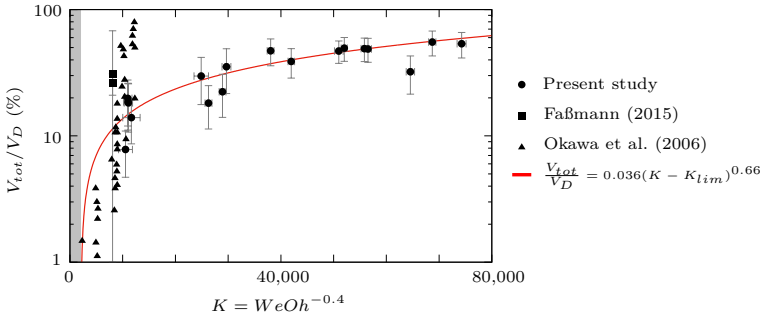

Figure 4.13: Ejected volume during the crown expansion. The experimental data available show the relation between the total ejected volume V_{tot}/V_D and the splashing parameter K. The non-splashing area is represented as a grey box, where the limit is given as $K_{lim} = 2100$.

of the crown at the latter stages of splashing consists mainly of liquid from the film and not from the drop. Nevertheless, the use of the empirical correlation based on the K-parameter reads

$$\frac{V_{tot}}{V_D} = 0.036(K - K_{lim})^{0.66}, \tag{4.7}$$

where $K = WeOh^{0.4}$. This expression provides a fair estimation of the volume ejected during the crown formation on thin films. It has to be highlighted that this empirical correlation is valid only for drop impacts on thin films when the film thickness δ is in a range between 0.1 and 1.29. The results of this study and the work of Li et al. (2019), Okawa et al. (2006) demonstrate that the film thickness has a weak effect on the total volume ejected in this range. For this reason, the film thickness can be neglected from equation 4.7. When a drop impacts on a very thin film $\delta < 0.1$, shallow films $1.5 < \delta < 4$, or a pool $\delta > 4$, the outcome differs notably, as shown in (Liang and Mudawar, 2017, Yarin et al., 2017). Nevertheless, equation 4.7 describes rather well the volume ejected at low, moderate, and high impact velocities on thin liquid films, which can be easily used to predict the total ejected volume or the deposited volume in several technical applications, such as aircraft inflight icing or vehicle soiling problems.

The volume ejected in the form of secondary droplets during the crown formation can be estimated farily well using the K-Parameter.

4.5 Crown collapse and delayed splash

Part of the text described in this section has already been published in Burzynski and Bansmer (2018a).

Once the spreading crown reaches its maximal height $U_l = 0$, it falls slowly down until the entire crown merges with the liquid film. This process is strongly dependent on the film thickness; for example, the impact on a pool generates a long jet (Worthington jet), which can collapse and generate additional secondary droplets. As this kind of phenomenon does not occur when high-speed drops impact on thin films, it is not covered in this thesis. Further details related to the Worthington jet can be found in (Gekle and Gordillo, 2010, Michon et al., 2017, Roisman et al., 2008). During the receding of the crown and before it merges with the thin film, a few large droplets are usually generated. This delayed splash results from the thin, unstable crown in retraction breaking up due to capillarity, forming large ligaments and, subsequently, multiple droplets (Vander Wal et al., 2006a, Villermaux, 2007). This ligament formation and the break-up are promoted by the transverse rim instabilities, which form the jets at the rim during the deceleration of the crown (Roisman et al., 2006).

The high-speed impact on very thin films leads to one particularly interesting phenomenon, which is characterized by a complete break-up of the crown before it can merge with the film. In such a case, the break-up is induced by two different mechanisms: hole formation and lamella separation from the crown base, as shown in figure 4.14. *The holes* are formed typically in the middle of the crown and spread throughout the lamella until the crown rim or base is reached. A similar break-up process has been observed in thin soap films after puncturing (Culick, 1960, Taylor, 1959) and in the splashing of droplets using a film of lower viscosity and surface tension than the primary drop (Aljedaani et al., 2018, Murphy et al., 2015, Thoroddsen et al., 2006). When liquids with different viscosity and surface tension collide, a gradient of surface tension leads to strong convective effects along the fluid-fluid interface. The liquid with the lower surface is stretched out, reducing the thickness locally; subsequently, the film breaks up forming a hole.

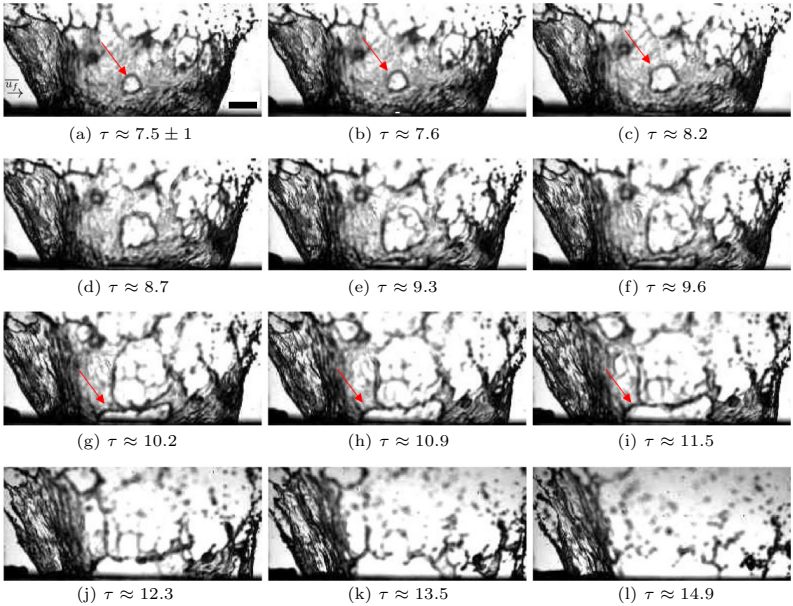

Figure 4.14: Crown break-up process at high Weber numbers ($We = 4,569$, $\delta \approx 0.03$, and $u^* = 0.04$). The film flows from left to right. The arrow shows the rims generated in the break-up phase for the hole formation and the separation from the base. Reprinted from Burzynski and Bansmer (2018a).

Marston et al. (2016) also observed hole formation near the crown top by using a solid sphere as an impact object onto deep pools at high Weber numbers. They attributed the hole formation due to the presence of air bubbles in the liquid, where the liquid sheet surrounding the bubble can be extremely thin. The hole formation in such kind of thin water films has been studied for decades and is relatively well understood; however, the origin of ruptures of thicker films ($1 < \delta < 100$ μm) is still not clear. Recently, Néel and Villermaux (2018) attributed the spontaneous rupture of thick water films to considerable chemical and thermal inhomogeneities caused by any agent diluted in the liquid. However, the experiments presented here demonstrate that a drop or film without chemical or surface tension differences can produce holes. This is particularly true when the impact velocity is very high and the thickness small. Discarding any chemical and thermal inhomogeneity,

the only reasonable possibilities remaining for the hole formation are very strong fluctuations in the lamella (Villermaux and Clanet, 2002), the collision of small secondary drops on the lamella (Thoroddsen et al., 2006), or rupturing of small bubbles in the film (Spiel, 1998).

To determine the mechanism responsible for the hole formation at high impact velocity, the break-up phenomenon was observed in detail using the high-resolution camera. Since this camera captured only two images for each impact, the elapsed time in this specific experimental set-up was calculated measuring the diameter and height of the observed crown. The uncertainty obtained by the calculation of the elapsed time from the high-speed camera also propagates into this analysis. Figure 4.15 shows the high-resolution image of the forming hole at $\tau \approx 7.5 \pm 0.5$, demonstrating that it is surrounded by capillary waves of different wavelengths and amplitudes. Due to the fact that the holes appeared at different azimuthal positions, the images were corrected to eliminate the perspective distortion for the holes located downstream and upstream from the crown center. The correction was made by defining the crown arc ($s = R \cdot \arcsin(x/R)$) as the new and transformed horizontal axis, where R is the crown radius. This transformation unfolds the cylindrical shape of the crown into a 2D SY-plane. The intensity values of each pixel in the transformed plane were obtained using a shape-preserving piecewise cubic interpolation. The light intensity of those images was further analyzed in a constant vertical and horizontal direction, y_0 and x_0 or s_0, respectively, as shown in figure 4.15.

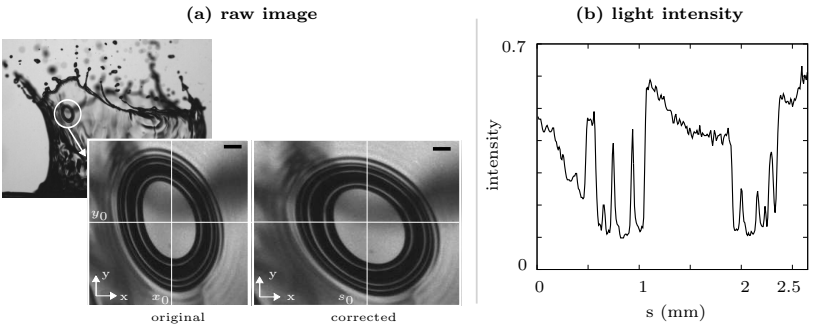

Figure 4.15: High-resolution image of the hole formation in the crown. The first zoomed image shows the original crop, while the second shows the corrected image. Reprinted from Burzynski and Bansmer (2018a).

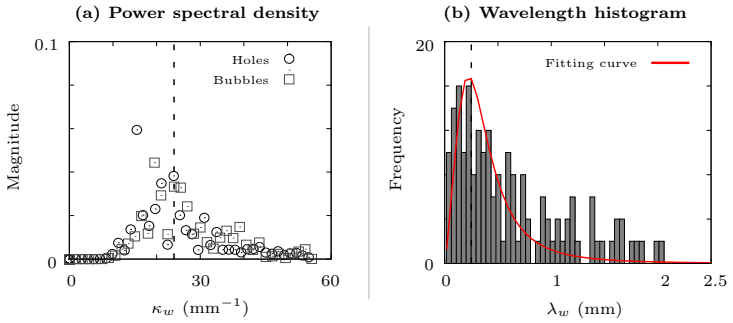

Figure 4.16: Spectral analysis of the holes and bubbles observed in the lamella during the break-up process. (a) shows the power spectral density of the DFT. (b) shows the histogram of wavelength with a fitting curve. Adapted from Burzynski and Bansmer (2018a).

After the spatial correction, the light intensity signals for the holes formed in the lamella were analyzed using a discrete Fourier transform (DFT). The DFT was performed to obtain the oscillatory components of the capillary waves around the holes. Figure 4.16(a) shows the spectral density of the capillary waves as a function of the wave number. The wavelengths can be estimated by setting the intensity threshold to a value that corresponded to 70% of the brightest pixel signal and measuring the lengths between the detected shadows. The results of this approach are shown in figure 4.16(b). It has to be mentioned that the location of the shadows varied depending on the setting of the intensity threshold. In the presented case, the 70% threshold led to uncertainty of around 6 pixels (54 μm). The results of analyzing the capillary waves around the holes show that the spectral density and the wavelength histogram have a local maximum at $k_w \approx 25$ mm^{-1} and $\lambda_w \approx 250$ μm. These values are discussed in the following section and are used to estimate the thickness of the lamella at the moment of the break-up.

The conducted experiments show that in some occasions either the crown is filled with some small bubbles or small secondary droplets fly through the impacting area. Therefore, it is challenging to establish whether the secondary droplets or small bubbles are responsible for the hole formation. Nevertheless, the high-resolution images often reveal the bursting of the small bubbles after they reach the middle of the crown. These bubbles have an initial diameter of approximately

100 μm, and their bursting caused waves expanding over the lamella. By analyzing the wave dispersion of the bubbles using the same methods as with the holes, it can be demonstrated that the wave numbers in the power spectral density correlate with each other, as shown in figure 4.16(a). This fact leads to the conclusion that if the lamella is locally thin enough, it is the bursting of these bubbles that produces the holes. This local thinning of the crown is predicted by the numerical simulations (see figure 4.6) and observed in the high-resolution images (see figure 4.10). In agreement with Marston et al. (2016), it seems that the thinning of the crown and the small bubbles are indeed responsible for the hole formation. Such bubbles can be formed at the initial stage of impact (Thoroddsen et al., 2012b) or are already present in the fluid prior to the impact. However, the simulations indicate that the bubbles formed during entrapment are very small and are not transported to the crown, as shown in figure 4.17.

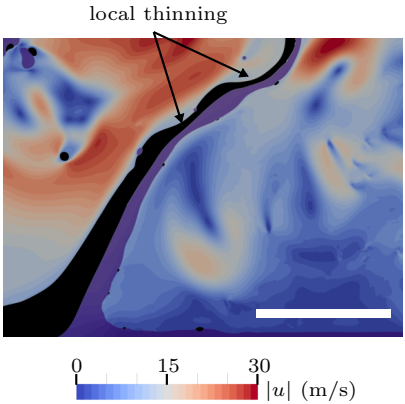

Figure 4.17: Undulations and thinning of the crown when drops impact at high velocity. Scale bar 500 μm.

The lamella separation is observed during the break-up process, starting from the crown base. A similar process has been reported in Kittel et al. (2018), Wang and Chen (2000) for droplet impact on thin film layers and at low Weber and Reynolds numbers. Even though these different break-up processes (holes and lamella separation) have been observed separately and are the results of different setups, this experimental study demonstrates that both mechanisms can coexist in the high-speed splashing on thin films. In the most common scenario, the separation from the crown base occurs first on the downstream side but never upstream; however, the holes are formed all around the crown. Considering this fact, it is clear that the moving film affects the instability of the crown, delaying the lamella separation upstream due to the constant mass supply. This process is observed in all experiments, but the separation occurs even earlier when the film velocity and thickness are low.

The physical explanation of the lamella separation is the surface tension, which does not stabilize the thinner film for a longer time, and the rupture or separation is more probable. Finally, the formed holes expand radially until the rim either reaches the crown rim or the rim formed by the lamella separation at the crown. Once these rims merge together, they form large ligaments that atomize later into secondary droplets (Villermaux and Bossa, 2011). It is important to mention that the size, velocity, and volume of these ejected droplets differ from the secondary droplets ejected during the crown formation, as shown in section 4.4.

The hole formation and lamella separation always occur at the last stage of splashing, usually when the crown has reached its maximal expansion. For film velocities lower than 5% of the impact velocity, the hole formation starts at $\tau \approx 7 \pm 0.5$, while the separation of the base begins at $\tau \approx 8 \pm 0.5$. The hole formation and the separation time is affected by the film velocity, thereby retarding the break-up process when the film velocity is increased. For film velocities higher than 10% of the impact velocity, the hole formation and the separation of the base start at $\tau \approx 8 \pm 0.5$ and $\tau \approx 9 \pm 0.5$, respectively.

The expanding crown formed during high-speed drop impacts may completely destroy itself due to the hole formation and lamella separation from the crown base.

Crown thickness

The presence of the expanding holes can be used to calculate the lamella thickness during splashing. The thickness is obtained by rewriting the Taylor-Culick equation (Culick, 1960, Taylor, 1959) for wave velocity as follows:

$$h_{ct} = \frac{2\sigma}{\rho_l U_{hole}^2}, \tag{4.8}$$

where U_{hole} is the expansion velocity of the holes. This expression balances the inertial forces of the rim $\sim h_{ct} U_{hole}^2$ and the surface tension σ acting on both sides of the sheet. Several numerical and experimental studies have demonstrated that this formulation describes very well the dynamics of a receding liquid film (Clanet et al., 2004, Eggers et al., 2010, Josserand and Thoroddsen, 2016, Josserand and Zaleski, 2003, Roisman, 2009).

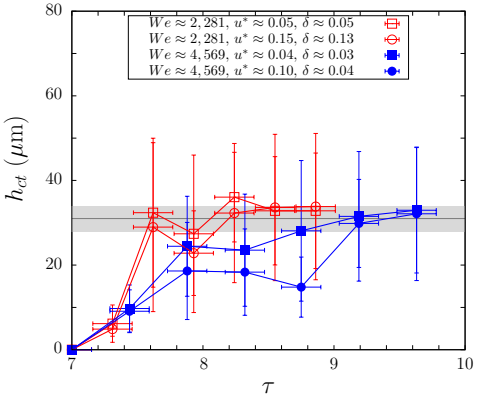

Figure 4.18: Lamella thickness as a function of τ. The holes formed first at $\tau = 7 \pm 0.5$ regardless of the experimental set-up. A total of 25 images for each case were used to calculate the lamella thickness. Reprinted from Burzynski and Bansmer (2018a).

The results of applying the equation 4.8 for the observed holes are shown in figure 4.18, where the lamella thickness after the break-up process is represented as a function of time. Interestingly, the thickness of the crown seems to be weakly dependent on the impact velocity and equals to $h_{ct} = 31 \pm 3$ μm in all experiments conducted. The time evolution also shows that the thickness increased up to $\tau \approx 7.6$ and then remained relatively constant when the drops impacted at $We \approx 2,281$. However, at higher Weber numbers, the thickness varied notably depending on the film velocity. The total number of videos used for the thickness calculation was only 25 due to the challenging task of capturing one of both lamella sides using a small depth of field of 2 mm. This is necessary to obtain a sharp image of the lamella without any intensity interference from its other side.

Since only a few images of the lamella with holes in it are available, another approach is needed to validate the lamella thickness estimated using the Taylor-Culick equation. Prévost and Gallez (1986) proposed a nonlinear theory to describe the variation of the film thickness, including the van der Waals forces acting on a thin liquid film. They demonstrated that the hydrodynamic nonlinearities accelerate the rupture process. This occurs because the attracting forces increase during the local thinning of the film. The growth rates of the disturbances in

the film are estimated as a function of the wave number as follows:

$$h_{ct} = \frac{\lambda_w k_{w,max}}{2\pi}, \tag{4.9}$$

where $k_{w,max} = 0.7$ is the dimensionless wave number corresponding to the fastest rate of growth of the disturbances and λ the related wavelength. As shown in figure 4.15(b), the most common wavelength measured around the holes is of 250 ± 50 μm. Using this information in the nonlinear theory, a lamella thickness of $h_{ct} \approx 28 \pm 6$ μm is estimated. The results are in excellent agreement with estimation made by using the Taylor-Culick equation. It is worth mentioning that the action of van der Waals forces, as considered in the work of Prévost and Gallez (1986), act on a molecular level when the film is only a few nanometers thick. This indicates that external perturbations have to be involved in order to induce the rupture in the liquid film, but once the lamella is a few nanometers thick, the nonlinear disturbances accelerate this process. It is reasonable to consider the small bubbles observed in the lamella or the secondary droplets that might collide with the thin film sheet as an external perturbation.

> The crown thickness at the moment of break-up seems to be weak dependent of the impact conditions.

Ejected volume during delayed splash

Knowing the thickness and the external geometry of the crown, it is possible to estimate its volume. This crow volume transforms into secondary droplets in the case of complete atomization in the delayed splashing phase. Although the crown shape changes over time and along the vertical axis, it develops axisymmetrically at the final stage of the impact and at very low film velocities. By roughly assuming the crown geometry as a hollow cylinder at the moment of complete atomization, the dimensionless volume of the crown can be expressed as

$$\frac{V_c}{V_D} = 3H_c \left(2D_c h^*_{ct} - (h^*_{ct})^2\right). \tag{4.10}$$

The use of this formulation indicates that the volume ejected in figure 4.14, where the geometry of the crown is described with $D_c \approx 7$, $H_c \approx 3.5$, and $h^*_{ct} = h_{ct}/D \approx 0.01$. The spreading diameter of the

crown is of approximately 1.46 times the initial drop diameter. Figure 4.19 illustrates the results of using the equation 4.10 to estimate the ejected volume during the delayed splash. It is remarkable to observe from this figure that the amount of liquid ejected in the specific case of complete atomization is much larger than the initial drop volume. However, the numerical simulations presented by Josserand et al. (2016), Thoraval et al. (2012) and those performed in this study indicate that the amount of liquid in the crown consists primarily of liquid from the film, as shown in figure 4.17. These results have been confirmed by the experiments conducted by Kittel (2019) using a dyed drop and a color high-speed camera.

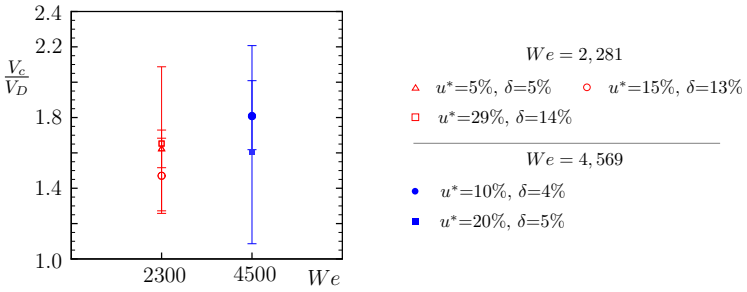

Figure 4.19: Estimated ejected volume during the delayed splashing regime as a function of the Weber number. The diagram shows the results of using equation 4.10 for the conducted experiments.

The total ejected volume during splashing on thin films consists of the ejected volume in the form of secondary droplets during the crown formation and of the ejected volume during the delayed splash caused by the entire atomization of the crown. To estimate this total ejected volume, the volume calculated with equation 4.7 has to be included in the predictions made for the delayed splash in equation 4.10. The estimation made using both equations indicates that indeed more liquid can be ejected than deposited by the primary drop when the crown breaks up completely. To conclude, the results presented in this thesis allow for an almost complete characterizing of the outcome of high-speed drop impacts on thin moving films. The use of the presented models and the detailed experimental and numerical data would indeed help understand the complex physical phenomenon of splashing in cases like aircraft in-flight icing, and many other technical applications.

5 Conclusions and outlook

This study shows that high-speed drop splashing is a complex three-dimensional phenomenon, which can strongly differ from the splashing observed at low-impact velocities. Although the liquids always spread axisymmetrically, usually forming a clearly defined crown, the formation of jets and their subsequent break-up drastically changes when the impact velocity is increased. The discrepancies become more notable when the surface is wetted with a liquid; therefore, a universal model describing all the splashing phenomena seems to be inconceivable. For this reason, each phenomenon has to be treated separately.

Splashing on dry surfaces

The splashing during the high-speed impact of drops on dry smooth surfaces is attributed to the aerodynamic lift force acting on the spreading lamella, as proposed by Riboux and Gordillo (2014). This force depends on the physical properties of the surrounding gas and is responsible for the levitation of the fast-moving lamella. The surrounding gas also plays an important role at the early stage of the impact by affecting the morphology and size of the entrapped gas bubble. However, the entrapment of gas was observed in all conducted experiments, even though no secondary droplets were ejected. This clearly indicates that droplet deformation at the early stage of the impact is not the mechanism responsible for splashing. Once secondary droplets are ejected, two typical outcomes are identified: the corona and the prompt splash. Each of these outcomes leads to a completely different splashing scenario, indicating that the regimes must be treated separately; however, prior to this study, there was no clear definition of what the prompt splash is. As a result of this study, it was possible to define the prompt splash as a scenario where multiple jets are formed in the azimuthal direction and the length of the break-up is similar to the thickness of the spreading lamella.

One of the possible mechanisms leading to the prompt splash is the Rayleigh-Taylor instability of the spreading liquid. Using this mechanism, it is feasible to determine the boundaries defining the prompt

splash regime. The first physical condition was derived using the rate of growth of the fastest unstable mode in the spreading liquid film. In this case, the break-up length must be of the same size or smaller than the lamella thickness. This assumption indicates that prompt splash occurs when $Oh < 0.0044$. The second physical condition was derived using the wavelength of the corresponding unstable mode. The wavelength has to be smaller than the spreading diameter in order to generate multiple jets in the azimuthal direction. This condition indicates that the prompt splash has to occur when $We \geq 34Re^{1/4}$.

Although the splashing of high-speed drops on dry smooth surfaces can be a complex physical phenomenon, some quantities of the ejected small secondary droplets are weakly dependent of the impact conditions. For example, it has been demonstrated that the non-dimensional droplet size distribution in a splashing regime is independent of the impact conditions or gas properties in the investigated parameter range. However, the droplet size distributions for the corona and prompt splash differ drastically from each other. The dimensionless velocity magnitude of the secondary droplets seems to be independent on the splashing regime. Over time, the velocity magnitude of the droplets behaves like $\sim 1/\sqrt{\tau}$. On the contrary, the angle of ejection of the smallest droplets increases with time and depends on the physical properties of the surrounding gas and kinematic impact conditions. It was demonstrated using different gas mixtures at the same ambient pressure that the lift force acting on the lamella is affected mostly by the density, followed by the viscosity, and lastly by the mean free path of the gas. The splash of different liquids with air as the surrounding gas shown that, on average, the droplets in the prompt splash are ejected at a lower angle than in the corona splash. The total ejected volume and the number of ejected droplets during splashing is affected strongly by the surrounding gas. It has been demonstrated in this thesis that the total ejected volume and the number of secondary droplets mainly increases with the impact velocity, liquid viscosity, and gas density. The results of this study lead to the conclusion that the Reynolds number – due to the liquid viscosity – plays a more important role than the Weber number, which weakly influences the generation of secondary droplets during high-speed impacts on dry smooth surfaces.

During the ejection of secondary droplets, the liquid on the surface continues to spread until the maximal diameter is reached. The dynamics of the liquid at this latter phase are dominated mainly by inertial, viscous, and surface tension forces. It has been demonstrated that the velocity of the spreading liquid is weakly dependent on the kinematic

impact conditions. Since the total ejected volume during splashing on dry surfaces represents only a small portion of the drop before the impact, it is also possible to estimate the maximal spreading diameter by considering a viscous force on the flow (Roisman, 2009). This thesis provides an extensive analysis of the splashing of high-speed drops on dry smooth surfaces from the early stage of the impact until the maximal spreading diameter is reached. A novel approach extending the theory of Riboux and Gordillo (2014) has been proposed in this study to predict whether a drop would splash or not, distinguish different splashing regimes, and estimate the entire outcome of splashing. The proposed approach can be used to estimate with high accuracy the mean diameter, velocity magnitude, and the total ejected volume of drops impacting on a smooth dry surface at relatively high velocity. The results of this extensive analysis can also be used to explain and characterize more accurately the underlying physics in many technical applications.

Splashing on wetted surfaces

The splashing during the high-speed impact of drops on wetted surfaces is a complex phenomenon that depends on the kinematic impact condition of the drop and the film and on the physical properties of the used liquids. At the early stage of the impact, the ejected sheet develops in a very irregular form as a result of a von Kármán vortex generated between the drop and the film, as shown in the numerical simulations presented in this study. The break-up of this ejecta sheet originates the smallest and fastest secondary droplets; the sheet then continues growing, forming the common crown-like lamella. The crown formation is well described by the kinematic discontinuity in the film thickness and velocity distributions, as proposed by Yarin and Weiss (1995). The theory of Yarin and Weiss (1995) can be used to characterize the crown diameter and height with a fair agreement in the case of high-speed impacts; however, it is only suited for thin films.

The experimental results from this thesis demonstrate that the film velocity affects the development of crown geometry. However, when the mean velocity of the film is $< 0.05U$, the crown formation develops similarly to the widely observed impacts on liquid layers at rest. When the mean velocity of the film is increased to $> 0.1U$, the film flow induces a strong curvature on the uprising liquid lamella. This curved lamella was observed only until $\tau \approx 5$ for all the impact velocities investigated here. Afterwards, the crown grows perpendicularly to the

film, and symmetrical shape is formed. It is also shown that the crown diameter decreases and its height increases along with the velocity and thickness of the film in the last stages of splashing $\tau > 5$. Another important effect observed in this study is that the movement of the film delays the break-up process since it continuously supplies the crown with liquid from the film.

The generation of secondary droplets during the crown formation is directly related to periodic instabilities acting on the free rim. These instabilities are responsible for the jet formation and the subsequent fragmentation into secondary droplets. In the case of very high impact velocity, the crown is formed in a very chaotic way, bending and deforming itself during the entire splashing process. The high deceleration of the crown notably influences the growth rate of the rim-bending instability. The fact that at high impact velocity the lamella and jets are strongly bent in comparison with the low-speed impacts suggests that the Rayleigh-Taylor instabilities indeed are the dominant rim instabilities during the splashing of high-speed drops. At the latter stages of impact, the crown recedes at a relatively low velocity, and the rim might be susceptible to Rayleigh-Plateau instabilities. As different mechanisms are probably in action at different stages of the splashing, it is acceptable to expect that the splashing is a complex phenomenon caused by a combination of at least three different mechanisms.

The splashing on thin films generates a host of small secondary droplets in a wide range of sizes and velocities. The arithmetic mean diameter of the droplets seems to correlate very well with the boundary layer thickness of the lamella as $d_{10} \approx 5DRe^{1/2}$. This scaling has been successfully corroborated in many cases, from the impact on dry surfaces to spray impacts. The velocity of these droplets varies over time and behaves like $\overline{u}/U \sim 1/\tau$ in all the studied configurations; therefore, it seems to be weakly dependent on the remaining impact conditions such as the drop diameter, film thickness, and velocity. The total ejected volume depends strongly on the impact conditions and can be model using a combination of the physical properties and impact conditions. It is demonstrated in this thesis that the total ejected volume for high-speed impacts can be estimated as $V_{tot}/V_D = 0.036(K-K_{lim})^{0.66}$, where the dimensionless parameter K is a function of We, Re, δ, and u^*. This formulation is valid when analyzing the impact on wet surfaces since the outcome in this case is almost independent of the surrounding gas, contrary to the splashing on dry surfaces.

The experimental study shows that the crown form during a high-speed impact can completely destroy itself due to two different types

of instabilities: the hole formation and the separation from its base. The holes were typically observed in the upper middle region of the crown, where the lamella becomes very thin. The holes tended to spread throughout the free liquid lamella until the crown base or rim was reached. Once this occurred, long liquid ligaments formed and then broke up into secondary droplets. The possible reasons for the hole formation are the very strong fluctuations in the lamella, the collision of small secondary drops with the lamella, or the rupturing of small bubbles in the film. It is important to mention that the high-speed drop impact on thin films leads to the formation of a very thin liquid lamella, which can also burst spontaneously, producing holes.

The crown separation from the base occurs when the film velocity and thickness are low. Since the film is thin and the impact velocity high, the surface tension cannot stabilize the spreading crown at the base, and the rupture with subsequent separation occurs. Using the Taylor-Culick retraction equation during the rupturing of the crown, it was possible to estimate the lamella thickness at the moment of rupture, which seems to be weak dependent of the impact conditions and is equal to ~ 30 μm. However, more experiments are needed to confirm if this estimated lamella thickness is the minimum required to promote hole formation during the splashing on moving liquid films. When this phenomenon occurs, the total ejected volume increases drastically, and more liquid can be ejected than provided by the drop prior to the impact. In this study, it is proposed to estimate the total ejected volume in the latter stages of the impact by assuming the crown as a hollow cylinder and knowing the external dimensions and thickness.

This investigation provides an in-depth analysis of the splashing phenomenon on thin moving films, beginning with the gas entrapment at the early stage of the impact and ending with the complete atomization of the crown in the last stage of the impact. It is demonstrated that the outcome of splashing of high-speed drops on wetted surfaces can be well described using different theories. The models developed in this thesis allows to estimate almost the entire outcome of splashing by means of size, velocity, and the total ejected volume when a drop impacts at high velocity on films of the same liquid.

Outlook

Although this study explores the underlying physics of the splashing phenomena, there are some limitations in the experimental and numerical methods used here, and some other scenarios deserve a closer look

in the future. For example, it has been observed that the drop shape before the impact may influence the outcome of splashing; thus, for many technical applications, it is relevant to understand how much the drop deformation would affect the splashing. This understanding may gain importance in processes that involve the splashing of fast and very large drops.

The effect of surface properties on high-speed impacts has not been studied here but deserves more attention. Understanding which surface properties affect the impact outcome the most can lead to a more focused development of future materials. Recently, some theoretical studies have concentrated on this topic; however, the lack of experimental data makes it difficult to validate them.

The oblique impact is the most common situation in nature and can be observed in many technical applications. The non-axisymmetry of the spreading lamella requires that the impact is recorded from multiple perspectives or simulated using 3D test cases. The presented experimental set-up can be adapted with some effort to study such kind of scenarios (Burzynski and Bansmer, 2019a). However, a parametric study of such a scenario is still needed, especially to quantify the total ejected volume in the case of impacts on dry and wetted surfaces.

The surface and liquid temperature may also play an important role in the outcome of high-speed drop impacts, and it is important for multiple applications. A change in the impact outcome due to a change in the surface temperature can be expected. Even small changes in the surface temperature can alter the physical properties of the surrounding gas, such as density or viscosity. As a consequence, the splashing outcome on dry surface can vary. A comprehensive study about these effects would help to better understand the complex phenomenon of splashing.

Numerical simulations on splashing provide helpful information about splashing; however, the large number of length and time scales to be solved with the simulations leads to costly calculations. Direct numerical simulation of high-speed drop impacts should be attempted in the future to clarify the origin of the strong undulations observed in the crown formation.

Nomenclature

Abbrevations

Ar	Argon
CFD	Computational Fluid Dynamics
CO_2	Carbon Dioxide
DFT	Discrete Fourier Transform
DNS	Direct Numerical Simulation
DOF	Depth Of Field
FORJ	Fiber Optic Rotary Joints
He	Helium
LWC	Liquid Water Content
MULES	Multidimensional Universal Limiter for Explicit Solution
NH_3	Ammonia
NO_x	Nitrogen Oxide
O_2	Oxygen
RANS	Reynolds-Averaged Navier-Stokes
RG	Riboux and Gordillo
SF_6	Sulfur Hexafluoride
TVD	Total Variation Diminishing
VOF	Volume Of Fluid

Latin Letters

a	Radius of the wetted region (Eq. 3.10)
a_l	Film acceleration (Eq. 3.6)
A	Exit nozzle area
c_g	Speed of sound in the gas
C_A	Experimental fitting constant (Eq. 3.23)
d	Secondary drop diameter
d_{10}	Arithmetic mean diameter
d_b	Gas bubble diameter (Sec. 3.2.1)
d_c	Crown diameter (Sec. 4.3.2)
d_{id}	individual droplet diameter (Sec. 2.3)

d_{model}	Predicted droplet diameter
D	Drop diameter
D_{rim}	Spreading diameter (Sec. 3.5)
D_c	Dimensionsless crown diameter (Sec. 4.3.2)
$f_{g,i}$	Gravity source term (Eq. 2.4)
$f_{\sigma,i}$	Surface tension source term (Eq. 2.4)
F_L	Lift force (Eq. 3.17)
Fr	Froude number
g	Gravitational force
h_a	Rim thickness at the wetted region (Eq. 3.15)
h_a^+	Rim thickness considering viscous forces (Eq. 3.15)
h_c	Crown height (Sec. 4.3.2)
h_ct	Crown thickness (Eq. 4.8)
h_c^*t	Dimensionsless crown thickness (Eq. 4.10)
h_f	Dimensionsless film thickness (Sec. 3.1)
h_l	Dimensionless thickness of the ejected lamella (Eq. 3.12)
h_μ	Thickness of the spreading film (Eq. 3.6)
H_b	Gas entrapment height (Eq. 3.1)
H_c	Dimensionsless crown height (Sec. 4.3.2)
H_l	Dimensionless thickness of the ejected lamella (Eq. 3.14)
k_w	Wave number (Eq. 4.9)
K	Splashing parameter (Mundo et al. (1995))
K_{lim}	Splashing threshold for wetted surfaces (Eq. 4.7)
K_{lub}	Constant obtained from the lubrication theory (Eq. 3.17)
K_u	Drag coefficient obtained from numerical simulations (Eq. 3.17)
ℓ	Wavelength of the most unstable mode (Eq. 3.7)
L_a	Length scale of the surface roughness (Sec. 4.3)
Ma	Mach number
n	Number of samples (Eq. 2.2)
Oh	Ohnesorge number
Oh_R	Ohnesorge number based on drop radius (Eq. 3.11)
$Oh^\star$	Threshold Ohnesorge number (Eq. 3.8)
p	Pressure
p^*	Dimensionless pressure (Eq. 3.10)
P	Dimensionless parameter (Eq. 3.23)
$\dot{Q}_{in}$	Flow rate entering the flywheel
$\dot{Q}_{out}$	Flow rate exiting the flywheel
$\dot{Q}_{ej}$	Flow rate through ejector
R	Drop radius
R_a	Arithmetic surface roughness
R_{wet}	Dimensionless radius of the region wetted by the drop (Eq. 3.10)

Re	Reynolds number
Re_R	Reynolds number based on drop radius (Eq. 3.11)
$\tilde{Re}$	Reynolds number of the spreading film (Eq. 3.6)
R_F	Flywheel radius
s	Transformed horizontal axis (Sec. 4.5)
St	Stokes number
t	Time
t_B	Time of lamella ejection from the base (Eq. 4.5)
t_R	Time at which the discontinuity reaches the rim (Eq. 4.5)
T	Temperature
T_e	Ejection time of the lamella (Eq. 3.14)
u	Secondary drop velocity
u^*	Dimensionless film velocity (Eq. 4.4)
$\overline{u}$	Mean secondary droplet velocity
$u_{a,x}$	Rim velocity at the wetted region (Eq. 3.16)
$u_{a,x}^+$	Rim velocity considering viscous forces (Eq. 3.16)
u_i	Velocity component
u_{id}	Individual droplet velocity
u_l	Dimensionless velocity of the ejected lamella (Eq. 3.13)
$u_{x,model}$	Predicted horizontal velocity (Sec. 3.4.4)
$u_{y,model}$	Predicted vertical velocity (Sec. 3.4.4)
U	Impact velocity
$U_{f,exit}$	Film exit velocity (Sec. 2.1.3)
U_{hole}	Expansion velocity of the holes (Eq. 4.8)
U_l	Dimensionless velocity of the ejected lamella (Eq. 3.14)
U_D	Drop velocity
U_f	Film velocity (Sec. 2.1.3)
U_S	Surface velocity (Sec. 2.1.2)
V_b	Entrapped volume (Sec. 4.2)
V_c	Crown volume (Eq. 4.10)
V_D	Drop volume prior impact
V_{id}	Individual droplet volume
V_{tot}	Total ejected volume during splashing (Eq. 3.21)
$\dot{V}_{tot}$	Volumetric flow rate of the ejected droplets (Eq. 2.1)
We	Weber number
$\tilde{We}$	Weber number of the spreading film (Eq. 3.6)
x_{id}	Individual droplet horizontal position (Sec. 2.3)
x_{imp}	Impact position (Sec. 2.3)
$\boldsymbol{X}_J(t_b, t)$	Radius vector defining the crown shape (Eq. 4.5)
x, y, z	Cartesian coordinates
$Z^\star$	Dimensionless empirical constant (Eq. 3.9)

Z_R	Dimensionless crown height from theory (Eq. 4.5)

Greek Letters

α	Volume fraction (Eq. 2.5)
α_d	Ejection angle of the secondary droplets (Sec. 3.4.2)
β	Splashing parameter (Eq. 3.5)
β_s	Dimensionless spreading diameter (Sec. 3.5)
$\beta_{s,max}$	Maximal spreading diameter (Sec. 3.5)
β_{RT}	Dimensionless constant (Eq. 4.5)
γ	Given quantity (Eq. 2.2)
δ	Dimensionless film thickness (Eq. 4.3)
ϵ	Compressibility factor (Eq. 3.1)
ζ	Dimensionless wave number (Eq. 3.6)
η_{RT}	Dimensionless constant (Eq. 4.5)
Θ	Angular position
κ	Surface curvature (Sec. 2.4)
λ	Mean free path of gas molecules
λ_w	Wavelength (Eq. 4.9)
μ	Dynamic viscosity
ν	Kinematic viscosity
ρ	Density
σ	Surface tension
Σ	Stress on spreading lamella (Eq. 3.4)
τ	Dimensionsless time
τ_e	Dimensionless ejection time of the lamella (Eq. 3.11)
τ_{RT}	Dimensionless constant (Eq. 4.5)
ϕ	Angular velocity (Sec. 2.1.2)
Φ_s	Extrapolated volume flux rate (Eq. 2.1)
χ	Gas concentration (Tab. 2.2)
ψ	Depth of Field (Sec. 2.1.2)
ω	Perturbation growth (Eq. 3.6)

Publications

Peer-reviewed journal articles

1. Burzynski, D. A., Roisman, I. V., and Bansmer, S. E. (2020). On the splashing of high-speed drops impacting a dry surface. *Journal of Fluid Mechanics*, 892(A2)

   Contribution of D. Burzynski: conducted the literature review and selected the journal, conceived and designed the experiments, performed the experiments and collected the data, developed the code to analyze the data, performed the statistical analysis, implemented and analyzed the RG theory, verified the RT instability analysis and the threshold conditions, interpreted the theoretical and experimental results, structured the manuscript, generated the figures, wrote the paper, and responded to the reviewers. *Contribution of I. Roisman:* conducted part of the literature review, developed the RT instability analysis and derived the threshold conditions, provided the figures 2 and 3, structured part of the manuscript, wrote part of the initial draft, and revised the final paper. *Contribution of S. Bansmer:* revised the final paper.

2. Burzynski, D. A. and Bansmer, S. E. (2019c). Role of surrounding gas in the outcome of droplet splashing. *Physical Review Fluids*, 4(7):073601

   Contribution of D. Burzynski: conducted the literature review and selected the journal, conceived and designed the experiments, performed the experiments and collected the data, developed the code to analyze the data, performed the statistical analysis, implemented and analyzed the RG theory, interpreted the theoretical and experimental results, structured the manuscript, generated the figures, wrote the paper, and responded to the reviewers. *Contribution of S. Bansmer:* revised the final paper.

3. Burzynski, D. A. and Bansmer, S. E. (2018a). Droplet splashing on thin moving films at high weber numbers. *International Journal of Multiphase Flow*, 101:202–211

   Contribution of D. Burzynski: conducted the literature review and selected the journal, conceived and designed the experiments, performed the experiments and collected the data, developed the code to analyze the data, analyzed the obtained data and interpreted the results, structured the manuscript, generated the figures, wrote the paper, and responded to the reviewers. *Contribution of S. Bansmer:* formulated the idea of performing the DFT, suggested the use of a nonlinear theory for the lamella thickness estimation, coordinated the loan of the camera, and revised the final paper.

4. Pierzyna, M., Burzynski, D. A., Bansmer, S. E., and Semaan, R. (2021). Data-driven splashing threshold model for drop impact on dry smooth surfaces. *(Under Review)*

   Contribution of M. Pierzyna: conducted the literature review, collected and digitalized the experimental data, selected the algorithms to be used, developed and implemented the code to analyze the data, interpreted the results, generated the figures, and wrote the first draft of the paper. *Contribution of D. Burzynski:* formulated and conceived the research idea, initiated the internal cooperation, conducted the literature review related to the physical phenomena, interpreted, analyzed, and abstracted the results, structured the manuscript, and wrote the paper together with M. Pierzyna and R. Semaan. *Contribution of S. Bansmer:* revised the final paper. *Contribution of R. Semaan:* conducted the literature review, proposed and supervised the used methodology, interpreted and analyzed the methodology results, and wrote the paper together with M. Pierzyna and D. Burzynski.

Conference proceedings

1. Burzynski, D. A. and Bansmer, S. E. (2018b). High speed visualization of droplets impacting with a dry surface at high weber numbers. In *New Results in Numerical and Experimental Fluid Mechanics XI*, pages 511–521. Springer. (Peer-reviewed conference)

Contribution of D. Burzynski: conducted the literature review, conceived and designed the experiments, performed the experiments and collected the data, developed the code to analyze the data, performed the statistical analysis, interpreted the experimental results, structured the manuscript, generated the figures, wrote the paper, and responded to the reviewers. *Contribution of S. Bansmer:* selected the conference, selected the impact conditions, coordinated the loan of the high-speed camera, interpreted the experimental results, and revised the final paper.

2. Burzynski, D. A. and Bansmer, S. E. (2019a). The effect of impact angle on the secondary droplets at high impact velocity. In *ILASS–Europe 2019, 29th Conference on Liquid Atomization and Spray Systems, 2-4 September 2019, Paris, France.* (Peer-reviewed conference)

   Contribution of D. Burzynski: conducted the literature review and selected the conference, conceived and designed the experiments, performed the experiments and collected the data, developed the code to analyze the data, performed the statistical analysis, implemented and analyzed the RG theory, interpreted the theoretical and experimental results, structured the manuscript, generated the figures, wrote the paper, and responded to the reviewers. *Contribution of S. Bansmer:* revised the final paper.

3. Burzynski, D. A. and Bansmer, S. E. (2019b). Experimental and numerical study of the effect of surrounding gas on splashing at high weber and reynolds numbers. In *72nd Annual Meeting of the APS Division of Fluid Dynamics, Vol. 64, No. 13, Seattle, USA*

   Contributions of D. Burzynski: conducted the literature review and selected the conference, setup and performed the numerical simulations, interpreted the numerical results, structured the manuscript, generated the figures, and wrote the paper. *Contribution of S. Bansmer:* revised the final paper.

Bibliography

Aboud, D. G. K. and Kietzig, A.-M. (2015). Splashing threshold of oblique droplet impacts on surfaces of various wettability. *Langmuir*, 31(36):10100–10111.

Adebayo, I. T. and Matar, O. K. (2017). Droplet impact on flowing liquid films with inlet forcing: the splashing regime. *Soft matter*, 13(41):7473–7485.

Agbaglah, G. and Deegan, R. (2014). Growth and instability of the liquid rim in the crown splash regime. *Journal of fluid mechanics*, 752:485–496.

Agbaglah, G., Josserand, C., and Zaleski, S. (2013). Longitudinal instability of a liquid rim. *Physics of Fluids*, 25(2):022103.

Agbaglah, G., Thoraval, M.-J., Thoroddsen, S. T., Zhang, L. V., Fezzaa, K., and Deegan, R. D. (2015). Drop impact into a deep pool: vortex shedding and jet formation. *Journal of fluid mechanics*, 764.

Alghoul, S. K., Eastwick, C. N., and Hann, D. B. (2011). Normal droplet impact on horizontal moving films: an investigation of impact behaviour and regimes. *Experiments in fluids*, 50(5):1305–1316.

Aljedaani, A. B., Wang, C., Jetly, A., and Thoroddsen, S. T. (2018). Experiments on the breakup of drop-impact crowns by marangoni holes. *Journal of Fluid Mechanics*, 844:162–186.

Allen, M. R. and Ingram, W. J. (2002). Constraints on future changes in climate and the hydrologic cycle. *Nature*, 419(6903):228–232.

Armandoost, P., Bayareh, M., and Nadooshan, A. A. (2018). Study of the motion of a spheroidal drop in a linear shear flow. *Journal of Mechanical Science and Technology*, 32(5):2059–2067.

Bansmer, S. E., Baumert, A., Sattler, S., Knop, I., Leroy, D., Schwarzenboeck, A., Jurkat-Witschas, T., Voigt, C., Pervier, H., and Esposito, B. (2018). Design, construction and commissioning of the braunschweig icing wind tunnel.

Baumert, A. (2019). *Experimental and Numerical Studies on Ice Crystal Icing of Civil Aircraft*. PhD thesis, Technische Universität Braunschweig, Braunschweig.

Baumert, A., Bansmer, S., Trontin, P., and Villedieu, P. (2018). Experimental and numerical investigations on aircraft icing at mixed phase conditions. *International Journal of Heat and Mass Transfer*, 123:957–978.

Beaugendre, H., Morency, F., and Habashi, W. G. (2003). Fensap-ice's three-dimensional in-flight ice accretion module: Ice3d. *Journal of Aircraft*, 40(2):239–247.

Berberović, E., van Hinsberg, N. P., Jakirlić, S., Roisman, I. V., and Tropea, C. (2009). Drop impact onto a liquid layer of finite thickness: Dynamics of the cavity evolution. *Physical Review E*, 79(3):036306.

Berg, T., Deppe, J., Michaelis, D., Voges, H., and Wissel, S. (2006). Comparison of particle size and velocity investigations in sprays carried out by means of different measurement techniques. *ICLASS'06, Kyoto, Japan*.

Berthoumieu, P. and Djean, B. (2017). Experimental investigation of sld impact phenomena. In *7th European conference for aeronautics and space sciences (EUCASS)*.

Bird, J. C., Tsai, S. S. H., and Stone, H. A. (2009). Inclined to splash: triggering and inhibiting a splash with tangential velocity. *New Journal of Physics*, 11(6):063017.

Boelens, A. M. P. and de Pablo, J. J. (2018). Simulations of splashing high and low viscosity droplets. *Physics of Fluids*, 30(7):072106.

Brackbill, J. U., Kothe, D. B., and Zemach, C. (1992). A continuum method for modeling surface tension. *Journal of computational physics*, 100(2):335–354.

Breitenbach, J., Roisman, I. V., and Tropea, C. (2018). From drop impact physics to spray cooling models: a critical review. *Experiments in Fluids*, 59(3):55.

Burzynski, D. A. and Bansmer, S. E. (2018a). Droplet splashing on thin moving films at high weber numbers. *International Journal of Multiphase Flow*, 101:202–211.

Burzynski, D. A. and Bansmer, S. E. (2018b). High speed visualization of droplets impacting with a dry surface at high weber numbers. In *New Results in Numerical and Experimental Fluid Mechanics XI*, pages 511–521. Springer.

Burzynski, D. A. and Bansmer, S. E. (2019a). The effect of impact angle on the secondary droplets at high impact velocity. In *ILASS–Europe 2019, 29th Conference on Liquid Atomization and Spray Systems, 2-4 September 2019, Paris, France*.

Burzynski, D. A. and Bansmer, S. E. (2019b). Experimental and numerical study of the effect of surrounding gas on splashing at high weber and reynolds numbers. In *72nd Annual Meeting of the APS Division of Fluid Dynamics, Vol. 64, No. 13, Seattle, USA*.

Burzynski, D. A. and Bansmer, S. E. (2019c). Role of surrounding gas in the outcome of droplet splashing. *Physical Review Fluids*, 4(7):073601.

Burzynski, D. A., Roisman, I. V., and Bansmer, S. E. (2020). On the splashing of high-speed drops impacting a dry surface. *Journal of Fluid Mechanics*, 892(A2).

Caminade, F. and Frazza, L. (2019). Focus on challenges in sld regime: Reemitted droplet modelling. Technical report, SAE Technical Paper.

Castrejón-Pita, A., Castrejón-Pita, J., and Hutchings, I. (2012). Experimental observation of von kármán vortices during drop impact. *Physical Review E*, 86(4):045301.

Castrejón-Pita, J. R., Muñoz-Sánchez, B. N., Hutchings, I. M., and Castrejón-Pita, A. (2016). Droplet impact onto moving liquids. *Journal of Fluid Mechanics*, 809:716–725.

Chandra, S. and Avedisian, C. (1991). On the collision of a droplet with a solid surface. *Proceedings of the Royal Society of London. Series A: Mathematical and Physical Sciences*, 432(1884):13–41.

Chandrasekhar, S. (2013). *Hydrodynamic and hydromagnetic stability*. Courier Corporation.

Chen, H., Marengo, M., and Amirfazli, A. (2019). Drop impact onto semi-infinite solid surfaces with different wettabilities. *Physical Review Fluids*, 4(8):083601.

Chen, N., Chen, H., and Amirfazli, A. (2017). Drop impact onto a thin film: Miscibility effect. *Physics of Fluids*, 29(9):092106.

Cherukat, P. and McLaughlin, J. B. (1994). The inertial lift on a rigid sphere in a linear shear. *Journal of Fluid Mechanics*, 263:1–18.

Cimpeanu, R. and Moore, M. R. (2018). Early-time jet formation in liquid–liquid impact problems: theory and simulations. *Journal of Fluid Mechanics*, 856:764–796.

Cimpeanu, R. and Papageorgiou, D. T. (2018). Three-dimensional high speed drop impact onto solid surfaces at arbitrary angles. *International Journal of Multiphase Flow*, 107:192–207.

Clanet, C., Béguin, C., Richard, D., and Quéré, D. (2004). Maximal deformation of an impacting drop. *Journal of Fluid Mechanics*, 517:199–208.

Coleman, H. W. and Steele, W. G. (2009). *Experimentation, validation, and uncertainty analysis for engineers*. John Wiley & Sons, 3rd ed edition.

Comiskey, P., Yarin, A., Kim, S., and Attinger, D. (2016). Prediction of blood back spatter from a gunshot in bloodstain pattern analysis. *Physical Review Fluids*, 1(4):043201.

Cossali, G., Coghe, A., and Marengo, M. (1997). The impact of a single drop on a wetted solid surface. *Experiments in fluids*, 22(6):463–472.

Cossali, G., Marengo, M., Coghe, A., and Zhdanov, S. (2004). The role of time in single drop splash on thin film. *Experiments in Fluids*, 36(6):888–900.

Culick, F. (1960). Comments on a ruptured soap film. *Journal of applied physics*, 31(6):1128–1129.

de Ruiter, J., Pepper, R. E., and Stone, H. A. (2010). Thickness of the rim of an expanding lamella near the splash threshold. *Physics of Fluids*, 22(2):022104.

Deegan, R., Brunet, P., and Eggers, J. (2007). Complexities of splashing. *Nonlinearity*, 21(1):C1.

Deshpande, S. S., Anumolu, L., and Trujillo, M. F. (2012). Evaluating the performance of the two-phase flow solver interfoam. *Computational science & discovery*, 5(1):014016.

Dodds, S., Carvalho, M. S., and Kumar, S. (2012). The dynamics of three-dimensional liquid bridges with pinned and moving contact lines. *Journal of fluid mechanics*, 707:521–540.

Eggers, J., Fontelos, M. A., Josserand, C., and Zaleski, S. (2010). Drop dynamics after impact on a solid wall: theory and simulations. *Physics of Fluids*, 22(6):062101.

Eggers, J. and Villermaux, E. (2008). Physics of liquid jets. *Reports on progress in physics*, 71(3):036601.

Entov, V., Sultanov, F., and Yarin, A. (1985). Breakup of liquid films under the action of a pressure drop in the ambient gas. In *Soviet Physics Doklady*, volume 30, page 882.

Entov, V., Sultanov, F., and Yarin, A. (1986). Disintegration of liquid films subjected to an ambient gas pressure difference. *Fluid dynamics*, 21(3):376–383.

Erkal, A., D'Ayala, D., and Sequeira, L. (2012). Assessment of wind-driven rain impact, related surface erosion and surface strength reduction of historic building materials. *Building and Environment*, 57:336–348.

Faßmann, B. W. (2015). *Zeitabhängige Charakterisierung der Sekundärtropfen aus dem Hochgeschwindigkeitsaufprall einzelner Flüssigkeitstropfen.* TU Braunschweig, Niedersächsisches Forschungszentrum für Luftfahrt.

Faßmann, B. W., Bansmer, S. E., Möller, T. J., Radespiel, R., and Hartmann, M. (2013). High velocity impingement of single droplets on a dry smooth surface. *Experiments in fluids*, 54(5):1516.

Fukai, J., Shiiba, Y., Yamamoto, T., Miyatake, O., Poulikakos, D., Megaridis, C. M., and Zhao, Z. (1995). Wetting effects on the spreading of a liquid droplet colliding with a flat surface: experiment and modeling. *Physics of fluids*, 7(2):236–247.

Gao, X. and Li, R. (2015). Impact of a single drop on a flowing liquid film. *Physical Review E*, 92(5):053005.

Garcia-Magariño, A., Sor, S., and Velazquez, A. (2018). Droplet breakup criterion in airfoils leading edge vicinity. *Journal of Aircraft*, 55(5):1867–1876.

Gaylard, A. P., Kirwan, K., and Lockerby, D. A. (2017). Surface contamination of cars: A review. *Proceedings of the Institution of Mechanical Engineers, Part D: Journal of Automobile Engineering*, 231(9):1160–1176.

Gekle, S. and Gordillo, J. M. (2010). Generation and breakup of worthington jets after cavity collapse. part 1. jet formation. *Journal of fluid mechanics*, 663:293–330.

Gent, R., Dart, N., and Cansdale, J. (2000). Aircraft icing. *Philosophical Transactions of the Royal Society of London. Series A: Mathematical, Physical and Engineering Sciences*, 358(1776):2873–2911.

Geppert, A., Terzis, A., Lamanna, G., Marengo, M., and Weigand, B. (2017). A benchmark study for the crown-type splashing dynamics of one-and two-component droplet wall–film interactions. *Experiments in Fluids*, 58(12):172.

Gibson, I., Rosen, D. W., Stucker, B., et al. (2014). *Additive manufacturing technologies*, volume 17. Springer.

Gilet, T. and Bourouiba, L. (2014). Rain-induced ejection of pathogens from leaves: revisiting the hypothesis of splash-on-film using high-speed visualization.

Gordillo, J. M. and Riboux, G. (2019). A note on the aerodynamic splashing of droplets. *Journal of Fluid Mechanics*, 871.

Gordillo, J. M., Riboux, G., and Quintero, E. S. (2019). A theory on the spreading of impacting droplets. *Journal of Fluid Mechanics*, 866:298–315.

Greenshields, C. J. (2019). *OpenFOAM: User Guide version 7*. OpenFOAM Foundation Ltd.

Gregory, P., Guthrie, E., and Bunce, M. E. (1959). Experiments on splash dispersal of fungus spores. *Microbiology*, 20(2):328–354.

Günther, C., Bröder, J., and Joos, F. (2017). Influence of pressure on droplet splashing behaviour inside gas turbine compressors during wet compression.

Guo, Y. and Lian, Y. (2017). High-speed oblique drop impact on thin liquid films. *Physics of Fluids*, 29(8):082108.

Guo, Y., Lian, Y., and Sussman, M. (2016). Investigation of drop impact on dry and wet surfaces with consideration of surrounding air. *Physics of Fluids*, 28(7):073303.

Haar, D. (2016). *Design of droplet impingement measurement set-up*. PhD thesis, University of Twente.

Hagemeier, T., Hartmann, M., and Thévenin, D. (2011). Practice of vehicle soiling investigations: A review. *International Journal of Multiphase Flow*, 37(8):860–875.

Hammond, D., Quero, M., Ivey, P., Miller, D., Purvis, R., McGregor, O., and Tan, J. (2005). Analysis and experimental aspects of the impact of supercooled water droplets into thin water films. In *43rd AIAA Aerospace Sciences Meeting and Exhibit*, page 77.

Hao, J. and Green, S. I. (2017). Splash threshold of a droplet impacting a moving substrate. *Physics of Fluids*, 29(1):012103.

Hendrix, M. H., Bouwhuis, W., van der Meer, D., Lohse, D., and Snoeijer, J. H. (2016). Universal mechanism for air entrainment during liquid impact. *Journal of fluid mechanics*, 789:708–725.

Hicks, P. D. and Purvis, R. (2010). Air cushioning and bubble entrapment in three-dimensional droplet impacts. *Journal of Fluid Mechanics*, 649:135–163.

Hicks, P. D. and Purvis, R. (2011). Air cushioning in droplet impacts with liquid layers and other droplets. *Physics of fluids*, 23(6):062104.

Hicks, P. D. and Purvis, R. (2013). Liquid–solid impacts with compressible gas cushioning. *Journal of Fluid Mechanics*, 735:120–149.

Hirt, C. W. and Nichols, B. D. (1981). Volume of fluid (vof) method for the dynamics of free boundaries. *Journal of computational physics*, 39(1):201–225.

Hoath, S. D. (2016). *Fundamentals of inkjet printing: the science of inkjet and droplets*. John Wiley & Sons.

Howison, S., Ockendon, J., Oliver, J., Purvis, R., and Smith, F. (2005). Droplet impact on a thin fluid layer. *Journal of Fluid Mechanics*, 542:1–23.

Howland, C. J., Antkowiak, A., Castrejón-Pita, J. R., Howison, S. D., Oliver, J. M., Style, R. W., and Castrejón-Pita, A. A. (2016). It's harder to splash on soft solids. *Physical review letters*, 117(18):184502.

Huang, J. C. P. (1970). The break-up of axisymmetric liquid sheets. *Journal of Fluid Mechanics*, 43(2):305–319.

IBIS-World (2019). Global commercial printing industry. `https://www.ibisworld.com/global/market-research-reports/global-commercial-printing-industry/`.

Iturrioz, A., Guanche, R., Lara, J., Vidal, C., and Losada, I. (2015). Validation of openfoam® for oscillating water column three-dimensional modeling. *Ocean Engineering*, 107:222–236.

Jasak, H. (2009). Openfoam: open source cfd in research and industry. *International Journal of Naval Architecture and Ocean Engineering*, 1(2):89–94.

Jenning, S. (1988). The mean free path. *J. Aerosol Sci*, 19:159–166.

Jian, Z., Josserand, C., Popinet, S., Ray, P., and Zaleski, S. (2018). Two mechanisms of droplet splashing on a solid substrate. *Journal of Fluid Mechanics*, 835:1065–1086.

Josserand, C., Ray, P., and Zaleski, S. (2016). Droplet impact on a thin liquid film: anatomy of the splash. *Journal of Fluid Mechanics*, 802:775–805.

Josserand, C. and Thoroddsen, S. T. (2016). Drop impact on a solid surface. *Annual review of fluid mechanics*, 48:365–391.

Josserand, C. and Zaleski, S. (2003). Droplet splashing on a thin liquid film. *Physics of fluids*, 15(6):1650–1657.

Kapulla, R., Tuchtenhagen, J., Müller, A., Dullenkopf, K., and Bauer, H. (2008). Droplet sizing performance of different shadow sizing codes. *Lasermethoden in der Strömungsmesstechnik*, 16:38–1.

Kim, K. S. and Kim, S. S. (1994). Drop sizing and depth-of-field correction in tv imaging. *Atomization and Sprays*, 4(1).

Kittel, H. M. (2019). *Drop Impact onto a Wall Wetted by a Thin Film of Another Liquid*. PhD thesis, Technische Universität Darmstadt, Darmstadt.

Kittel, H. M., Roisman, I. V., and Tropea, C. (2018). Splash of a drop impacting onto a solid substrate wetted by a thin film of another liquid. *Physical Review Fluids*, 3(7):073601.

Kray, T., Franke, J., and Frank, W. (2012). Magnus effect on a rotating sphere at high reynolds numbers. *Journal of wind engineering and industrial aerodynamics*, 110:1–9.

Krechetnikov, R. (2010). Stability of liquid sheet edges. *Physics of Fluids*, 22(9):092101.

Krechetnikov, R. and Homsy, G. M. (2009). Crown-forming instability phenomena in the drop splash problem. *Journal of colloid and interface science*, 331(2):555–559.

Kuzmin, D., Löhner, R., and Turek, S. (2012). *Flux-corrected transport: principles, algorithms, and applications*. Springer.

Laan, N., de Bruin, K. G., Bartolo, D., Josserand, C., and Bonn, D. (2014). Maximum diameter of impacting liquid droplets. *Physical Review Applied*, 2(4):044018.

Lagubeau, G., Fontelos, M. A., Josserand, C., Maurel, A., Pagneux, V., and Petitjeans, P. (2012). Spreading dynamics of drop impacts. *Journal of Fluid Mechanics*, 713:50–60.

Latka, A., Strandburg-Peshkin, A., Driscoll, M. M., Stevens, C. S., and Nagel, S. R. (2012). Creation of prompt and thin-sheet splashing by varying surface roughness or increasing air pressure. *Physical review letters*, 109(5):054501.

Lee, S. H., Hur, N., and Kang, S. (2011). A numerical analysis of drop impact on liquid film by using a level set method. *Journal of Mechanical Science and Technology*, 25(10):2567.

Lejeune, S. and Gilet, T. (2019). Drop impact close to the edge of an inclined substrate: Liquid sheet formation and breakup. *Physical Review Fluids*, 4(5):053601.

Li, E. and Thoroddsen, S. T. (2015). Time-resolved imaging of a compressible air disc under a drop impacting on a solid surface. *Journal of Fluid Mechanics*, 780:636–648.

Li, E. Q., Langley, K. R., Tian, Y. S., Hicks, P. D., and Thoroddsen, S. T. (2017). Double contact during drop impact on a solid under reduced air pressure. *Physical review letters*, 119(21):214502.

Li, E. Q., Thoraval, M.-J., Marston, J. O., and Thoroddsen, S. T. (2018). Early azimuthal instability during drop impact. *Journal of Fluid Mechanics*, 848:821–835.

Li, H. (2013). *Drop Impact on Dry Surfaces With Phase Change*. PhD thesis, Technische Universität Darmstadt, Darmstadt.

Li, J., Zhang, H., and Liu, Q. (2019). Characteristics of secondary droplets produced by a single drop impacting on a static liquid film. *International Journal of Multiphase Flow*, 119:42–55.

Liang, G., Guo, Y., and Shen, S. (2014a). Gas properties on crown behavior and drop coalescence. *Numerical Heat Transfer, Part B: Fundamentals*, 65(6):537–553.

Liang, G., Guo, Y., Shen, S., and Yang, Y. (2014b). Crown behavior and bubble entrainment during a drop impact on a liquid film. *Theoretical and Computational Fluid Dynamics*, 28(2):159–170.

Liang, G. and Mudawar, I. (2017). Review of drop impact on heated walls. *International Journal of Heat and Mass Transfer*, 106:103–126.

Liu, M. and Bothe, D. (2016). Numerical study of head-on droplet collisions at high weber numbers. *Journal of Fluid Mechanics*, 789:785–805.

Malgarinos, I., Nikolopoulos, N., and Gavaises, M. (2017). Numerical investigation of heavy fuel droplet-particle collisions in the injection zone of a fluid catalytic cracking reactor, part ii: 3d simulations. *Fuel Processing Technology*, 156:43–53.

Mandre, S. and Brenner, M. P. (2012). The mechanism of a splash on a dry solid surface. *Journal of Fluid Mechanics*, 690:148–172.

Mandre, S., Mani, M., and Brenner, M. P. (2009). Precursors to splashing of liquid droplets on a solid surface. *Physical review letters*, 102(13):134502.

Mannan, F. O. and Leiderman, K. (2020). Weak inertial effects on arbitrarily shaped objects in the presence of a wall. *Physical Review Fluids*, 5(4):044102.

Marengo, M., Antonini, C., Roisman, I. V., and Tropea, C. (2011). Drop collisions with simple and complex surfaces. *Current Opinion in Colloid & Interface Science*, 16(4):292–302.

Marston, J., Vakarelski, I. U., and Thoroddsen, S. T. (2011). Bubble entrapment during sphere impact onto quiescent liquid surfaces. *Journal of fluid mechanics*, 680:660–670.

Marston, J. O., Truscott, T. T., Speirs, N. B., Mansoor, M. M., and Thoroddsen, S. T. (2016). Crown sealing and buckling instability during water entry of spheres. *Journal of Fluid Mechanics*, 794:506–529.

Mehdizadeh, N. Z., Chandra, S., and Mostaghimi, J. (2004). Formation of fingers around the edges of a drop hitting a metal plate with high velocity. *Journal of Fluid Mechanics*, 510:353–373.

Michon, G.-J., Josserand, C., and Séon, T. (2017). Jet dynamics post drop impact on a deep pool. *Physical Review Fluids*, 2(2):023601.

Moore, M. R., Whiteley, J. P., and Oliver, J. M. (2018). On the deflection of a liquid jet by an air-cushioning layer. *Journal of Fluid Mechanics*, 846:711–751.

Moreira, A. L. N., Moita, A. S., and Panao, M. R. (2010). Advances and challenges in explaining fuel spray impingement: How much of single droplet impact research is useful? *Progress in energy and combustion science*, 36(5):554–580.

Moukalled, F., Mangani, L., Darwish, M., et al. (2016). *The finite volume method in computational fluid dynamics*, volume 113. Springer.

Mundo, C. H. R., Sommerfeld, M., and Tropea, C. (1995). Droplet-wall collisions: experimental studies of the deformation and breakup process. *International journal of multiphase flow*, 21(2):151–173.

Murphy, D. W., Li, C., d'Albignac, V., Morra, D., and Katz, J. (2015). Splash behaviour and oily marine aerosol production by raindrops impacting oil slicks. *Journal of Fluid Mechanics*, 780:536–577.

Néel, B. and Villermaux, E. (2018). The spontaneous puncture of thick liquid films. *Journal of Fluid Mechanics*, 838:192–221.

Okawa, T., Shiraishi, T., and Mori, T. (2006). Production of secondary drops during the single water drop impact onto a plane water surface. *Experiments in fluids*, 41(6):965.

Opfer, L., Roisman, I., Venzmer, J., Klostermann, M., and Tropea, C. (2014). Droplet-air collision dynamics: Evolution of the film thickness. *Physical Review E*, 89(1):013023.

Ostrach, S. and Koestel, A. (1965). Film instabilities in two-phase flows. *AIChE Journal*, 11(2):294–303.

Palacios, J., Hernández, J., Gómez, P., Zanzi, C., and López, J. (2013). Experimental study of splashing patterns and the splashing/deposition threshold in drop impacts onto dry smooth solid surfaces. *Experimental Thermal and Fluid Science*, 44:571–582.

Pan, K. L., Tseng, K. C., and Wang, C. H. (2010). Breakup of a droplet at high velocity impacting a solid surface. *Experiments in fluids*, 48(1):143–156.

Pasandideh-Fard, M., Bhola, R., Chandra, S., and Mostaghimi, J. (1998). Deposition of tin droplets on a steel plate: simulations and experiments. *International Journal of Heat and Mass Transfer*, 41(19):2929–2945.

Philippi, J., Lagrée, P., and Antkowiak, A. (2016). Drop impact on a solid surface: short-time self-similarity. *Journal of Fluid Mechanics*, 795:96–135.

Pierzyna, M., Burzynski, D. A., Bansmer, S. E., and Semaan, R. (2021). Data-driven splashing threshold model for drop impact on dry smooth surfaces. *(Under Review)*.

Politovich, M. K. (1989). Aircraft icing caused by large supercooled droplets. *Journal of Applied Meteorology*, 28(9):856–868.

Prévost, M. and Gallez, D. (1986). Nonlinear rupture of thin free liquid films. *The Journal of chemical physics*, 84(7):4043–4048.

Quetzeri-Santiago, M. A., Yokoi, K., Castrejón-Pita, A. A., and Castrejón-Pita, J. R. (2019). Role of the dynamic contact angle on splashing. *Physical Review Letters*, 122(22):228001.

Quintero, E. S., Riboux, G., and Gordillo, J. M. (2019). Splashing of droplets impacting superhydrophobic substrates. *Journal of Fluid Mechanics*, 870:175–188.

Raman, K. A., Jaiman, R. K., Sui, Y., Lee, T.-S., and Low, H.-T. (2016). Rebound suppression of a droplet impacting on an oscillating horizontal surface. *Physical Review E*, 94(2):023108.

Rein, M. (1993). Phenomena of liquid drop impact on solid and liquid surfaces. *Fluid Dynamics Research*, 12(2):61.

Riboux, G. and Gordillo, J. M. (2014). Experiments of drops impacting a smooth solid surface: a model of the critical impact speed for drop splashing. *Physical review letters*, 113(2):024507.

Riboux, G. and Gordillo, J. M. (2015). The diameters and velocities of the droplets ejected after splashing. *Journal of Fluid Mechanics*, 772:630–648.

Riboux, G. and Gordillo, J. M. (2017). Boundary-layer effects in droplet splashing. *Physical Review E*, 96(1):013105.

Rioboo, R., Bauthier, C., Conti, J., Voue, M., and De Coninck, J. (2003). Experimental investigation of splash and crown formation during single drop impact on wetted surfaces. *Experiments in fluids*, 35(6):648–652.

Rioboo, R., Marengo, M., and Tropea, C. (2002). Time evolution of liquid drop impact onto solid, dry surfaces. *Experiments in fluids*, 33(1):112–124.

Rioboo, R., Tropea, C., and Marengo, M. (2001). Outcomes from a drop impact on solid surfaces. *Atomization and sprays*, 11(2).

Roisman, I. and Tropea, C. (2002). Impact of a drop onto a wetted wall: description of crown formation and propagation. *Journal of Fluid Mechanics*, 472:373–397.

Roisman, I. V. (2009). Inertia dominated drop collisions. ii. an analytical solution of the navier–stokes equations for a spreading viscous film. *Physics of Fluids*, 21(5):052104.

Roisman, I. V. (2010). On the instability of a free viscous rim. *Journal of Fluid Mechanics*, 661:206–228.

Roisman, I. V., Berberović, E., and Tropea, C. (2009). Inertia dominated drop collisions. i. on the universal flow in the lamella. *Physics of fluids*, 21(5):052103.

Roisman, I. V., Gambaryan-Roisman, T., Kyriopoulos, O., Stephan, P., and Tropea, C. (2007). Breakup and atomization of a stretching crown. *Physical Review E*, 76(2):026302.

Roisman, I. V., Horvat, K., and Tropea, C. (2006). Spray impact: rim transverse instability initiating fingering and splash and description of a secondary spray. *Physics of Fluids*, 18(10):102104.

Roisman, I. V., Lembach, A., and Tropea, C. (2015). Drop splashing induced by target roughness and porosity: The size plays no role. *Advances in colloid and interface science*, 222:615–621.

Roisman, I. V., Prunet-Foch, B., Tropea, C., and Vignes-Adler, M. (2002a). Multiple drop impact onto a dry solid substrate. *Journal of colloid and interface science*, 256(2):396–410.

Roisman, I. V., Rioboo, R., and Tropea, C. (2002b). Normal impact of a liquid drop on a dry surface: model for spreading and receding. *Proceedings of the Royal Society of London. Series A: Mathematical, Physical and Engineering Sciences*, 458(2022):1411–1430.

Roisman, I. V., van Hinsberg, N. P., and Tropea, C. (2008). Propagation of a kinematic instability in a liquid layer: capillary and gravity effects. *Physical Review E*, 77(4):046305.

Rozhkov, A., Prunet-Foch, B., and Vignes-Adler, M. (2002). Impact of water drops on small targets. *Physics of Fluids*, 14(10):3485–3501.

Saffman, P. (1965). The lift on a small sphere in a slow shear flow. *Journal of fluid mechanics*, 22(2):385–400.

Sahu, R. P., Sinha-Ray, S., Yarin, A. L., and Pourdeyhimi, B. (2012). Drop impacts on electrospun nanofiber membranes. *Soft Matter*, 8(14):3957–3970.

Samenfink, W., Elsäßer, A., Dullenkopf, K., and Wittig, S. (1999). Droplet interaction with shear-driven liquid films: analysis of deposition and secondary droplet characteristics. *International journal of heat and fluid flow*, 20(5):462–469.

Scardovelli, R. and Zaleski, S. (1999). Direct numerical simulation of free-surface and interfacial flow. *Annual review of fluid mechanics*, 31(1):567–603.

Scheller, B. L. and Bousfield, D. W. (1995). Newtonian drop impact with a solid surface. *AIChE Journal*, 41(6):1357–1367.

Schilling, F., Kuthada, T., Gaylard, A., Wiedemann, J., and Wagner, A. (2020). Advances in experimental vehicle soiling tests. Technical report, SAE Technical Paper.

Schremb, M., Roisman, I. V., and Tropea, C. (2018). Normal impact of supercooled water drops onto a smooth ice surface: experiments and modelling. *Journal of Fluid Mechanics*, 835:1087.

Seiler, P. M., Gloerfeld, M., Roisman, I. V., and Tropea, C. (2019). Aerodynamically driven motion of a wall-bounded drop on a smooth solid substrate. *Physical Review Fluids*, 4(2):024001.

Shen, S., Chen, G., Crone, R. M., and Anaya-Dufresne, M. (2007). A kinetic-theory based first order slip boundary condition for gas flow. *Physics of Fluids*, 19(8):086101.

Shetabivash, H., Ommi, F., and Heidarinejad, G. (2014). Numerical analysis of droplet impact onto liquid film. *Physics of Fluids*, 26(1):012102.

Šikalo, Š. and Ganić, E. (2006). Phenomena of droplet–surface interactions. *Experimental thermal and fluid science*, 31(2):97–110.

Smith, F., Li, L., and Wu, G. (2003). Air cushioning with a lubrication/inviscid balance. *Journal of Fluid Mechanics*, 482:291–318.

Spiel, D. E. (1998). On the births of film drops from bubbles bursting on seawater surfaces. *Journal of Geophysical Research: Oceans*, 103(C11):24907–24918.

Staat, H. J. J., Tran, T., Geerdink, B., Riboux, G., Sun, C., Gordillo, J. M., and Lohse, D. (2015). Phase diagram for droplet impact on superheated surfaces. *Journal of fluid mechanics*, 779.

Stevens, C. S. (2014). Scaling of the splash threshold for low-viscosity fluids. *EPL (Europhysics Letters)*, 106(2):24001.

Stevens, C. S., Latka, A., and Nagel, S. R. (2014). Comparison of splashing in high-and low-viscosity liquids. *Physical Review E*, 89(6):063006.

Stow, C. D. and Stainer, R. D. (1977). The physical products of a splashing water drop. *Journal of the Meteorological Society of Japan*, 55(5):518–531.

Taylor, G. I. (1959). The dynamics of thin sheets of fluid ii. waves on fluid sheets. *Proceedings of the Royal Society of London. Series A. Mathematical and Physical Sciences*, 253(1274):296–312.

Thoraval, M.-J., Takehara, K., Etoh, T., and Thoroddsen, S. T. (2013). Drop impact entrapment of bubble rings. *Journal of Fluid Mechanics*, 724:234–258.

Thoraval, M.-J., Takehara, K., Etoh, T. G., Popinet, S., Ray, P., Josserand, C., Zaleski, S., and Thoroddsen, S. T. (2012). von kármán vortex street within an impacting drop. *Physical review letters*, 108(26):264506.

Thoroddsen, S. (2002). The ejecta sheet generated by the impact of a drop. *Journal of Fluid Mechanics*, 451:373–381.

Thoroddsen, S., Etoh, T., and Takehara, K. (2003). Air entrapment under an impacting drop. *Journal of Fluid Mechanics*, 478:125–134.

Thoroddsen, S., Etoh, T., Takehara, K., Ootsuka, N., and Hatsuki, Y. (2005). The air bubble entrapped under a drop impacting on a solid surface. *Journal of Fluid Mechanics*, 545:203–212.

Thoroddsen, S., Etoh, T. G., and Takehara, K. (2006). Crown breakup by marangoni instability. *Journal of Fluid Mechanics*, 557:63–72.

Thoroddsen, S. T., Etoh, T. G., and Takehara, K. (2008). High-speed imaging of drops and bubbles. *Annu. Rev. Fluid Mech.*, 40:257–285.

Thoroddsen, S. T. and Sakakibara, J. (1998). Evolution of the fingering pattern of an impacting drop. *Physics of fluids*, 10(6):1359–1374.

Thoroddsen, S. T., Takehara, K., and Etoh, T. G. (2012a). Micro-splashing by drop impacts. *Journal of Fluid Mechanics*, 706:560–570.

Thoroddsen, S. T., Thoraval, M.-J., Takehara, K., and Etoh, T. (2011). Droplet splashing by a slingshot mechanism. *Physical review letters*, 106(3):034501.

Thoroddsen, S. T., Thoraval, M.-J., Takehara, K., and Etoh, T. (2012b). Micro-bubble morphologies following drop impacts onto a pool surface. *Journal of fluid mechanics*, 708:469–479.

Tran, T., de Maleprade, H., Sun, C., and Lohse, D. (2013). Air entrainment during impact of droplets on liquid surfaces. *Journal of Fluid Mechanics*, 726.

Trontin, P. and Villedieu, P. (2017). Revisited model for supercooled large droplet impact onto a solid surface. *Journal of Aircraft*, 54(3):1189–1204.

Tropea, C., Feldmann, J., Rettenmaier, D., Seiler, P. M., Ade, M., and Demel, D. (2019). External water management: A predictive challenge. In *19. Internationales Stuttgarter Symposium*, pages 398–411. Springer.

Tropea, C. and Marengo, M. (1999). The impact of drops on walls and films. *Multiphase Science and Technology*, 11(1).

Tropea, C. and Roisman, I. V. (2000). Modeling of spray impact on solid surfaces. *Atomization and sprays*, 10(3-5).

Tsai, P., van der Veen, R. C. A., van de Raa, M., and Lohse, D. (2010). How micropatterns and air pressure affect splashing on surfaces. *Langmuir*, 26(20):16090–16095.

Van Leer, B. (1974). Towards the ultimate conservative difference scheme. ii. monotonicity and conservation combined in a second-order scheme. *Journal of computational physics*, 14(4):361–370.

Vander Wal, R. L., Berger, G. M., and Mozes, S. D. (2006a). Droplets splashing upon films of the same fluid of various depths. *Experiments in fluids*, 40(1):33–52.

Vander Wal, R. L., Berger, G. M., and Mozes, S. D. (2006b). The splash/non-splash boundary upon a dry surface and thin fluid film. *Experiments in fluids*, 40(1):53–59.

Villermaux, E. (2007). Fragmentation. *Annu. Rev. Fluid Mech.*, 39:419–446.

Villermaux, E. (2020). Fragmentation versus cohesion. *J. Fluid Mech*, 898:P1.

Villermaux, E. and Bossa, B. (2011). Drop fragmentation on impact. *Journal of Fluid Mechanics*, 668:412–435.

Villermaux, E. and Clanet, C. (2002). Life of a flapping liquid sheet. *Journal of fluid mechanics*, 462:341–363.

Visser, C. W., Tagawa, Y., Sun, C., and Lohse, D. (2012). Microdroplet impact at very high velocity. *Soft matter*, 8(41):10732–10737.

Wagner, H. (1932). Über stoß-und gleitvorgänge an der oberfläche von flüssigkeiten. *ZAMM-Journal of Applied Mathematics and Mechanics/Zeitschrift für Angewandte Mathematik und Mechanik*, 12(4):193–215.

Walsh, P. P. and Fletcher, P. (2004). *Gas turbine performance*. John Wiley & Sons.

Wang, A.-B. and Chen, C.-C. (2000). Splashing impact of a single drop onto very thin liquid films. *Physics of fluids*, 12(9):2155–2158.

Wang, Y. and Bourouiba, L. (2018). Unsteady sheet fragmentation: droplet sizes and speeds. *Journal of Fluid Mechanics*, 848:946–967.

Weiss, D. A. (1993). *Periodischer Aufprall monodisperser Tropfen gleicher Geschwindigkeit auf feste Oberflächen*. PhD thesis, Universität Göttingen, Göttingen.

Weiss, D. A. and Yarin, A. L. (1999). Single drop impact onto liquid films: neck distortion, jetting, tiny bubble entrainment, and crown formation. *Journal of Fluid Mechanics*, 385:229–254.

Wilke, C. (1950). A viscosity equation for gas mixtures. *The journal of chemical physics*, 18(4):517–519.

Worthington, A. M. (1908). *A study of splashes*. Longmans, Green, and Company.

Wright, W. and Potapczuk, M. (2004). Semi-empirical modelling of sld physics. In *42nd AIAA aerospace sciences meeting and exhibit*, page 412.

Xavier, T., Zuzio, D., Averseng, M., and Estivalezes, J.-L. (2019). Toward direct numerical simulation of high speed droplet impact. *Meccanica*, pages 1–15.

Xu, L., Barcos, L., and Nagel, S. R. (2007). Splashing of liquids: Interplay of surface roughness with surrounding gas. *Physical Review E*, 76(6):066311.

Xu, L., Zhang, W. W., and Nagel, S. R. (2005). Drop splashing on a dry smooth surface. *Physical review letters*, 94(18):184505.

Yarin, A. and Weiss, D. (1995). Impact of drops on solid surfaces: self-similar capillary waves, and splashing as a new type of kinematic discontinuity. *Journal of fluid mechanics*, 283:141–173.

Yarin, A. L. (1993). *Free liquid jets and films: hydrodynamics and rheology*. Longman Publishing Group.

Yarin, A. L. (2006). Drop impact dynamics: splashing, spreading, receding, bouncing.... *Annu. Rev. Fluid Mech.*, 38:159–192.

Yarin, A. L., Roisman, I. V., and Tropea, C. (2017). *Collision phenomena in liquids and solids*. Cambridge University Press, Cambridge.

Zhang, D., Jiang, C., Liang, D., and Cheng, L. (2015). A review on tvd schemes and a refined flux-limiter for steady-state calculations. *Journal of Computational Physics*, 302:114–154.

Zhang, L., Toole, J., Fezzaa, K., and Deegan, R. (2012a). Evolution of the ejecta sheet from the impact of a drop with a deep pool. *Journal of fluid mechanics*, 690:5–15.

Zhang, L., Toole, J., Fezzaa, K., and Deegan, R. (2012b). Splashing from drop impact into a deep pool: multiplicity of jets and the failure of conventional scaling. *Journal of fluid mechanics*, 703:402–413.

Zhou, C., Yue, P., Feng, J. J., Ollivier-Gooch, C. F., and Hu, H. H. (2010). 3d phase-field simulations of interfacial dynamics in newtonian and viscoelastic fluids. *Journal of Computational Physics*, 229(2):498–511.

Niedersächsisches Forschungszentrum für Luftfahrt
Hermann-Blenk-Straße 42
38108 Braunschweig
nfl@tu-braunschweig.de
www.tu-braunschweig.de/nfl